Development, Kinetic Analysis and Applications of 2-D Nanostructured Layered Metal Hydroxides

Stephen Majoni
Marquette University

DEVELOPMENT, KINETIC ANALYSIS AND APPLICATIONS OF 2-D
NANOSTRUCTURED LAYERED METAL HYDROXIDES

by

Stephen Majoni
BSc (Hons) Biochemistry, University of Zimbabwe, 2001

A Dissertation submitted to the Faculty of the Graduate School,
Marquette University,
in Partial Fulfillment of the Requirements for
the Degree of Doctor of Philosophy

Milwaukee, Wisconsin

December, 2011

ABSTRACT
DEVELOPMENT, KINETIC ANALYSIS AND APPLICATIONS OF 2-D
NANOSTRUCTURED LAYERED METAL HYDROXIDES

Stephen Majoni, BSc.

Marquette University, 2011

Nanodimensional layered metal hydroxides which include layered hydroxy salts (LHSs) and hydroxy double salts (HDSs) have the ability to accommodate species between the layers. The structural composition of these materials can be tuned so as to create materials with targeted physico-chemical properties for applications where it is advantageous to intercalate or release molecules. Some of the applications include ion-exchange, fire retardation, catalysis, and controlled release delivery. Anion exchange reactions are among methods used to optimize these materials for targeted applications, making the characterization of exchange kinetics of practical interest. In addition, understanding fundamental factors that control retention and release of functional anions is important in designing hosts for storage and triggered release.

Isomers of hydroxycinnamate were used as model compounds to systematically explore the effects of anion structure on controlled release delivery in layered metal hydroxides. Following intercalation and subsequent release of the isomers, it has been demonstrated that the nature and position of substituent groups on interlayer anions have considerable effects on the rate and extent of release. The extent of release was correlated to the magnitude of dipole moments of the anions while the reaction rate showed strong dependence on the level of hydrogen bond network within the layers. Anion exchange kinetic analyses of this class of compounds have traditionally been carried out using model fitting methods. Isoconversional (model-free) approach can be utilized to identify when fitting to a single model is not appropriate, particularly for characterizing the temperature dependence of the reaction kinetics. We established a systematic analysis for identifying cases when model based approaches are not appropriate in modeling anion exchange kinetics in these compounds. Results obtained demonstrate the utility of the isoconversional approach for identifying when fitting kinetic data to a single model is not appropriate.

In another study, nanocomposites prepared by compounding poly (methyl methacrylate) with boron containing LHSs showed enhanced thermal stability and reduced flammability (up to 48 %) as evaluated by thermogravimetry analysis and cone calorimetry. Effective activation energies for the first step of the degradation process (evaluated using Flynn-Wall-Ozawa, Friedman, and Kissinger methods) were shown to be higher in the nanocomposites.

ACKNOWLEDGEMENTS

Stephen Majoni, BSc

It is a pleasure to thank those who made this dissertation possible; first and foremost I would like to express my deep and heartfelt gratitude to my supervisor Dr. Jeanne M. Hossenlopp for her continuous support and feedback during each step of the research work. Her patience, motivation, enthusiasm and guidance are greatly appreciated. I will always treasure the knowledge and skills I have gained from her. I would also like to thank her for extraordinary amount of experimental and intellectual freedom during my years here.

I am also grateful to Dr. Scott Reid and Dr. Dmitri Babikov for the time they took to serve in my dissertation committee, and I appreciate all the valuable suggestions and advice they gave me. I would also like to thank Dr. Chieu Tran whom we collaborated with. I am also delighted to express my gratitude to Dr Qadir Timerghazin for being my faculty mentor for preparing future faculty program; I appreciate all the help he has given me on the teaching aspects of my Ph.D. program.

I am also thankful to the National Science Foundation, and the US Department of Commerce, National Institute of Standards and Technology, for providing the financial support for this work. I would also like to thank past and present group members, with special mention going to Dr. Allen Chaparadza for all the help he has offered. I am

grateful to all friends and colleagues at Marquette University who offered assistance and encouragement.

My deepest gratitude goes to my wife, Susan, for her understanding and love during the past few years. Her support and encouragement was pivotal in making this dissertation possible. My parents and rest of my family receive my heartfelt gratitude and love for their dedication and the many years of support during my undergraduate studies that provided the foundation for this work, may God bless them all in abundance.

TABLE OF CONTENTS

LIST OF TABLES

LIST OF FIGURES

Chapter 1 :   Nanodimensional Layered Metal Hydroxides: Applications and Kinetic Analysis

1.1   Introduction.

Nanodimensional layered metal hydroxides have been shown to undergo ion exchange reactions with a variety of inorganic and organic anions.[1-5] These materials can generally be grouped, according to their structure, into layered double hydroxides (LDHs), hydroxy double salts (HDSs), and layered hydroxy salts (LHSs).[6] Layered metal hydroxides are composed of brucite-like metal hydroxide layers alternating with interlayer anions; one metal hydroxide layer and one interlayer space together make up an elementary layer.[7] In brucite, $\{Mg(OH)_2\}$, the magnesium ions are octahedrally coordinated by hydroxyl groups forming octahedral units.[2;3;8] The octahedral units share edges to form an infinite network of neutral layers (sheets) as shown in Figure 1.1, the sheets are stacked one on top of another and are held together by Van der Waals interactions and hydrogen bonds to form the brucite crystal.

In layered metal hydroxides, the metal hydroxide layers are positively charged and can be composed of one, two and sometimes three metal ions. The layers form the backbone of the structure with negatively charged ions, and often water molecules, in the interlayer space (sites). The formed structures are stabilized by electrostatic attraction between the layers and the anions as well as a network of hydrogen bonds between the interlayer anions, water molecules and the layers.[9;10] Although most of the charge balancing anions are situated in the interlayer space (gallery), NMR studies by Hou *et al.* have indicated that there are small amounts of weakly bound anions located on the

surface of the metal hydroxide sheets.[11;12] The ability to vary the metal ion constituents of the layers and the intercalation of different charge balancing interlayer anions results in a large class of materials which can potentially be synthesized.
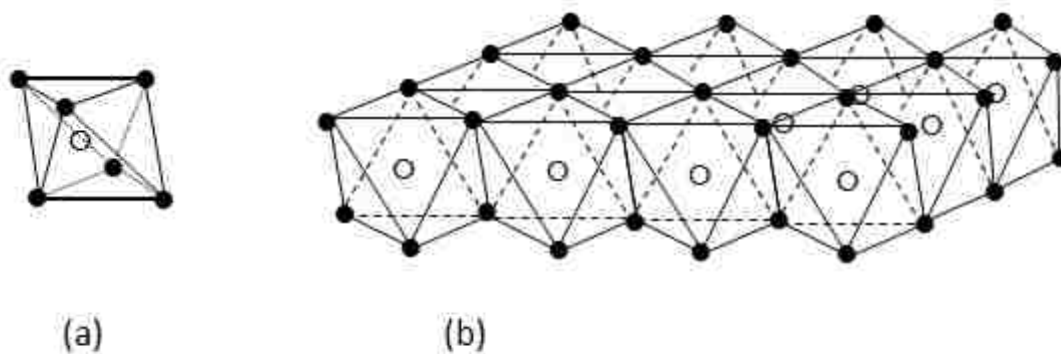
Figure 1.1: Schematic representation of a typical brucite octahedron (a), and the brucite sheets (b) with ○ representing Mg^{2+} ion, and ● representing hydroxyl ion.

1.2   Structure and Reactivity

Naturally occurring layered metal hydroxides are widespread and the crystal structures of many of the minerals have been determined. These include Mg,Fe-carbonates (pyrourite and sjögrenite); Mg,Al- carbonates (hydrotalcite and manasseïte); Ca,Al- carbonates (hydrocalumite); Cu-Cl (clinoatacamite and botallackite); Cu-NO$_3$ (gerhardtite), Zn,Cu-Cl (e.g. kapellasite) among others.[7;13-17] In the most common naturally occurring LDH, hydrotalcite, the metal hydroxide layers are composed of the cations Mg^{2+} and Al^{3+} with carbonate anions as the interlayer anions. Depending on symmetry, the formula of hydrotalcite can be $[Mg_6Al_2(OH)_{16}](CO_3).4H_2O$ for

hexagonal symmetry or $[Mg_6Al_2(OH)_{16}](CO_3) \cdot H_2O$ for rhombohedral symmetry.[16;17] The layered structure in hydrotalcite is obtained from brucite by the isomorphous substitution of some of the Mg^{2+} ions with Al^{3+} ions. The isomorphous substitution of divalent cations with trivalent cations generates a positive charge within the layers and charge compensating anions (normally represented as A^{n-}) are located in the interlayer regions between the brucite like-sheets.[8] The range of divalent and trivalent cations (M^{2+} and M^{3+}) which can constitute the LDH metal hydroxide layers is large, the only requirement being that their ionic radii should be close to each other.[2] As in brucite, the metal ions occupy octahedral positions within the metal hydroxide, $([M_{1-x}^{2+}M_x^{3+}(OH)_2]^{x+})$, layers. [18] The value of x (the layer charge) is equal to $\left[\frac{M^{3+}}{M^{2+}+M^{3+}}\right]$, and it is usually in the range 0.17-0.38.[16] This indicates that the ratio (M^{2+} to M^{3+}) determine the charge density on the hydroxide layers which enables tuning of the charge density by varying the ratio of the metals. The formula for LDHs can general be expressed as $[(M_{1-x}^{2+}M_x^{3+}(OH)_2]^{x+}(A^{n-})_{x/n} \cdot mH_2O$[16] with water molecules also occupying the interlayer space.

The brucite-like layers can be stacked two layers per unit cell with hexagonal symmetry (2H), three layers per cell with rhombohedral symmetry (3R), or other arrangements of lower symmetry.[16;19] The water molecules in these structures have been shown to be closely associated with the layer hydroxyl groups, participating in hydrogen bonding and thereby wetting the layers. In addition to wetting the layers, water molecules also hydrate the interlayer anion by forming hydrogen bonds with the interlayer anions.[20] Molecular dynamic calculations carried out by Padma *et al.* on citrate containing MgAl-

LDH indicated that, due to the citrate anions being H-bond acceptors and the layers being H-bond donors, the water molecules have a preference to wet the LDH layers by being H-bond acceptors than hydrate the interlayer citrate anions by being donors.[21] During hydration of anhydrous LDHs, the H-bond network between the layer hydroxyl groups and interlayer anions weaken in favor of forming H-bonds with water molecules. This results in wetting of the layers and hydration of the anions leading to swelling of the structure which may lead to exfoliation of the layers.[9;10;20;21] The water content, together with the interlayer anions and the layer charge, influence the interlayer distance enabling tuning of the materials.[21] Thus the nature of anions and their subsequent interactions with the layers affect the stability and reactivity of these materials.[8] The interlayer anions in LDHs can be exchanged by suspending the materials in solutions containing other anions.[3;16] The structure of LDH can be represented as shown in figure 1.2.
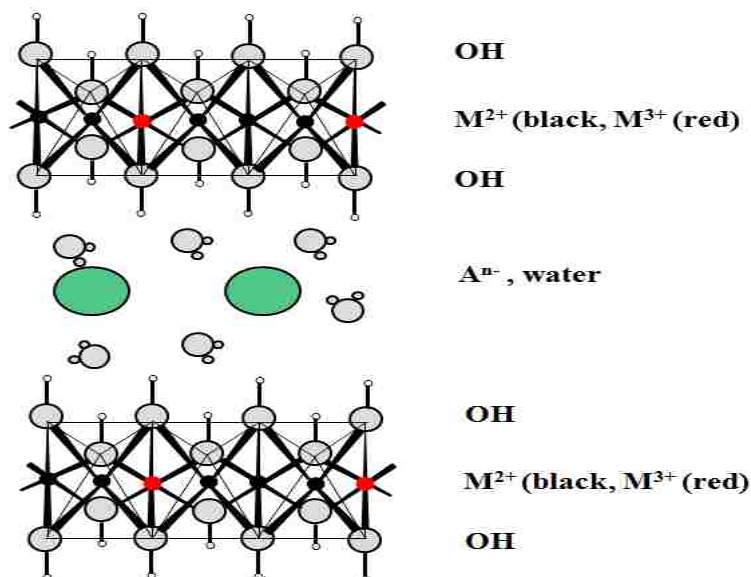
Figure 1.2: Structure of LDH[22] which is stabilized by electrostatic attraction between the layers and the anions and hydrogen bonds between water molecules, the layer hydroxyl groups and interlayer anions.

The structure of hydroxy double salts can generally be represented as $[(M^{2+}_{1-x}Me^{2+}_{1+x})(OH)_{3(1-y)/n}]A^{n-}_{(1+3y)/n}\cdot mH_2O$ where M^{2+} and Me^{2+} represent different divalent metal ions. In layered hydroxy salts, which are closely related to HDSs, $M^{2+}= Me^{2+}$ (thus they contain a single type of divalent metal ion). The differences in the ionic radii of the divalent Me^{2+} and M^{2+} metal ions in the brucite-like metal hydroxide layers of HDSs should be within 0.05Å. The structure formed and the relative composition of the ions in the metal hydroxide layers depends on the preparation method and the nature of the metal ions.[6;23] HDSs and LHSs can be classified broadly into two structural types based on the structure of either zinc hydroxy nitrate (ZHN) with the formula $Zn_5(OH)_8(NO_3)_2\cdot 2H_2O$ or copper hydroxy nitrate (CHN) with the formula $Cu_2(OH)_3NO_3$.[24]

The ZHN structure is regarded as a variation of the hypothetical $Zn(OH)_2$ structure in the C6 or CdI_2-type group.[25;26] In this mineral, a quarter of the zinc ions in the octahedral interstices of the sheets are vacant which would result in negatively charged sheets which can be represented as $[Zn_3^{oct}(OH)_8]^{2-}$. However, tetrahedral sites above and below the vacant octahedron are occupied by zinc ions, resulting in sheets which are positively charged with the formula $[Zn_3^{oct}(OH)_8\ Zn_2^{tetra}(H_2O)_2]^{2+}$.[27] The tetrahedral coordination of Zn^{tetra} is satisfied by three hydroxyl groups and a water molecule. The nitrate ions are located in the interlayer space and are held within the layers by electrostatic attraction, almost preserving the D_{3h} symmetry in free ions. The near-complete preservation of the D_{3h} symmetry is supported by the insignificant difference of the N-O bond length and also from infrared spectrum, shown in Figure 1.3, in which the doubly degenerate N-O stretching frequency υ_3 near 1380 cm^{-1} is strong and is not split.[27]
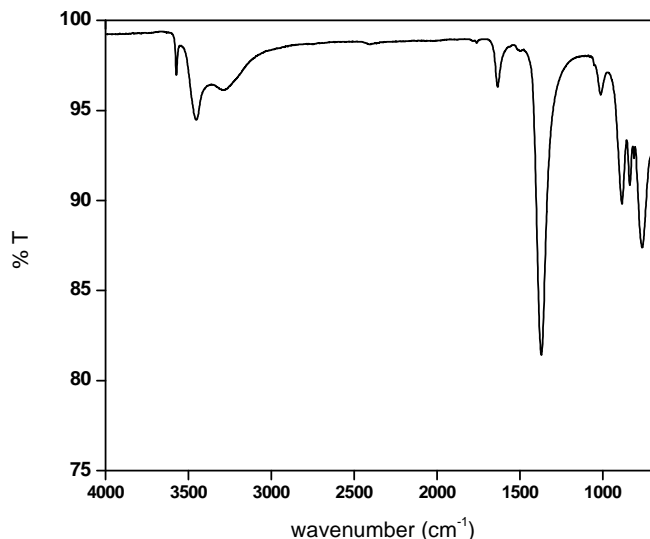
Figure 1.3. Infrared spectrum of ZHN

Techniques sensitive to the local environments around specific atoms within the

structures such as X-ray absorption near edge structure (XANES) spectroscopy and

extended X-ray absorption fine structure (EXAFS), have been used to accurately

determine the local structure of metal ions such as coordination number and atomic

distances.[28-30] EXAFS studies on zinc nickel hydroxy acetate (which has a ZHN

structure) by Choy *et al.* and Rojas *et al.* indicates that in this HDS structure, nickel ions

occupy octahedral sites of the metal hydroxide layers while zinc ions occupy tetrahedral

sites above and below vacant octahedral sites as indicated in Figure 1.4.[28;31] As shown in

Figure 1.4, the interlayer anions are found around the zinc ions where positive charge is

localized. As in LDHs, structural stability of materials based on the ZHN structure is

based mainly on layer-anions electrostatic interaction as well as the hydrogen bonding

network among interlayer anions, water molecules, and layer hydroxyl groups. Changes

in the hydration conditions of the materials are bound to result in changes in the

orientation of the interlayer anions so as to maximize the hydrogen bonding interactions and adopt the most stable arrangement. Choy *et al.* observed that in Ni,Zn-acetate HDS prepared under hydrothermal conditions, the acetate ions changed from chelating binding to unidentate binding during deintercalation of water molecules.[32]
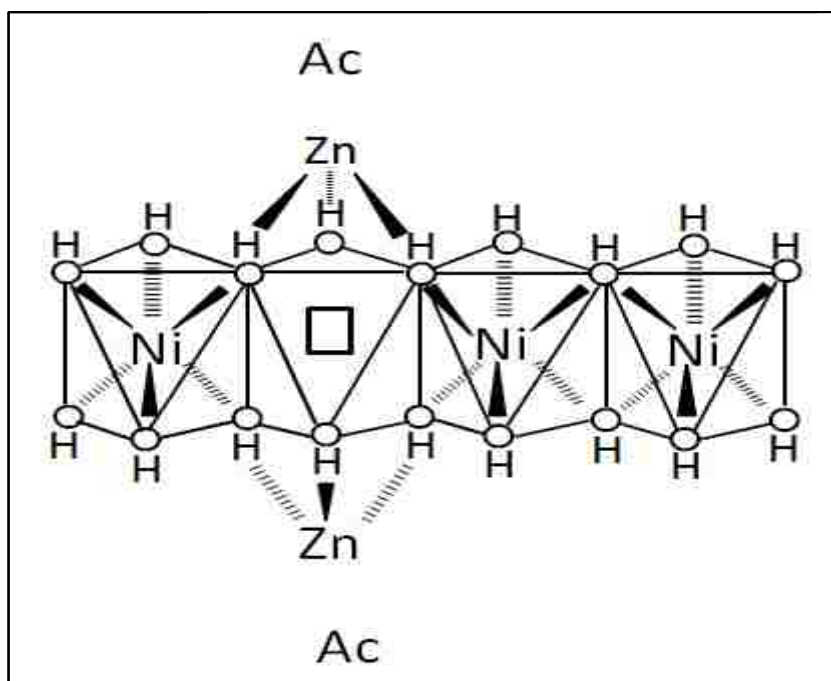
Figure 1.4: The structure of zinc nickel hydroxy acetate with the nickel vacancies being represented by □ and oxygen atom s by ○ [28]

In the CHN structure, the brucite-like layers are not positively charged as in the case of ZHN structure, but the interlayer anions (nitrate) are introduced by the replacement of 25% of the OH⁻ ions of the metal hydroxide layers by NO_3^- ions. [33] The interlayer ions are therefore coordinated directly to the metal matrix. EXAFS studies

have indicated that copper ions in CHN occupy two crystallographically distinct sites. Cu(1) is coordinated to four hydroxyl ions and two ionic oxygens (from nitrate ions) in a 4+2 coordination, and Cu(2) is coordinated to five hydroxyl groups and one nitrate oxygen (4+1+1 coordination) with a Jahn-Teller distortion.[29;33] The individual layers are connected by hydrogen bonds between the interlayer anions coordinated to one layer and the OH groups of the other layer.

1.2.1   Applications

The capacity to host different anions within the gallery and the ability to vary the constituent metal ions in the layers has enabled fine tuning of these materials for a variety of applications. Various groups, including this lab and the group of Prof. Wilkie at Marquette University, have separately done extensive studies on the applications of layered metal hydroxides as fire retardants (FR). The general property which makes layered metal hydroxide FRs useful in reducing the flammability of polymers is their $Mg(OH)_2$ like properties. These materials have one or more endothermic reactions during the heating process which act to absorb heat from the combustion process. Magnesium hydroxide absorbs approximately 1.42 $MJkg^{-1}$ of heat by losing water in the reaction shown in equation 1.1.[34] The metallic oxide residues formed during the decomposition process also impedes the burning process by acting as a barrier to air and heat transfer.

$$Mg(OH)_2 \xrightarrow{\Delta} MgO + H_2O \qquad \textbf{Equation 1.1}$$

Improvements in thermal stability and selected flammability properties such as peak heat release rate (PHRR) and total heat release (THR) have been observed in a wide

range of polymers by using layered metal hydroxides.[35-41] PHRR is an important

parameter in assessing polymer flammability as it has been considered as the variable

which expresses the flame intensity and fire spread in fire situation.[42] The properties of

FR are usually evaluated using three main methods; oxygen index, the UL-94 test, and

cone calorimetry.[43] Since most of the important parameters for evaluation of FR (such as

PHRR and THR) can be obtained from the cone calorimetry, the instrument has been one

of the most effective bench-scale method for studying FR.[44] Since the pioneering work of

Gilman *et al*. in evaluation of FR properties of layered silicate nanocomposites,[45] a lot of

effort has been dedicated in investigating the FR properties of layered materials including

the layered silicates [46-53] and LDH.[35-37;54-59] Although HDSs and LHSs have not been

extensively studied as compared to other layered materials, the LDHs and layered

silicates, they have similarly been shown to have potential as fire retardants.[38-41]

The potential for sustained release of intercalated anions and biocompatibility of

layered metal hydroxides have resulted in a growing area of research dedicated in

optimizing the materials for the uptake, storage and controlled release delivery of

bioactive materials such as drugs and pesticides.[60-67] In the most comprehensive study to

date on the use of the materials in controlled release of bioactive compounds and

industrial chemicals, Khan *et al.* showed that a variety of compounds ranging from drugs

to color fixants can be intercalated into, and subsequently released from, layered metal

hydroxides.[67] In this study it was shown that the rate of release depends on the metal ion

composition of the metal hydroxide layers and also on the size and nature of the

intercalated anions. In another study, Panda *at al* reported sustained release of pravastain

and fluvastatin drugs incorporated in Mg,Al-LDH with 90% of pravastain being released

in 10 hrs and 85 % of fluvastatin being released in 32 hrs. [63] Also since the LDHs have

been shown to intercalate admixtures used in the cement industry,[68] the controlled release

of these compounds can be used to control the kinetics of cement hydration.

Selectivity of the materials to isomeric compounds has also been observed and

can be utilized in separation of closely related materials[64;69-74] Studies by Takaya *et al.*[74]

have shown that zinc hydroxy nitrate and copper hydroxy nitrate exhibited selectivity in

the intercalation of the isomers 1-naphthoic acid and 2-naphthoic acid; in the same study,

2-naphthoic acid was preferred to 2,7-naphthoic dicarboxylic acid. In a more

comprehensive study, Ragavan *et al.*[75] studied the intercalation of chlorophenoxyacetates

{(4-; 2,4 di-; and 2,4,5 tri-) chlorophenoxyacetates}, into lithium aluminum chloride and

observed that there is selectivity depending on the extent of chlorination on the

molecules. It was observed that the rate and mechanisms of intercalation were different

among the three isomers. The selectivity of L-histidine over the D- stereoisomer into

Mg,Al-LDH observed by Ikeda *et al.*[1] indicates that the materials can also be applied in

chiral separation.

Research has also been carried out on the bacterial and viral sorption ability of

layered metal hydroxides. For example,   Jin *et al.* and You *et al.* have shown that Mg,Al

and Zn,Al-LDHs are capable of removing the viruses MS2,[76;77] ϕ X174[76] and the

bacterium E. *coli* [76] from synthetic ground water with efficiencies greater than 99 %.

There have also been studies on the use of layered metal hydroxides as point-of-use water

treatment devices due to their ability to adsorb and sequester water pollutants which

include herbicides[78] and harmful inorganic oxyanions such as arsenate, vanadate and

chromate.[79-82] In addition to the above applications, layered metal hydroxides have also

been applied in catalysis where they have been used in reactions such as

transesterification, hydrodechlorination of compounds such as trichloroethane, Michael

addition, Knoevenagel condensation, among other reactions.[83-86] Other uses include

corrosion inhibition, ion-exchange and as magnetic materials.[87-91] Wong and Buchheit [92]

have also utilized the memory effect of LDHs to sense water uptake in organic coatings.

1.2.2   Preparation Methods

Various methods have been used to synthesize nanodimensional layered metal

hydroxides, the simplest and the most commonly used method being coprecipitation. In

the coprecipitation method, LDHs are prepared by the drop wise combination of metal

salts of the dications and trications with the interlayer anion of choice while the pH is

maintained within a small range (usually around 10).[17;19;93] HDSs and LHSs on the other

hand are prepared from a reaction of metal oxides and metal salts of the dications and the

anion of interest with the synthetic conditions varying with the metal ions involved.[6;24]

LHS can also be prepared via a titration method in which solutions of the metal salts are

slowly reacted with precipitating agents such as NaOH or NH_4OH.[5;24;94] Although

coprecipitation is the simplest method, it may not be applicable in situations where the

anions of choice are not stable in alkaline solutions or where the anion is precipitated out

by one of the cations. In these cases, ion exchange method is used to obtain materials

with the interlayer anion of choice. In this method, the guests (anions of choice) are

exchanged with the anions already present in the interlayer regions of the layered

materials.[2] This is the main method for the preparation of organically modified materials.[2;3;6] Some of the other methods which have also been used successfully include the following; (i) Hydrolysis in urea, polyols and hexamethylenetetramine, which results in the production of highly crystalline materials with homogenous particle size; [95-99] (ii) hydrothermal methods, used when the interlayer anion of interest has a low affinity for the metal hydroxide layers, i.e. when coprecipitation and ion exchange are not applicable. [100-102] Hydrothermal methods have also been used as a post-synthesis procedure in the coprecipitation and titration methods. Recently, Zhang *et al.* have used the hydrothermal procedure to post-synthetically obtain Cd-dodecyl sulfate LHS with microtube or microrods morphology.[103] (iii) Direct reaction of lithium salts with aluminum hydroxide, which has been used to prepare lithium aluminum LDHs, the only stable LDH which is composed of a +1 cation.[104] (iv) Rehydration/ reconstruction method that makes use of the structural "memory effect" of the LDHs. In this method, water and the original interlayer ions are removed by calcinations of the LDH at moderate temperatures $450^{o}C$ – $600^{o}C$ resulting in mixed metal oxides. Due to the memory effect of the LDH, the layered structure is regenerated by dispersing the mixed oxides in water (CO_3^{2-} will be the interlayer anion) or solutions of the anion of interest in de-carbonated water.[105-107] This regeneration method has found applications in areas such as sensing [92] and water remediation.[82]

1.3   Condensed Phase Kinetic Analysis

One of the major reasons for quantifying rates of chemical reactions is that, by parameterizing the reaction rates as a function of state variables such as temperature, pressure, and concentration, prediction of the rates of reaction for any set of conditions becomes possible. Although no reaction mechanism can be proved on the basis of kinetic data alone, kinetic analysis also enables one to draw reasonable mechanistic conclusions.[108] The rate determining step of solid state kinetics can be the chemical transformation of reactants into products (or intermediates) or the transport of materials, by diffusion, to or from the reaction site. The kinetics of many solid state reactions can be represented by the general equation of the form

$$\frac{d\alpha}{dt} = k(T)f(\alpha) \qquad\qquad \textbf{Equation 1.2}$$

where α is the extent of reaction at time t, *k(T)* is the temperature dependent rate constant, and *f(α)* is the reaction model which describes the dependence of the reaction rate on the extent of reaction and contains information about the reaction mechanism. Some of the mostly used functional forms of the reaction models are shown in table 1.1. These models can be classified into 3 classes depending on the mechanism of the reaction; (1) reactions that are controlled by diffusion, (2) phase boundary controlled, and (3) reactions which obey the Avrami –Erofe'ev equations.[109;110] Equation 1.2 is usually used in the integral form shown in equation 1.3 in which g(α) is the integral reaction model.

$$g(\alpha) \equiv \int_0^\alpha [f(\propto)]^{-1}\, d\alpha = k(T)t \qquad\qquad \textbf{Equation 1.3}$$

The integral form of the reaction model (equation 1.3) allows the determination of the

rate constant (k) from the linear plots of $g(\alpha)$ as a function of time t.

Table 1.1 : Some of the Functional forms of the commonly used models for the kinetic analysis of solid-state reactions.

Model	Equation	Label	n
Power law	$\alpha^{1/m} = kt$	P	m
Avrami –Erofe'ev			
First order	$[\ln (1-\alpha)] = kt$	A1	1
Second order	$[\ln (1-\alpha)]^{1/2} = kt$	A2	2
Third order	$[\ln (1-\alpha)]^{1/3} = kt$	A3	3
Fourth order	$[\ln (1-\alpha)]^{1/4} = kt$	A4	4
Prout-Tomkins	$\ln [\alpha/(1-\alpha)] = kt$		
Diffusion models			
1-D diffusion	$\alpha^2 = kt$	D1	0.62
2-D diffusion	$(1-\alpha) \ln(1-\alpha) + \alpha = kt$	D2	
3-D diffusion (Jander expression)	$[1-(1-\alpha)^{1/3}]^2 = kt$	D 3	0.57
Gistling-Brounshtein	$[1- 2\alpha/3- (1-\alpha)^{2/3} = kt$		

For a specific chemical reaction, the reaction model is usually determined by

fitting the experimental data to different reaction models and determining the model that

accurately reproduces the data. This enables the reaction to be interpreted in terms of the

mechanism represented by the chosen (best-fitting) reaction model. The usual outcome of

this procedure is a single reaction model and a constant value of activation energy for the

overall process. Even when the experimental data do not closely follow any of the

available models, a commonplace practice is to choose the model that provides best

statistical fit of experimental data.[111] Sharp *et al.* [112] have shown that the comparison of

experimental data against a set of model plots can be facilitated by the use of reduced

time (t/t₀) approach in which α is plotted against t/t_o, where t_o is the half-life of the

reaction. This procedure of fitting experimental data to reaction models is thus referred to

as model fitting and, as indicated before, the mechanistic interpretations are made in

terms of the best-fitting model. Thus this procedure may not lead to an unambiguous

mechanistic interpretation of experimental data since the same process may be described

by various reaction models which result in different activation energies being obtained.[113]

To date, the Avrami –Erofe'ev equation appears to be the simplest model with the

broadest applications and has been regarded as a universal equation for the treatment of

solid state reactions and can therefore be used to compare kinetic data for most solid state

reactions.[114] The Avrami –Erofe'ev equation takes the form

$$a(t) = 1 - e^{[-(kt)^n]}$$ Equation 1.4

where *n* is the Avrami exponent and has integer values which varies from 1.0 to 4.0,

depending on the growth dimensionality and nucleation conditions. A value of *n* in the

region of 0.5 indicates a diffusion-controlled process.[114-116] Equation 1.4 can be

linearlized by taking the natural logarithms twice obtaining equation 1.5.

$$\ln[-ln(1-\alpha)] = nln(t) + nln(k)$$ Equation 1.5

The double-logarithmic plot of ln [-ln (1-α)] as a function of ln t gives a linear plot in which the value of n is obtained from the slope and the value of k is evaluated from the intercept. Although double-logarithmic plots have been used since the 1950s,[117] they were made popular by Sharp and Hancock in 1972.[114] The double-logarithmic analysis for reactions with different mechanisms gives linear plots with different slopes making it easy to distinguish reactions occurring via different mechanisms. The Avrami–Erofe'ev model has been applied successfully to a wide range of reactions which includes crystallization and phase transformations in glasses and alloys, metal hydrogenation reactions,[118] crystallization and growth of polymers,[119] and in anion exchange reactions of layered materials.[66;69;75;120-123]

Model based approaches suffer from the kinetic ambiguity which, as discussed before, stems from the observation that (in some instances) the experimental data give excellent fits to various reaction models and therefore significantly different mechanistic conclusions can be drawn and different activation energies are obtained.[113] The reliability of the Arrhenius parameters obtained from these model fitting procedures is therefore subject to proper choice of the reaction model.[124;125] Most importantly, model based approaches are most useful in the analysis of single step reactions. A strategy utilized in thermal analysis studies to identify when fitting to a single model is not appropriate is to utilize isoconversional methods as proposed by Vyazovkin and Wight.[126] The model-free methodology is built around the dependence of the activation energy on the extent of conversion which is used for both drawing mechanistic conclusions and predicting reaction rates. Model-free isoconversional methods are based on the isoconversional principle that states that the reaction rate at a constant extent of conversion is only a

function of the temperature which eliminates the need for a reaction model.[127] The

dependence of E_a on α indicates a variation of the relative contribution of single steps in

the overall reaction and can therefore be used to detect multi-step reactions. A detailed

explanation of the concept of variable activation energy, which is represented by

isoconversional methods, was given by Flynn and Wall in 1966.[128] Since isoconversional

methods enables the determination of the dependency of E_a on the extent of reaction, they

provide information about the changes in reaction mechanism and enables the

investigation of reaction mechanisms[129;130] and are therefore favored over model-fitting

methods.[124;131;132] For isothermal processes, isoconversional methods can be divided into

differential methods (equation 1.6) and integral method (equations 1.7).[129;131]

$$ln\frac{d\alpha}{dt} = ln\left[A\,f(\alpha)\right] - \frac{Ea}{RT} \qquad \qquad \textbf{Equation 1.6}$$

$$lnt = ln\frac{g(\alpha)}{A} + \frac{Ea}{RT} \qquad \qquad \textbf{Equation 1.7}$$

In equation 1.6 and 1.7, E_a, $f(\alpha)$, $g(\alpha)$ and α are as defined before, A is the pre-

exponential factor, t is the time, T the temperature, and R is the gas constant. The

isoconversional approach has been widely applied in the degradation kinetics of a variety

of materials which include polymers and inorganic molecules, recently the approach has

been extended to other reactions which include hydride formation in reactive plasmas.[133]

1.4   Motivation for the study

The flexibility in the composition of layered metal hydroxides and their ability to host and exchange different types of anions has resulted in the materials having extensive applications. Anion exchange is the most widely used method in modifying these materials and optimizing them for different applications. Although anion exchange is generally thought to occur via topotactic mechanism, there have been instances where it has been shown to occur via the dissolution-reprecipitation pathway. These two exchange mechanisms allow optimization of the materials for a variety of applications. For example, the intercalation of a wide range of anions into the gallery results in materials with improved magnetic, electronic, and catalytic properties. Detailed study of anion exchange in these materials will allow us to:

(1)   Provide insight in to the applications of isoconversional analysis in anion exchange kinetics of layered metal hydroxides

Substantial work has been carried out on anion exchange kinetics in layered metal hydroxides where both in situ data acquisition [66;69;75;120;122;123] and conventional quenching experiments have been used.[121;134;135] Kinetic analysis in these compounds has traditionally involved fitting experimental data to various reaction models and choosing the best fitting model to make kinetic and mechanistic conclusions. In some cases the same data set can satisfactorily fit more than one reaction model, or may result in a poor fit to all the available models. The choice of the model to represent the data is then based on the best statistical fit of experimental data. In these instances the reliability of the Arrhenius parameters obtained from model fitting procedures is then subject to the

proper choice of the reaction model.[124;125] This model fitting procedure is mainly applicable to single process reactions in which the mechanism does not change over the entire reaction. The procedure becomes inapplicable when describing multi-process reactions in which there are changes in reaction mechanism as the reaction proceeds, such as in cases where there are structural changes occurring during the exchange process. Although periods with different mechanisms can be distinguished in double-logarithmic plots when using the Avrami expression, obtaining an effective activation energy that can be utilized to describe the temperature dependence over the entire course of the reaction becomes difficult.[136]

In this study, we extend isothermal, isoconversional analysis to anion exchange kinetics in layered metal hydroxides. Two model reactions have been chosen to illustrate how the isoconversional approach can be exploited to identify when model-based approaches such as Avrami-Erofe'ev kinetics, are appropriate. Isoconversional analysis is applied to evaluate the rate of anion release into solution as well as changes in solid state structure in order to derive effective E_a that can be compared to global E_a values obtained from the Avrami-Erofe'ev model fitting method.

(2)   *Explore the role of anion structure on controlled release delivery in layered metal hydroxides*

Layered metal hydroxides have been shown to exhibit sustained release of intercalated anions over periods ranging from hours to days.[60;61;63;135;137] The work on HDS and LHS is limited yet it has been shown that HDSs show a slower release of anions and has greater capacity for intercalating anions, [116;135] which makes them more

applicable where slow release delivery of anions is required. The rate of release of intercalated anions which may be drugs, industrial chemicals, or pesticides depend on the intralayer metal composition of the host materials and the size of the intercalated materials.[67;135] Anions are stabilized in the interlayer space by electrostatic interactions with the layers, and also by a network of hydrogen bonds with layer hydroxyl and/ or interlayer water molecules.[21;138;139] Differences in stability of the anions may also affect the rates of release which enables tuning of the materials for controlled release delivery.

Characterization techniques such as powder X-ray diffraction (PXRD), Fourier transform infrared (FTIR) spectroscopy; thermogravimetric (TG) analysis, UV-Vis spectroscopy and elemental analysis will be used to get valuable information on the structural transformation and reactivity of the materials with emphasis on the kinetics of anion release. This study will provide insight into the chemistry that governs anion retention and release in layered metal hydroxides. This will provide vital information which can be used to screen these materials for applications in controlled release delivery of substances such as chemicals, drugs and pesticides. The ultimate goal is to provide information which will enable fine tuning of rates of release by altering the structure of intercalated anions.

(3)   Optimization of layered hydroxy salts for fire retardant properties

Poly (methyl methacrylate) is a synthetic polymer which is inexpensive, transparent and resistant to weathering. As such it has been widely used as a building material but suffers from the general flammability setback of synthetic polymers.[140] For a long time halogen based compounds have been used as additive flame retardants (FRs)

for different classes of polymeric materials with a good efficiency, but they have been shown to have negative environmental effects. [141-144] Layered metal hydroxides have been shown to improve thermal, physical and fire properties of a variety of polymers. The uses of HDSs and LHSs as FRs have been limited due to the fact that, for those systems studied, the flame retarding properties were inferior to those of LDHs. This study is based on the realization that with a careful choice of intra-layer metal ion(s) and interlayer anions then good reduction in flammability, comparable or better than current additives can be achieved. In this study a careful choice of the layer metal ion constituent(s) and the interlayer anion will enable us to design LHSs with superior FR performances that can be able to compete with commercially available materials. This work, together with previous work in this lab, will give us a better understanding of the role of metal ions in thermal/fire degradation processes of polymer-(nano)composites of single-metal-containing materials.

Chapter 2 : Experimental

2.1   Instrumentation

2.1.1   Thermogravimetric analysis

Thermogravimetry (TG) is a technique in which the mass of a sample is monitored as a function of temperature or time while the sample is subjected to a controlled temperature program.[145] Temperature programming can be heating at a linear rate (non-isothermal measurements), maintaining a constant temperature (isothermal measurements) or a combination of heating, cooling and isothermal stages. TG has applications in the determination of thermal stability of materials and characterization of polymers through loss of known entities, e.g. hydrochloric acid from poly(vinyl chloride).[146] Low temperature weight loss may arise from evaporation of moisture, while higher temperature weight loss may be due to material decomposition.[145;146]

Thermogravimetric analysis was performed on a Netzsch TG 209 F1, TGA instrument coupled to Fourier transform infrared (FTIR) spectrometer. Due to its ability to identify functional groups, FTIR allows for the identification of the products of thermal degradation thereby enabling a better understanding of the degradation process. Samples of the appropriate weight (specific details are given in experimental section sections of each chapter) were heated in air or inert (N_2) atmosphere in aluminum oxide crucibles. Measurements were performed in triplicates and the average is reported here, the temperature for a given mass loss is generally reproducible to $\pm$ 3°C.[53]

2.1.2 X-Ray Powder Diffraction

X-Ray diffraction (XRD) as a method of chemical analysis was developed by A.W. Hull in 1919.[147] The method is based on constructive interference when X-rays interact with a crystalline sample due to the phase relationship between beams of elastically scattered x-rays. Constructive interference occur when conditions satisfy Bragg's Law, $n\lambda = 2d\sin\theta$ (where n is the reflection order, λ is the wavelength of incident X-ray, d is the spacing between the planes in the lattice, and θ is the angle between the incident ray and the scattering planes).[148] The emitted X-rays are at characteristic angles based on the spaces between the atoms in the crystalline sample, thus every crystalline substance gives a unique pattern. Thus powder diffraction methods have been used for characterization and identification of polycrystalline phases.

The instrument used in this study was a Rigaku Miniflex II diffractometer operated in para-focusing Bragg-Bretano configuration using Ni filtered Cu Kα (λ =1.54 Å) radiation source at 30 kV and 15 mA. The diffractometer was calibrated using a silicon reference material (RSRP-43275G: manufactured by Rigaku Corporation). Estimation of crystallite sizes was performed using the Scherrer equation:[148]

$$\tau = \frac{\kappa\lambda}{\beta cos\theta} \qquad \text{Equation 2.1}$$

where τ is the crystallite size, κ is a constant (shape factor = 0.9 for powders), β is the full width at half maximum of the diffraction peak after correcting for instrumental broadening. λ is the X-ray wavelength. The silicon 111 peak at 28.4$^\mathrm{o}$ was used to correct for instrumental broadening. The *001* sample peaks were used to estimate the crystallite size in the c-axis dimension.

2.1.3 Cone Calorimetry

This test makes use of a cone calorimeter to measure the heat release rate (which is one of the most important parameters in a fire situation) among other parameters. The cone calorimeter utilizes the oxygen consumption principle which states that the heat release rate for a variety of materials, when normalized by the amount of oxygen consumed, is the same and has a numerical value of 13.1±5% kJ per gram of oxygen consumed.[149] The oxygen consumption principle assumes complete combustion of the materials. Although carbon monoxide is usually found in the products of combustion reaction of polymers, its concentrations are usually very low as compared to the concentration of carbon dioxide, thus the effect of incomplete combustion is minimal.[140]

In cone calorimetry, a square sample (100 mm x 100 mm with a thickness of 3 mm) is exposed to an external heat flux ranging from 10 to 110 kW/m^2. The external heat flux is supplied from a constant temperature electric heater which is in the shape of a cone (hence the name cone calorimeter). The general requirement is that the hood system should be able to collect all the products of combustion. The results from the cone calorimeter are generally considered to be reproducible to ± 10 %.[150] Here, the flammability measurements were conducted on an Atlas Cone 2 instrument, with the basic features being shown in Figure 2.1.
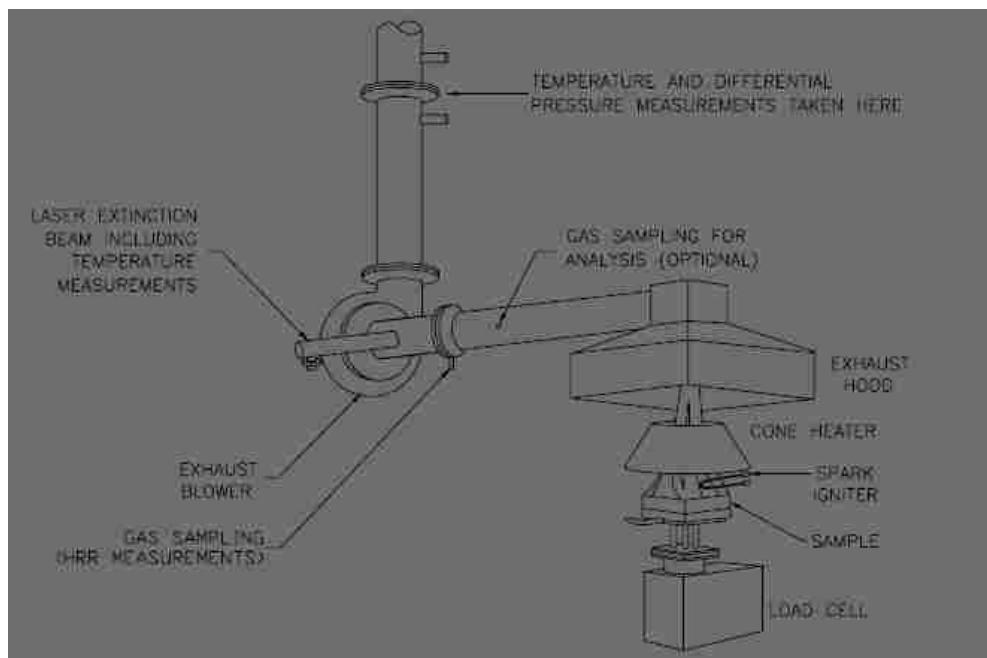
Figure 2.1: Schematic representation of the cone calorimeter (diagram obtained from http://www.doctorfire.com/cone_dwg.gif, accessed 06/01/11)

2.1.4   Attenuated Total Reflectance-Fourier Transform Infrared Spectroscopy

Fourier transform infrared (FTIR) spectroscopy is based on the absorption, by

covalent bonds in molecules, of electromagnetic radiation in the infrared region of the

electromagnetic spectrum. In attenuated total reflectance -Fourier transform infrared

(ATR-FTIR) spectroscopy, an ATR accessory with a highly refractive prism is used as a

sampling tool. In ATR sampling, the IR beam is totally reflected from the internal surface

of the prism at the prism-sample interface if the incident beam angle is larger than the

critical angle for internal reflection. The internal reflectance creates an evanescent wave

that extends beyond the surface of the crystal into the sample, which is in intimate contact

with the crystal, leading to some of the energy of the evanescent wave being absorbed by the sample. In regions of the infrared spectrum where the sample absorbs energy, the evanescent wave will be attenuated. Infrared spectral data reported in this study were either obtained on a Nicole Magna-IR 560 spectrometer or a Perkin Elmer Spectrum 100 FT-IR spectrometer using a single reflection ATR accessory.

2.1.5 UV-Visible Spectrometry

The concentration of released hydroxy(cinnamate) anions at specific time periods was monitored by UV-Vis analysis on a Shimadzu UV-2501 PC UV-Vis Recording Spectrophotometer or a Perkin Elmer Lambda 35 UV-Vis Spectrophotometer using quartz cuvettes with a path length of 1 cm; this was after the necessary dilutions were done (the general dilution factor was 1000).

2.1.6 Computational calculations

Chain lengths and dipole moments of anions used in this study were calculated utilizing the Gaussian 98 program[151] and carried out at the DFT (B3LYP) level of theory with 6-311++G(d,p) basis set. The chain lengths were calculated as the inter-atomic distance between the center of the carboxyl oxygen and the furthest hydrogen atom.

2.2 Synthesis of nanodimensional layered materials

Precursor layered hydroxy double salts (LHSs) and hydroxy double salts (HDSs) were prepared according to literature methods.[25;116;152] Basic copper nitrate (BCN) was prepared via a titration method; a 0.4 M copper nitrate solution was slowly titrated, under

continuous stirring, with 0.1 M NaOH solution until the ratio Cu^{2+}: OH^- of 1:1.5 was achieved. Zinc hydroxy nitrate (ZHN) was prepared via a core-precipitation method, in a typical experiment; zinc oxide (8.1 g, 0.1 mol) was added to 100 cm^3 of a 2.4 M aqueous zinc (II) nitrate solution with vigorous stirring at room temperature for 24 hours. The resultant white precipitate was filtered, washed several times with deionized water and dried in a vacuum oven for 48 hours at about 50° C. Zinc copper hydroxy acetate (ZC-Ac) was prepared by adding 0.41 g of ZnO to 1.00 g of Cu $(CH_3COO)_2 \cdot H_2O$ in 10 ml of deionized (DI) water with vigorous stirring at room temperature and left to stand for 24 hours. The resultant precipitates were filtered, washed several times with deionized (DI) water, and dried at room temperature.

Intercalation of cinnamate (Cn) and isomers of hydroxycinnamate (*n*-HCn), which exist in 3 geometric isomers as shown in Figure 2.2, into precursor LHSs and HDSs was achieved by anion exchange. The conditions for exchange were optimized for each material. To improve solubility in water, the acids (*n*-hydroxycinnamic acid and cinnamic acid) were reacted with an equimollar amount of NaOH in enough deionized water to produce the desired concentration for complete exchange of the precursor anion without observable degradation of the layered material.
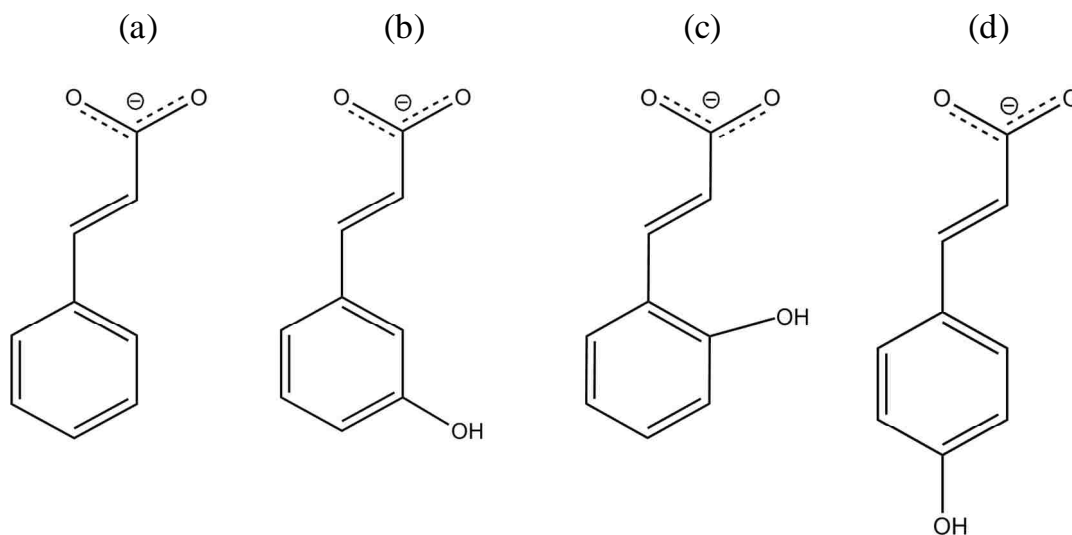
Figure 2.2: Structure of the anions used in this study: (a) cinnamate (Cn), (b) *m*-hydroxycinnamate (*m*-HCn), (c) *o*-hydroxycinnamate (*o*-HCn), (d) *p*-hydroxycinnamate (*p*-HCn).

2.3   Anion Exchange kinetics

The replacement of (hydroxy) cinnamate anions by chloride ions was investigated in the temperature range 30 $^{\circ}$C to 60 $^{\circ}$C. The exchange reactions were performed in a shaking water bath with a temperature stability of ± 0.2 $^{\circ}$C and shaking speed of 300 strokes per minute. Multiple reaction samples were prepared by mixing 0.15 g of LHS or HDS with 15 ml of 1.0 M sodium chloride; samples were continuously agitated in the water bath for a specified time period. After the specified time period, the reaction was quenched by filtration followed by washing of the residue several times with DI water. The filtrate was collected into polystyrene vials, capped and stored for UV-Vis analysis. Solid samples were allowed to dry in air at room temperature prior to PXRD analysis.

2.3.1 Solution Phase Analysis

The concentration of released anions at specified time periods was monitored by UV-Vis analysis. Representative UV-vis spectra are shown in Appendix A, anion concentrations were monitored at the peak of the UV band (Cn, λ_{max} = 269 nm, o-HCn, λ_{max} = 270 nm, m-HCn, λ_{max} = 272 nm and p-HCn, λ_{max} = 287 nm). Calibration curves for calculating (hydroxy) cinnamate concentration in aqueous solutions were determined in the presence of sodium chloride concentrations identical to those used in the exchange reactions. Representative calibration curves are shown in appendix B. The concentrations of released (hydroxy) cinnamate anions at time t, C_t, and the concentration at equilibrium, C_∞, were used to calculate the extent of reaction using equation 2.2.

$$\alpha = \frac{C_t}{C_\infty}$$
Equation 2.2

2.3.2 Solid State Analysis

Solid state transformation of the exchange reaction was monitored by PXRD. The intensity of a given Bragg reflection was obtained by fitting the XRD peaks to a Gaussian or Lorentzian function. The disappearance of the (001) reflection of the (hydroxy) cinnamate phase as well as the growth of the (001) reflection of chloride phase were monitored and the relative intensities of the phases were used to calculate the extent of

reaction for the decay of the host phase (α_{host}) at time (t) based on equation 2.3.

$$\alpha_{host(t)} = \left[\frac{1-\left(\frac{I_{h(t)}}{I_{g(t)}+I_{h(t)}}\right)}{1-\left(\frac{I_{h(\infty)}}{I_{g(\infty)}+I_{h(\infty)}}\right)}\right] \qquad \text{Equation 2.3}$$

In equation 2.3, $I_{h(t)}$ is the intensity of a given Bragg reflection of the host anion at time t, $I_{g(t)}$ is the intensity of a given Bragg reflection of the guest anion at time t, $I_{h(\infty)}$ is the equilibrium intensity of the Bragg reflection of the host anion (determined at equilibrium) and $I_{g(\infty)}$ is the equilibrium intensity of the Bragg reflection of the guest anion.

Chapter 3 :   Use of Isoconversional Analysis in Anion Exchange Kinetics of Nanodimensional Layered Metal Hydroxides

3.1   Introduction

Layered metal hydroxides with exchangeable interlayer anions have found widespread applications in areas such as flame retardadation,[41;48] ion-exchange, magnetism and catalysis,[87-90] and controlled release delivery.[60;62;67;153] Examples of these materials include layered double hydroxides, hydroxy double salts, and layered hydroxy salts. Anion exchange reactions of layered metal hydroxides are useful for creating materials with optimal physico-chemical properties for targeted applications. Also anion exchange reactions can be used as low temperature methods to prepare novel materials which may not be accessible by other techniques, making the characterization of exchange kinetics of practical interest. In addition, understanding the factors that control release of functional anions from these structures is important in designing hosts for storage and triggered release delivery.[67] Perhaps the most widely utilized approach for evaluating kinetics of this class of reactions has been the use of the Avrami-Erofe'ev nucleation-growth model.[109;110] In this model, the extent of reaction (α) is scaled from zero at the start of the reaction to one at the end, and depends upon the rate constant, k, and a coefficient, n, as shown in eqn 1.4.

The Avrami–Erofe'ev model has been applied successfully to a wide range of reactions as discussed in section 1.3. However, this model-based approach is of limited use in cases where there are structural changes occurring during the exchange process.

The Avrami-Erofe'ev model works well in some cases but is not sufficient when the mechanism is not constant over the entire extent of reaction. Thus before applying model based approaches, it is important to ascertain that the reaction is indeed a single process reaction otherwise model based approach might not be application.

A strategy used in thermal analysis studies to identify when fitting to a single model is not an appropriate strategy is to utilize isoconversional methods.[126] Isoconversional methods have been applied successfully in a variety of reactions including thermal degradation kinetics of a variety of materials including polymers and inorganic compounds. Recently the approach has been extended to other reactions which include hydride formation in reactive plasmas.[133] The approach allows for the identification of multi-step reactions in which the relative contributions of individual steps change during the course of the reaction.[111;129] Variation of E_a as a function of the extent of reaction provides information about changes in the reaction mechanism and enables the investigation of reaction mechanisms.[129;130] When a single process is involved, the E_a is constant over the entire conversion range. For isothermal processes, isoconversional methods can be divided into differential methods (equation 1.6) and integral method (equations 1.7).[129;131]

In this study, we report the use of isothermal, isoconversional analysis to examine the anion exchange kinetics of two model reactions which have been chosen to illustrate how the isoconversional approach can be exploited to identify when model-based approaches such as Avrami-Erofe'ev kinetics, are appropriate. The selected examples involve release of cinnamate or hydroxycinnamate anions from HDS and LHS structures

via exchange with chloride anions. Isoconversional analysis is applied to evaluate the rate of anion release into solution as well as changes in solid state structure in order to derive effective activation energies that can be compared to global E_a values obtained from the Avrami-Erofe'ev model fitting method.

3.2 Experimental Methods

3.2.1 Materials

Copper nitrate trihydrate [$Cu(NO_3)_2 \cdot 3H_2O$] (98.0%) and copper acetate monohydrate [$Cu (C_2H_3O_2)_2 \cdot H_2O$] (98.0%) were obtained from Alfa Aesar, trans-cinnamic acid [$C_6H_5CHCHCO_2H$], and trans-*o*-hydroxycinnamic acid [*o*-$(OH)C_6H_4CHCHCO_2H$] (98%), were obtained from Sigma Aldrich Chemical Co. Sodium chloride (100%) and zinc oxide (100%) were obtained from J. T. Baker. Sodium hydroxide (pellets, 98%) was obtained from EMD Chemicals. All materials were used as supplied by manufacturer without further purification.

3.2.2 Preparation of layered compounds

Copper hydroxy-*o*-hydroxycinnamate (C-*o*-HCn) was prepared by mixing 20.0 g of BCN (see section 2.2 for preparation of BCN) with 1000 cm^3 of 0.08 M *o*-hydroxycinnamate (*o*-HCn) solution at room temperature for 48 hours with frequent stirring. The sample was filtered and the exchange reaction repeated two more times using fresh *o*-HCn solutions in order to get complete exchange product. Zinc copper hydroxycinnamate (ZC-Cn) was prepared by mixing 20.0 g of ZC-Ac with 1000 cm^3 of 1.0 M cinnamate (Cn) and allowed to react at room temperature for 8 hours; longer reaction times led to degradation of the layered metal hydroxide.

3.2.3 Characterization of materials

UV-Vis analysis was conducted on a Perkin Elmer Lambda 35 UV-Vis Spectrophotometer using quartz cuvettes with a path length of 1 cm. Infrared spectral data of the synthesized and exchanged materials were obtained on a Perkin Elmer Spectrum 100 FT-IR spectrometer operated at a 2 cm^{-1} resolution in the 4000 - 650 cm^{-1} spectral range; 16 scans were averaged. The FTIR spectra were recorded using a single reflection ATR accessory with a ZnSe prism (PIKE MIRacle^{TM}, from PIKE technology) at an incident beam angle of 45°. Powder x-ray diffraction (PXRD) measurements were recorded in the 2θ range of 2.0^{o} - 45.0^{o}; data acquisition was performed using a step size of 0.0167^{o} per second. The powder samples were pressed in to the trough of glass sample holders.

Thermogravimetric analysis (TGA) was performed on a Netzsch TG 209 F1, TGA instrument described in section 2.1.1. Samples with a weight of 10.0 ± 0.2 mg were placed into aluminum oxide crucibles and heated under a constant flow of nitrogen at a heating rate of 20°C min^{-1} between 40 and 800 ^{o}C. The chain length of Cn and *o*-HCn anions were calculated as described in section 2.1.6. Elemental analysis was performed by Huffman Laboratories, Colorado, using atomic emission spectroscopy interfaced with inductively coupled plasma (AES-ICP) for determination of metals. **BCN: Cu$_{2.3}$(OH)$_{3.6}$(NO$_3$)** [N (4.98% exp 5.13% calc), Cu (52.56% exp 54.28 calc), H (1.34% exp 1.37 calc)]; **ZC-Ac: ZnCu$_{2.8}$(OH)$_{5.3}$(Ac)$_{1.7}$·2.6 H$_2$O** [Zn (14.72% exp 14.15 calc), Cu (35.84% exp 34.44 calc), H (3.25% exp 3.39% calc), C (9.25% exp 8.90% calc)], **C-**

***o*-HCn: Cu$_{2.0}$(OH)$_{2.9}$(o-HCn)$_{1.1}$0·6H$_2$O** [Cu (36.61% exp 35.64 calc), H (3.24% exp 3.25% calc), C (32.94% exp 32.66 calc)]; **ZC-Cn: ZnCu$_{3.2}$(OH)$_{6.1}$(Cn)$_{2.4}$** [Zn (8.81% exp 9.06% calc), Cu (27.8% exp 28.57% cal), H (3.00% exp 3.08% calc), C (35.14% exp 36.11% calc)].

3.3   Results and Discussion

3.3.1   Characterization.

PXRD results for BCN, which has been indexed as the synthetic monoclinic gerhardtite $Cu_2(OH)_3NO_3$ space group $P\ 2_1/m$ (4), (PDF # 45-594),[154] are shown in Figure 3.1. The formula of gerhardtite is in close agreement with the formula obtained from elemental analysis results $\{Cu_{2.3}(OH)_{3.6}(NO_3)\}$ shown in section 3.2.3. Figure 3.1 shows the PXRD patterns for BCN (lower panel) and its exchange product (upper panel). In both cases, the materials show intense $00l$ reflections which are equally spaced indicating that the structures are layered and possess high range ordering, at least to the third order in the c axis direction. The 001-003 Bragg reflections were used to calculate the basal spacing using the Bragg equation.[148] The obtained value of 6.94 ± 0.01 Å for BCN matches literature value of 6.81Å.[155] Upon exchanging nitrate with o-HCn, new 001-003 peaks appear at lower 2 θ values giving an average d-spacing value of 16.813 ± 0.003 Å; an indication of the expansion of the interlayer space. The increase of the interlayer space, from 6.94 Å in BCN to 16.81 Å in C-o-HCn, is consistent with a smaller nitrate anion (thermochemical radius = 1.65 Å,[75]) being replaced by a larger o-HCn anion (chain length = 8.63 Å). The o-HCn anions are either tilted or partially interdigitated within the metal hydroxide layers. The absence of nitrate ion reflections from the C-o-HCn trace indicates that the exchange was complete, consistent with elemental analysis results which gave the C-o-HCn formula as $Cu_2(OH)_3(C_9H_7O_3)_{1.1}\cdot 0.5H_2O$. The metal ion to anion ratios are consistent, within approximately 10%, for a nearly 1:1 exchange.
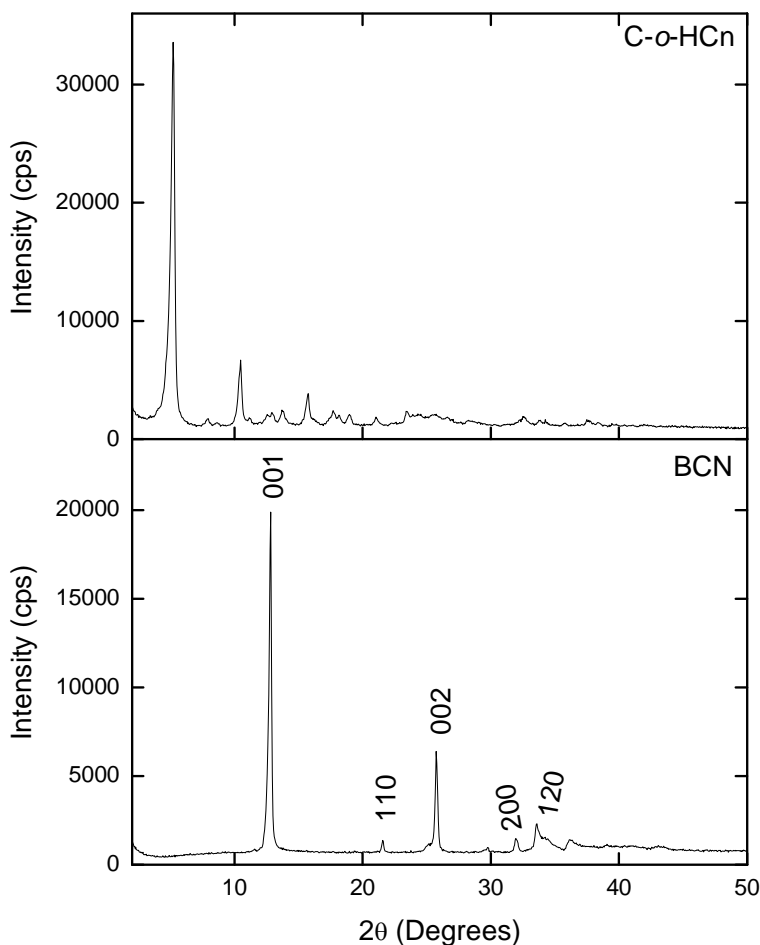
Figure 3.1: PXRD profiles for BCN and C-*o*-HCn

Thermogravimetric (TG) and derivative thermogravimetric (DTG) curves presented in Figure 3.2 shows that CHN undergoes decomposition in one step consistent with results obtained by other workers.[94;155] Single step decomposition may indicate that the temperature at which dehydroxylation of the layers and the loss of the interlayer nitrate is very close and the material undergoes simultaneous dehydroxylation and deanation. The onset of degradation is at around 220°C and peaks at about 247°C in

agreement with literature values.[155;156] The TG curve does not shows significant low temperature mass loss, an indication that the material is anhydrous and may decompose to CuO(s) according to equation 3.1.[155]

$$\textbf{4 Cu}_2\,\textbf{(OH)}_3\,\textbf{NO}_{3(s)} \longrightarrow \textbf{8 CuO}_{(s)} + \textbf{4 NO}_{2(g)} + \textbf{O}_{2(g)} + \textbf{6 H}_2\textbf{O}_{(g)} \qquad \textbf{Equation 3.1}$$
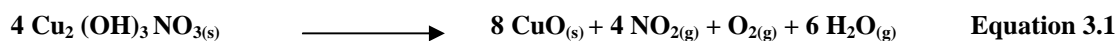
From the above equation the theoretical mass loss for the decomposition of CHN is 33.8%.[94] The experimental value from TG (33.76 %) is the same as the theoretical value and in close agreement with literature values.[94]
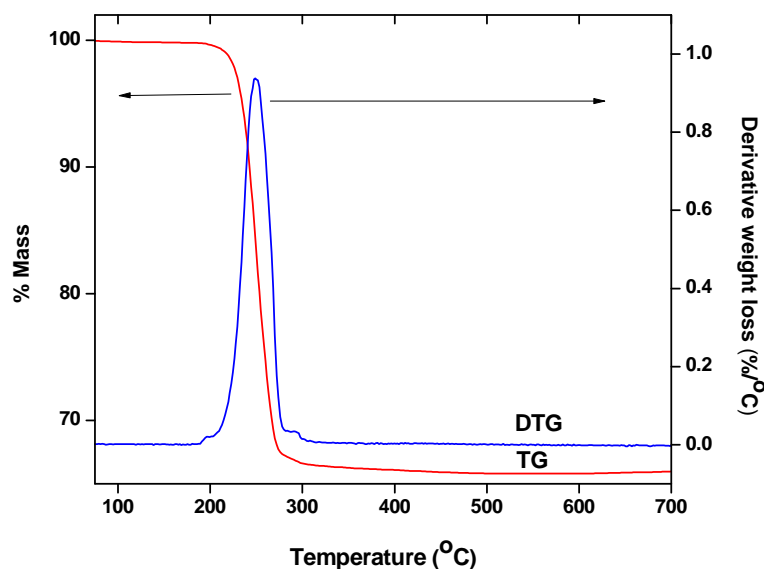
Figure 3.2: TG (red) and DTG (blue) curves of BCN in nitrogen atmosphere at a ramp rate of 20⁰/min

FTIR spectra of BCN (lower panel) and C-*o*-HCn (upper panel) are shown in Figure 3.3. The nitrate group of BCN prepared using similar methods has been shown to be coordinated to matrix copper ion through one of the oxygen atoms. The vibrational frequencies in Figure 3.3 are in agreement with those obtained by other workers and have been assigned as follows; 1049 cm^{-1}, N-O stretching (ν_2); 1338 cm^{-1}, O-NO$_2$ symmetric

stretch (ν_1); 1425 cm^{-1}, O-NO$_2$ asymmetric stretch (ν_4).[155;157] The presence of two O-NO$_2$

stretching peaks is consistent with vibrations of coordinated nitrate groups of C_{2v}

symmetry. Coordination of the nitrate group to matrix copper ion through one of the

oxygen atoms reduces the symmetry of the nitrate ion from D_{3h} in free nitrate to C_{2v}

resulting in splitting of the doubly degenerate NO$_2$ stretch (ν_3, 1360-1380 cm^{-1}) in free

nitrate.[157] A set of new peaks appear in the exchange product corresponding to the

presence of o-HCn in the gallery and the nitrate vibrational peaks disappeared, indicating

complete exchange consistent with PXRD and elemental analysis results. The new peaks

appear at 1639 cm^{-1} (C=C bond vibration of the α,β-unsaturated carboxylate group), 1540

cm^{-1} and 1417 cm^{-1} (ν_{asym} C=O and ν_{sym} C=O respectively). There is extensive hydrogen

bonding in C-o-HCn as indicated by the appearance of broad peaks and the disappearance

of the sharp peaks in the OH stretching region (3650 cm^{-1} – 3000 cm^{-1}).

Thermogravimetric analysis and elemental analysis results (section 3.2.3)

demonstrate that the BCN precursor does not have a significant amount of intercalated

water, whereas C-o-HCn does contain some associated water molecules which may

reside within the interlayer space. The appearance of broad absorption peaks in C-o-HCn

may be due to the presence of interlayer water molecules which form hydrogen bonds

with free layer hydroxyl groups or o-HCn molecules. The broad peaks may also be due to

hydrogen bond network between layer hydroxyl groups and o-HCn hydroxyl groups.

Broad absorption bands in the OH stretching region have been shown to disappear with

hydrous - anhydrous transformation, with the subsequent appearance of sharp absorption

bands around 3600 cm^{-1}.[158]
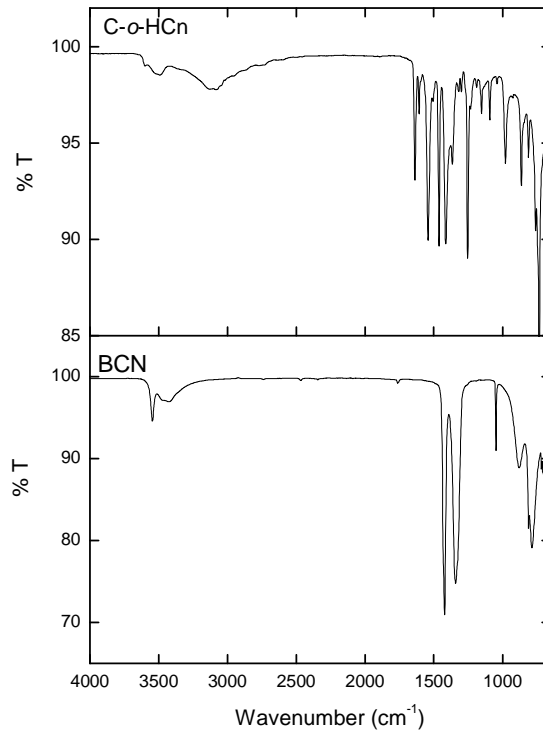
Figure 3.3: ATR-FTIR profiles for BCN and C-*o*-HCn

ZC-Ac prepared in this work is layered and posses high range ordering in the *c* direction as shown in the lower panel of Figure 3.4; the PXRD profile show intense *00l (l* =1 to 3) Bragg reflections which are equally spaced. The interlayer distances of 9.43 ± 0.03 Å obtained for ZC-Ac is comparable to literature values (9.3 Å and 9.46 Å) reported for material prepared using the same method.[25;116] When the acetate anions in ZC-Ac were replaced by Cn ions, a shift of the Bragg reflections to lower 2 θ values was observed indicating expansion of the interlayer space with the interlayer distance increasing to 20.21 ± 0.09 Å. The increase in the basal spacing is consistent with a

smaller ion (acetate ion chain length = 2.53 Å) being replaced by a larger anion (Cn chain

length = 8.62 Å) with the cinnamate anions adopting a close to bilayer orientation.
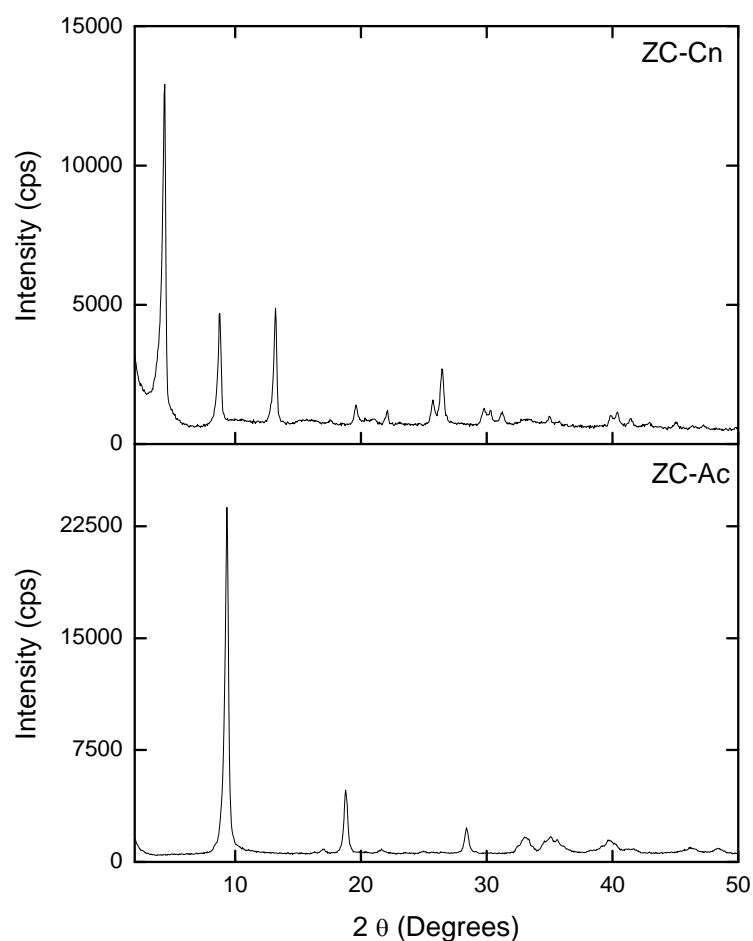
Figure 3.4: PXRD profiles for ZC-Ac (lower trace) and ZC-Cn (upper trace)

Thermal analysis results of ZC-Ac presented in Figure 3.5 shows low temperature

weight loss which may be due to loss of surface and intercalated water. This dehydration

process results in 8 % mass loss and is confirmed by the endothermic peak observed in

DSC (curve B). A second endothermic peak at 202 ^{o}C has been shown to be due to

deanation and dehydroxylation, with the processes occurring simultaneously.[159] The final

two exothermic steps are due to deanation and possibly thermal degradation of acetate anions. Exchanging acetate ions in ZC-Ac with cinnamate ions resulted in exclusion of intercalated water as shown in Figure 3.6 A in which there is no significant low temperature weight loss in the TG traces. The dehydroxylation and deanation temperatures are close, with the processes occurring at 235 $^{\circ}$C and 253°C respectively as confirmed from the endothermic and exothermic transitions in DSC trace (Figure 3.6 B). Thermal degradation of the anion occurs at higher temperatures resulting in 51 % weight loss.
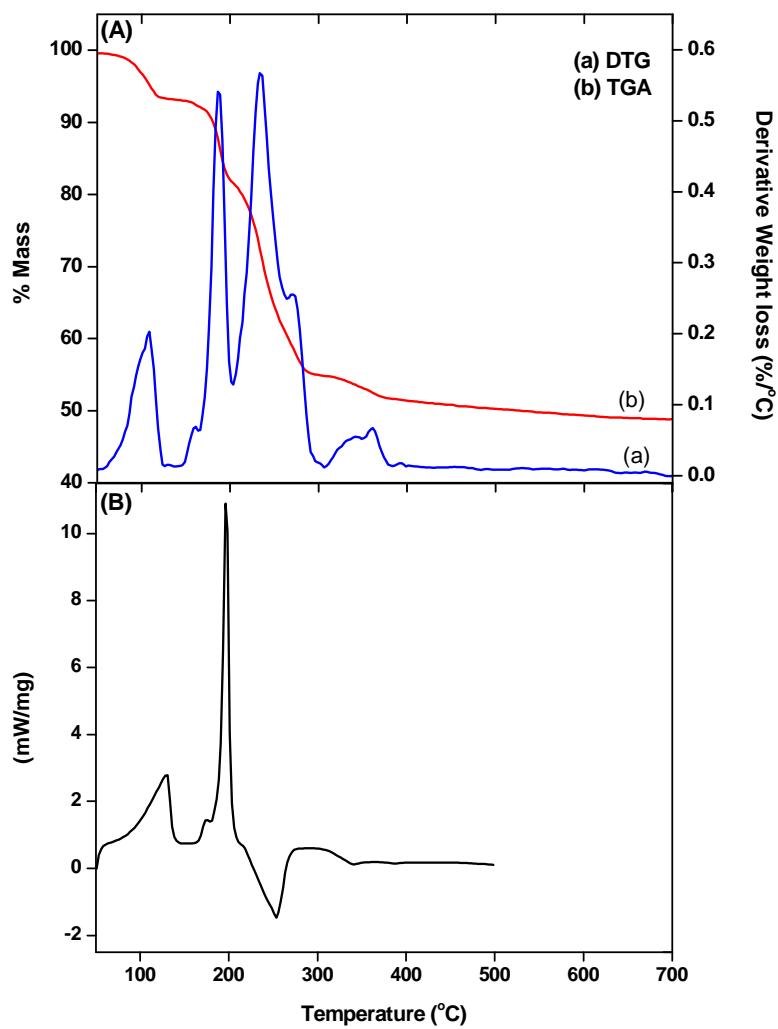
Figure 3.5: (A) DTG (a), TG (b) and (B) DSC curves for ZC-Ac degraded in nitrogen at a heating rate of 20°C min⁻¹
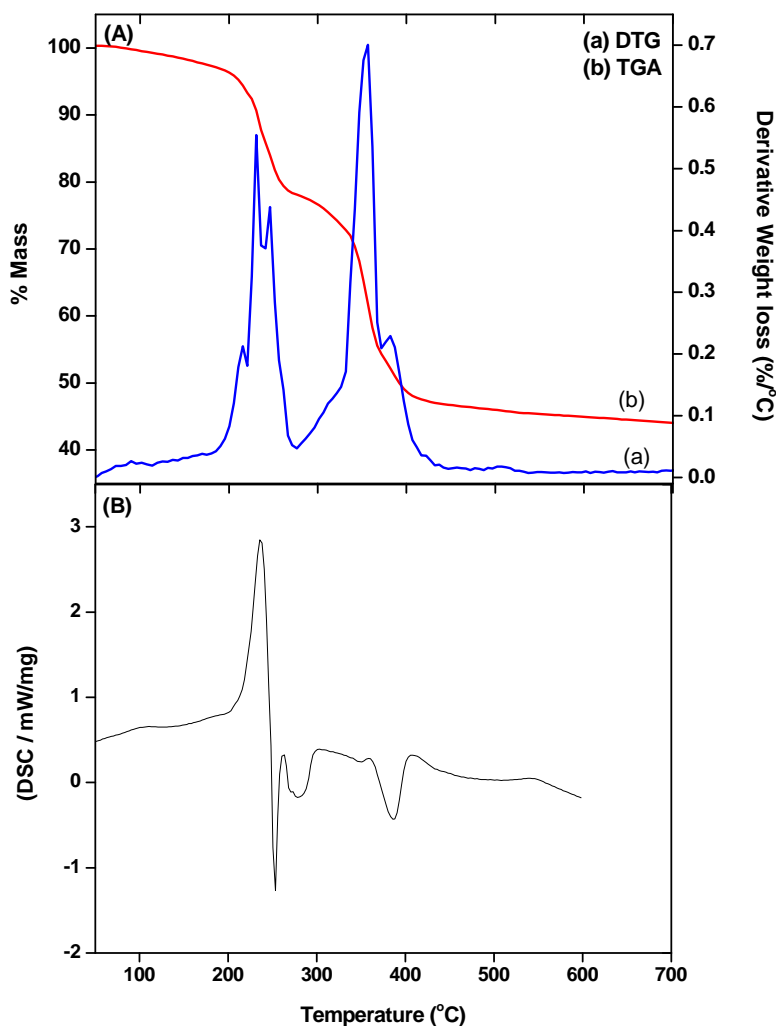
Figure 3.6: (A) DTG (a), TG (b) and (B) DSC curves for ZC-Cn degraded in nitrogen at a heating rate of 20°C min^{-1}

ZC-Ac has high levels of hydrogen bonding as shown in the IR spectra presented in Figure 3.7; the presence of the broad peak centered around 3400 cm^{-1} is indicative of O-H stretching vibrations of hydrogen bonded water and/or layer hydroxyl groups. The presence of intercrystalline water molecules in ZC-Ac has been confirmed from elemental analysis results {obtained formula; $ZnCu_{2.8}(OH)_{5.3}(Ac)_{1.7} \cdot 2.6\ H_2O$}, and TGA

results discussed previously. Exchanging acetate with Cn ions resulted in the loss of intercalated water as indicated from TGA results and elemental analysis data which gave the formula as $ZnCu_{3.2}(OH)_{6.1}(Cn)_{2.4}$. FTIR results (Figure 3.7) show that the broad band in the hydroxyl stretching region of ZC-Ac was replaced by a single sharp peak at 3577 cm^{-1} in ZC-Cn consistent with losing water of intercalation resulting in the layer hydroxyl groups being free.[158] Upon intercalation of Cn, peaks due to C=O vibrations of acetate ion in ZC-Ac (υ_{asym} = 1563 cm^{-1} and υ_{sym} =1410 cm^{-1}) were replaced by a series of peaks due to Cn vibrations (1642 cm^{-1}, C=C bond vibration of the α,β-unsaturated carboxylate group; 1551 cm^{-1}, υ_{asym} C=O and 1428 cm^{-1}, υ_{sym} C=O) indicating complete replacement of acetate ions with Cn ions.
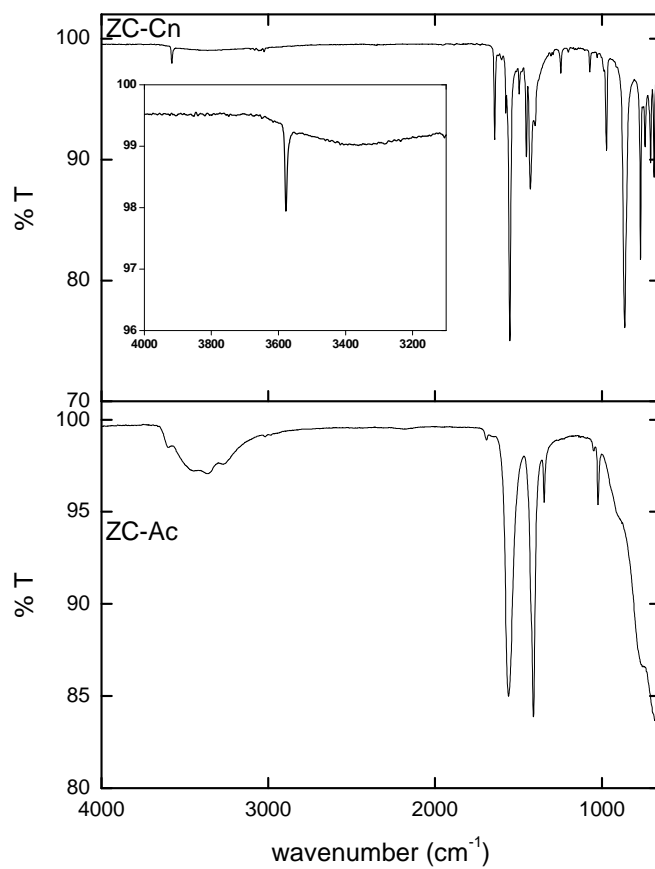
Figure 3.7: ATR-FTIR profiles for ZC-Ac (lower trace) and ZC-Cn (upper trace).

3.3.2 Kinetic analysis

Anion exchange reactions in clays are generally viewed as topotactic with the overall structural integrity being maintained during the reaction although the nature of the lamellar structure and the anions involved can result in a dissolution-reprecipitation mechanism.[160] Tapotactic exchange reactions may involve multiple steps which include;

- Transport of the guest ions in the bulk solution and their subsequent diffusion across the liquid film surrounding the lamellar compound;

- Diffusion of the guest within the interlayer space to completely fill the space;

- Chemical reaction at exchange sites within the layers;

- Diffusion of the host anion (displaced from the layers) in the interlayer space and its subsequent diffusion in the bulk solution away from the lamellar compound.

3.3.2.1   C-*o*-HCn Exchange Kinetics

PXRD analysis of the solid samples obtained during the exchange reaction provides insight into the transformation of both the guest phase and the host phase during the reaction. Selections of traces at different time periods for all the temperatures are shown in Figure 3.8. In addition to reflections from *o*-HCn, new reflections that increase in intensity with time appear at higher 2θ values. These reflections are assigned to layered products containing intercalated Cl⁻ ions. There are two Cl⁻ phases, with the one with higher intensity (major phase) being indexed as monoclinic botallackite $\{Cu_2(OH)_3Cl\}$, space group $P2_1/m$ (11), PDF # 58-520 and the minor phase (lower

intensity) was indexed as monoclinic clinoatacamite {$Cu_2Cl(OH)_3$}, space group $P2_1/n$ (14), PDF # 50-1559.[154] The botallackite phase has a *001* peak at $2\theta = 15.5^o$ corresponding to a d-spacing of 5.74 ± 0.049 Å which is in close agreement with reported value for $Cu_2(OH)_3Cl$ of 5.726 Å,[30] the clinoatacamite phase *011* peak at 16.2^o corresponding to a d-spacing of 5.29 ± 0.03 Å is in agreement with reported value of 5.47 Å.[15] The assignments have been confirmed by examining higher angle data of a representative spectrum shown in Figure 3.9. In Figure 3.8, the *o*-HCn phase is marked by closed diamonds, botallackite phase by closed circles and the clinoatacamite phase by closed squares. As expected for release kinetics, the intensity of the Cl^- phases (guest anion) increase with time while the *o*-HCn phase intensity (host anion) decrease relative to the Cl^- phase. The reaction does not go to completion since the Bragg reflections from the *o*-HCn phase are still observed at equilibrium (t_∞).
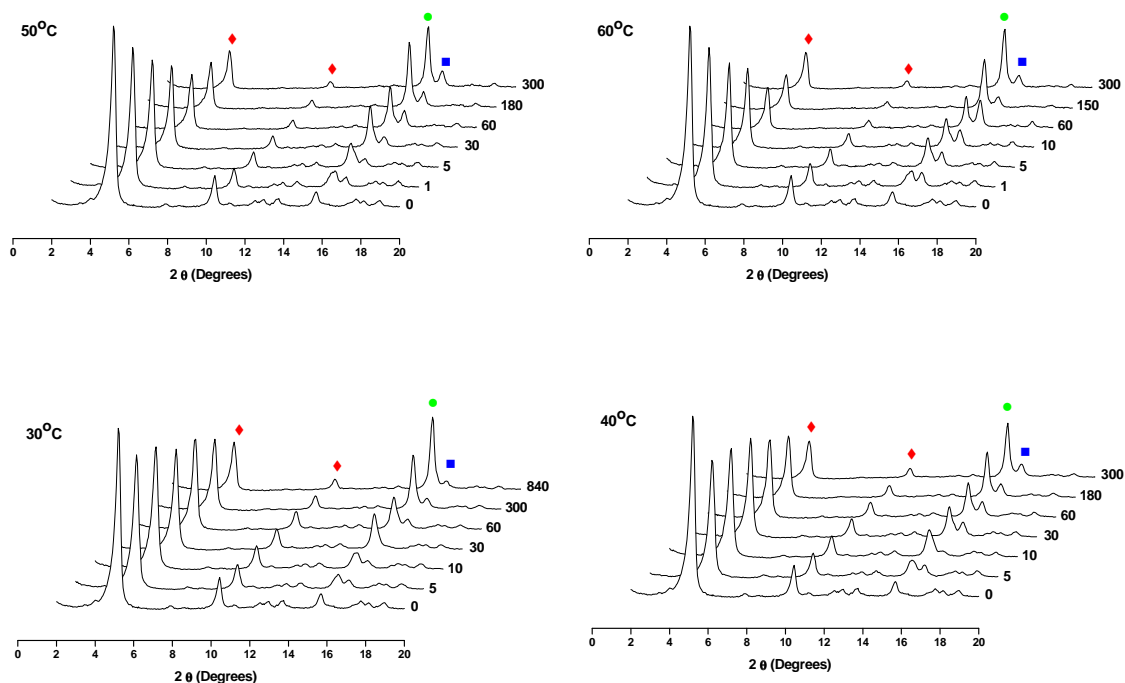
Figure 3.8: PXRD profile for solid samples collected at different times and at different temperatures for the C-*o*-HCn /Cl⁻ reaction. The *o*-HCn phase is represented by closed diamonds, botallackite phase by closed circles and the clinoatacamite phase by closed squares

The intercalation mechanism in layered materials has been shown to involve staging in materials with flexible layers such as graphite intercalation compounds (GIC), this phenomenon of staging involves filling of every n^{th} layer in the nth stage compound.[161] Staging has been postulated to be a mechanism for lowering of the activation energy for intercalation and exchange reactions.[162] Although the layers in clays are too rigid for staging to occur,[163;164] the phenomenon has however been observed in a few LDH systems where only 2nd stage compounds have been formed. In LDHs, staging depends on the intercalated anions and the composition of the layers.[120;123;162;165;166]

Second-stage compounds contain alternating interlayers occupied by different anions.

Only first-order staging was observed in this study since the XRD profiles did not show

series of 00l basal reflections at 2 θ positions corresponding to the sum of the interlayer

space of the starting material and the fully exchanged product (for 2nd order stage

compound) as shown in Figure 3.8. The absence of higher order staging may indicate that

the interaction between the layers and the initial anion are strong as compared to the

layer-guest interaction resulting in a small reduction in the E_a being attained through

staging.[166]
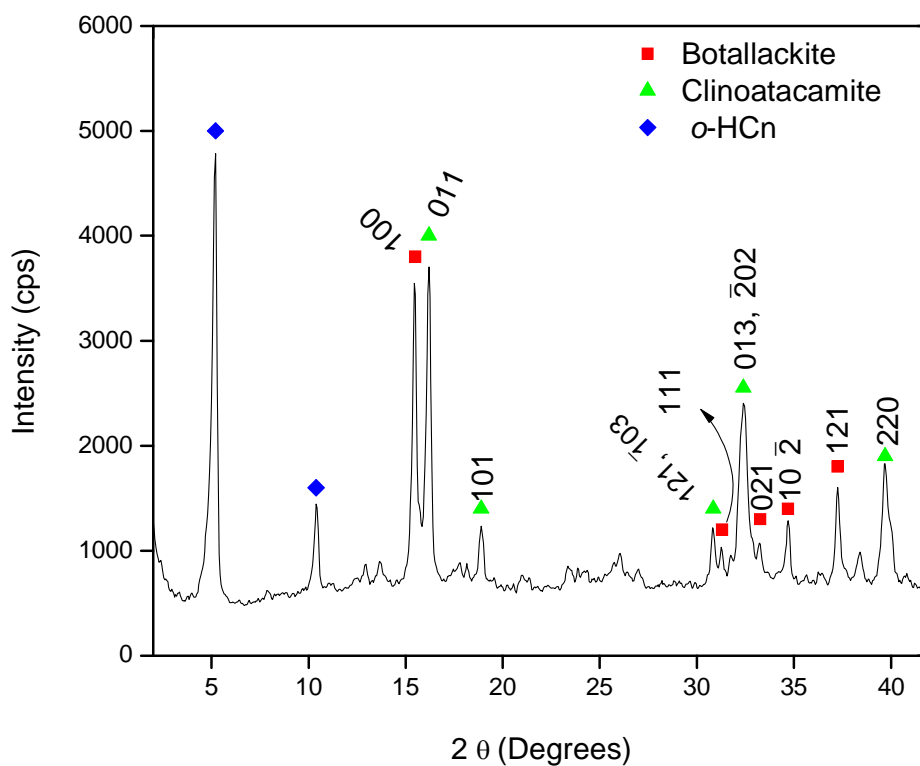
Figure 3.9: XRD profile of C-*o*-HCn exchanged with chloride for 60 minutes at 60°C. *o*-HCn phase is represented by closed diamonds, botallackite phase by closed squares [PDF# 58-520] and clinoatacamite phase by closed triangles [PDF# 50-1559].

The extent of reaction as a function of time plots obtained from solid state transformations at different temperatures are shown in Figure 3.10. The sum of peak heights of the *001* botallackite and the *011* clinoatacamite reflections was used to determine the product $I_{g(t)}$ values. The extent of reaction versus time data were fit to the Avrami –Erofe'ev nucleation-growth model (Equation 1.4); the model provided good fit within the range of α of 0.15-0.85 as has been observed for other intercalation reactions in layered materials.[75;116] Corresponding double-logarithmic plots shown in Figure 3.10 have R^2 values ranging from 0.986 to 0.996 and are almost parallel with an *n* value of approximately 0.5 indicating that, for the temperature range used here, the mechanism is the same and consistent with being diffusion controlled.[115]
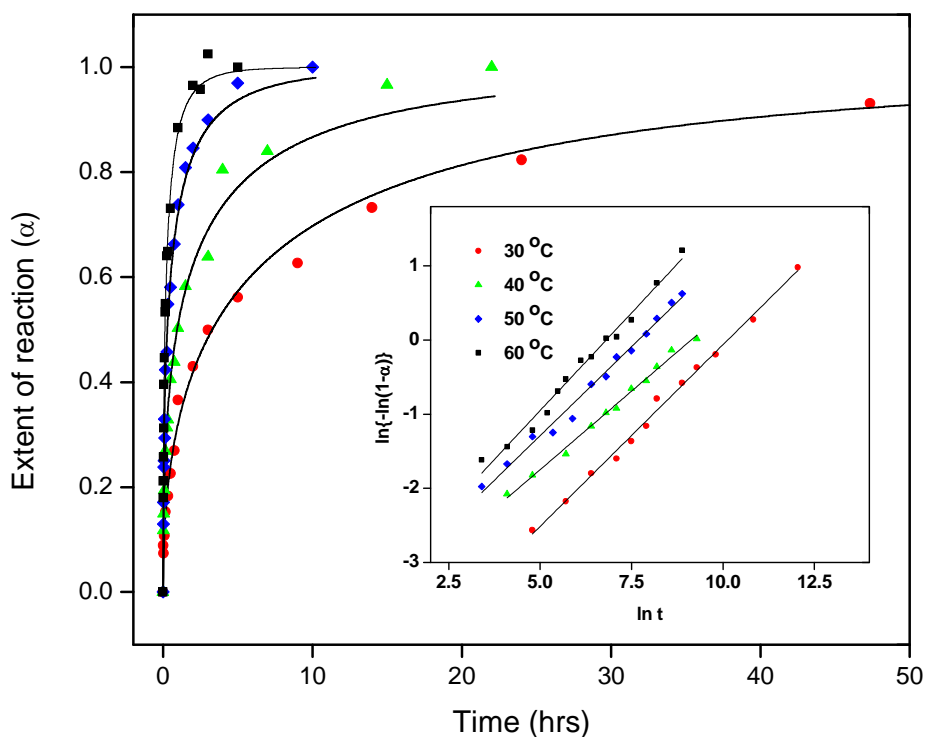
Figure 3.10: Extent of reaction as a function of time for the exchange reaction of Cl⁻ anion and C-*o*-HCn at various temperatures for solid state analysis: 60 °C (■), 50 °C (♦), 40 °C (▲), 30 °C (●), the extent of reaction data has been fitted to Avrami –Erofe'ev equation (solid lines). Insert shows corresponding double-logarithmic plots

UV-Vis spectroscopy was used to determine the accumulated amounts of *o*-HCn

in the filtrate, and hence the amount of host anion released into solution. Since the

Avrami–Erofe'ev model has been successfully applied to liquid phase UV-Vis and NMR

data of released anions,[67;116;167] it was also applied here to the solution data in order to

determine whether the model provides a good description of the release process. The

release profiles are shown in Figure 3.11 together with the corresponding double-

logarithmic plots. The double-logarithmic plots are linear for all the temperatures used

here which is an indication that the Avrami–Erofe'ev model provides a good description of the liquid phase data within the range 0.15<α<0.85. The resulting fits are represented by solid lines in the profiles shown in Figure 3.11. Similar to the solid phase transformation results, the *n* values are again consistent with a diffusion controlled process. Calculated rate constants (*k*) and Avrami *n* coefficients are provided in Table 1 for the kinetics of solid state transformation and the anion release into solution.
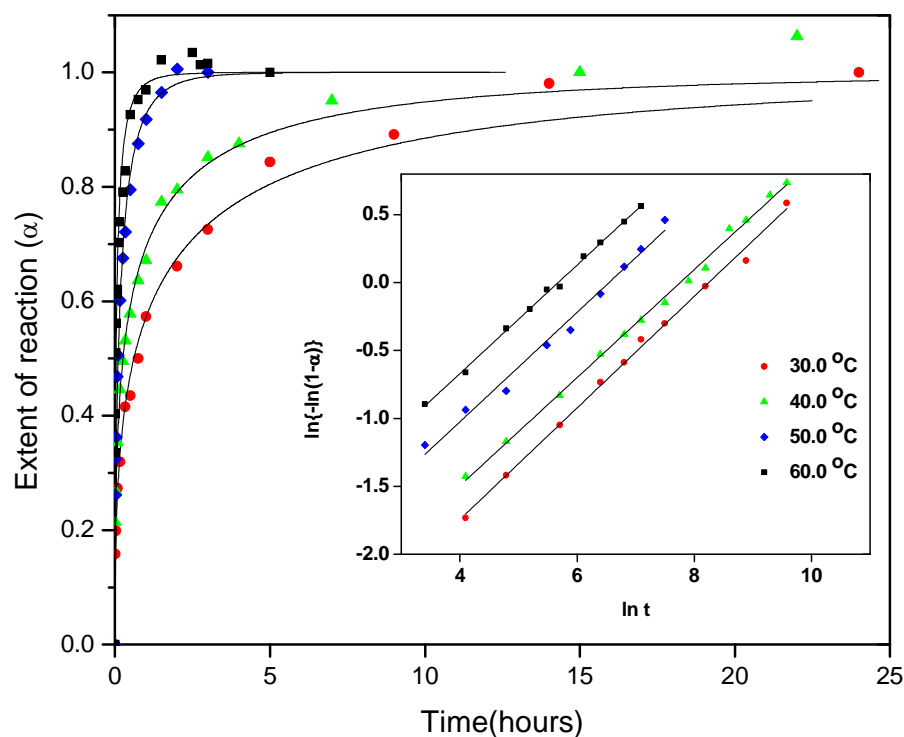
Figure 3.11: Extent of reaction as a function of time for the exchange reaction of C-*o*-HCn at various temperatures for solution analysis: 60 ºC (■), 50 ºC (♦), 40 ºC (▲), 30 ºC (●), the extent of reaction data has been fitted to Avrami –Erofe'ev equation. Insert shows corresponding double-logarithmic plots

As observed in Table 3.1, the rate constants obtained for anion release into solution are three to four times larger than the corresponding rate constants for the solid state transformation. This is to be expected since for each given time period, the extent of reaction for the solution data is higher than that of the solid state transformation, up to the end of reaction. The differences between solution analysis and solid state transformation may indicate that the loss of the host anions and subsequent loss of coherent diffraction from the host phase occurs faster than the gain in coherent diffraction from the product phase. This has been observed in other systems and maybe due to the presence of an intermediate with poor crystallinity [168] or a delayed appearance of the guest phase which may be because a significant number of layers have to be filled with the guest to observe Bragg reflection from the guest phase.

Table 3.1: Summary of solid state and solution analysis kinetic parameters obtained from the Sharp Hancock analysis for the reaction of C-*o*-HCn at different temperatures.

Temperature/ °C	Solid state		solution phase	
	n	$k\,s^{-1}(*10^{-4})$	*n*	$k\,s^{-1}(*10^{-4})$
60.0	0.52 ± 0.02	11 ± 3	0.397 ± 0.006	29 ± 4
50.0	0.48 ± 0.01	4 ± 1	0.45 ± 0.02	16 ± 4
40.0	0.45 ± 0.01	1.3 ± 0.2	0.39 ± 0.06	4.3 ± 0.7
30.0	0.45 ± 0.01	0.4 ± 0.1	0.40 ± 0.01	1.6 ± 0.4

Since higher order staging was not observed in this study, the onset of the exchange reaction may then occur from the outermost layers, and parallel to the layers as observed in the intercalation of NH_3 into TaS_2[169] and deintercalation of mercury from

TiS_2.[170] Johnsen *et al.* [171] observed a similar effect in the exchange reaction of chloride into carbonate containing LDH. The exchange reaction then progressively proceeds to layers closest to the outer layers resulting in a mixture of layers, with some occupied by the host anion and others occupied by the guest anion giving the mixed phases with different interlayer separations observed in XRD profiles.[172] The progressive increase in the number of layers occupied by the guest anions results in the growth of the guest phase and the decay of the host phase with time as observed in XRD profiles. Since anion exchange reactions proceeds from layer to layer and a smaller anion is replacing a larger anion coupled with the rigidity of the HDS layers, the layers will collapse to the interlayer dimension of the guest phase when all the host anions in the layers have been replaced. Unless the complete exchange within the individual layers is instantaneous, the growth of the guest phase and the decay of the host phase may be delayed while at the same time host anions will be released into solution. As such, some of the C-*o*-HCn may be consumed and significant amount of *o*-HCn released into solution without subsequent appearance of guest diffraction peaks.[166;173;174] Due to the ex-situ nature of the experiment, the decay of the host phase was referenced to the growth of the guest (chloride) phase in obtaining the extent of reaction as shown in equation 2.3. The rate of decay of the host phase and the growth of the guest phase are therefore interlinked to give the observed rate constants. The low rate of growth of the chloride phase due to factors indicated above will affect the extent of reaction values obtained, resulting in the observed lower rates of reaction compared to solution analysis.

The temperature dependence of the reaction was evaluated via Arrhenius plots which are shown in Appendix B. The value of the effective activation energy was 91 ± 3 kJ /mol for the solid phase transformation and 84 ± 5 kJ /mol for solution analysis. These values are not significantly different indicating that the temperature dependence obtained from these two approaches is comparable. When the chemical reaction at the exchange sites is rapid, the transport process (by diffusion) then determines the overall rate of reaction. Diffusion-controlled processes have been shown to have varying E_a values, although the value for diffusion of ions in water is low (approximately 15 kJ mol^{-1}),[175] values for surface adsorption processes are generally considered to be as high as 30 kJ mol^{-1}.[176] During the sorption of 2,4-Dichlorophenoxyacetate on various clays, Haque *et al.* [177] observed E_a values ranging from 12-21 kJ mol^{-1}. Lv *et al.* [81] obtained two E_a values for the two-step removal of fluoride ions from solution using an LDH. In the study by Lv *et al.* the fast first step was considered to be diffusion controlled and had an E_a value of 37 $kJmol^{-1}$ while the second slower step with an E_a value of 72 kJ mol^{-1} was proposed to be controlled by the chemical reaction of F^- with the LDH layers.[81] The E_a values for 2-dimensional (2-D) diffusion within the layers can be high depending on the nature of the interlayer species and how densely packed the anions are. When the interlayer species are organic anions, the diffusion through the organic matrix may resemble diffusion through polymers in which the E_a values can be high and in some instances above 100 kJ mol^{-1} depending on the diffusing molecule.[178] In ion exchange reactions in lamellar compounds, Ragavan *et al.*[75] found an activation energy of 43 kJ mol^{-1} for the diffusion controlled intercalation of 4-chlorophenoxyacetate and 53-62 kJ mol^{-1} for intercalation

reactions presumed to be controlled by nucleation at the edge of the layers, based on Avrami model results. The E_a values for processes controlled by reactions of the anions with the lamellar compounds have been shown to range from 30-70 kJ mol^{-1} depending on the nature and size of the guest anions, with larger anions having higher E_a values.[75;168;179]

While model-fitting methods can frequently be utilized to provide insight into the potential mechanism of a reaction, the rate constants depend largely on the functional form chosen and can vary among different models.[124] Use of a single model to obtain a global, effective activation energy for the entire reaction time may also not be appropriate for complex reactions such as structural transformations in polycrystalline layered metal hydroxides. Isoconversional analysis offers the advantage of being able to determine the variation of activation energy as a function of reaction progress; this provides information regarding how the reaction mechanism may change as a function of extent of reaction.[126] The results obtained from isoconversional analysis for solid state analysis and solution analysis are shown in Figure 3.12 and Figure 3.13, respectively. The E_a values obtained for solid state data range from 87 – 96 kJ mol^{-1} and those for solution analysis range from 78-85 kJ mol^{-1}. The data for both solid state and solution analysis reveal that, within experimental error, the E_a does not significantly change as a function of extent of reaction. This is an indication that the reaction proceeds via a single mechanism. This is consistent with the fact that the Avrami *n* values did not vary significantly as a function of temperature for each data set. The E_a values obtained from the Avrami-Erofe'ev analysis lie within the range of values obtained using isoconversional method, indicating

that in this case the model fitting approach provides reliable averaged global effective activation energy for the entire reaction. As noted above, the E_a values obtained are too high to be explained by diffusion of ions in solution alone, 2-D diffusion in a densely packed interlayer region may explain the high E_a values obtained here. Results from Avrami-Erofe'ev model kinetics are consistent with diffusion control, however one cannot rule out a mechanism controlled by reaction at the exchange site. In basic copper nitrate the layers are not charged, the interlayer anions are introduced as a result of the substitution of a quarter of the hydroxyl groups on the brucite type layers and they are thus grafted onto the layers.[29] Since it is expected that the covalent bond between copper and the *o*-HCn carboxylate oxygen is strong, the E_a values at the exchange sites are expected to be high since the reaction involves breaking of covalent bonds. The constant E_a as a function of extent of reaction could be consistent with the mechanism in which the rate is determined by the reaction at the exchange site and thus the mechanism remains the same throughout the reaction. Since E_a does not vary as a function of extent of reaction, model-fitting analyses can be adequate to describe the release kinetics for this system.
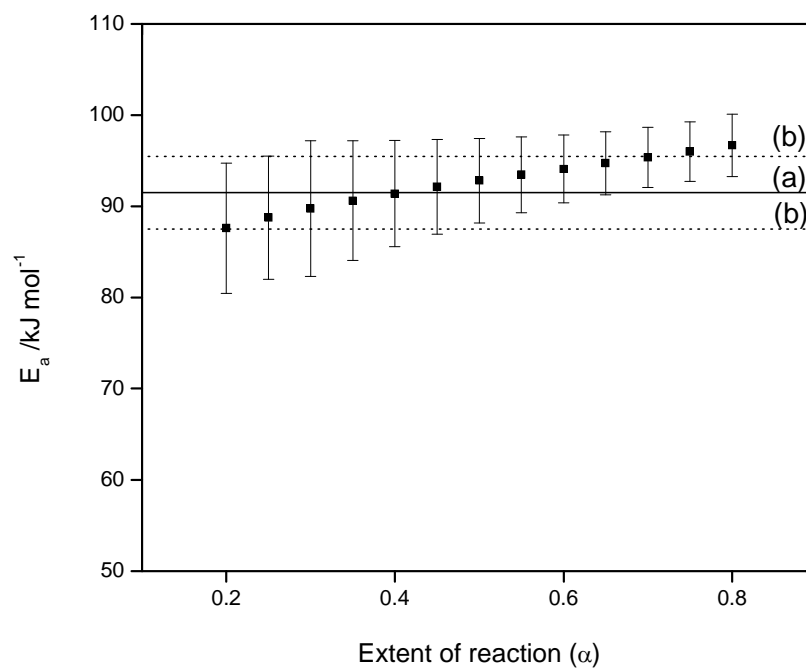
Figure 3.12: Variation of effective E_a with α for solid state analysis. The solid line (a) represents the Arrhenius determined E_a together with the associated errors (broken lines, b)
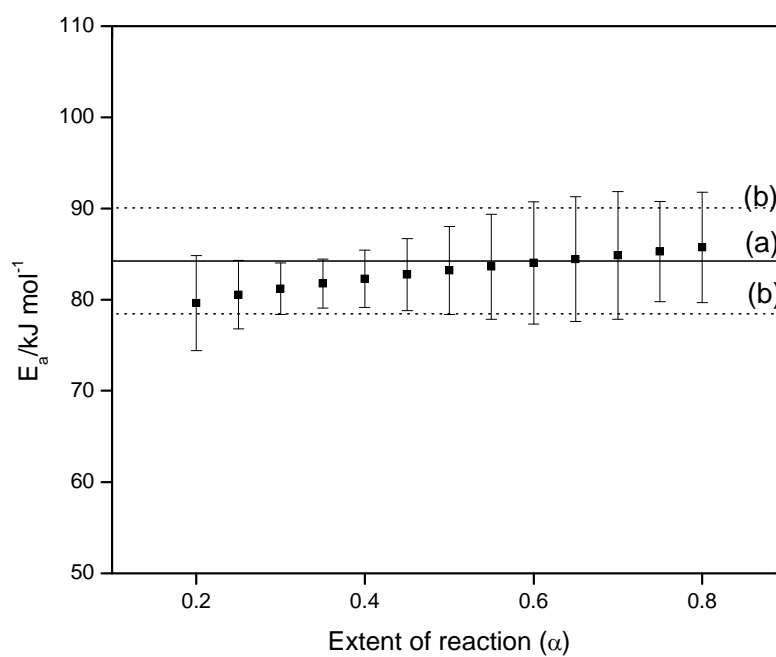
Figure 3.13: Variation of effective E_a with α for solution analysis. The solid line (a) represents the Arrhenius determined E_a together with the associated errors (broken lines, b).

3.3.2.2   ZC-Cn Exchange Kinetics.

The solid state transformation of both the guest and the host phases during the replacement of Cn by chloride in the ZC-Cn HDS host are shown in Figure 3.14, with the chloride phase indicated by an arrow. There is a small induction period observed at low temperatures (30 ^{o}C and 40 ^{o}C) as seen in Figure 3.14. Induction periods have been observed for other anion exchange reactions[123] and maybe due to restructuring of the host layers which results in a delayed or slow release of the Cn anions and subsequent delayed crystallization and/ or growth of the guest phase. During the induction period, the chloride phase is not observed for a period of up to 5 minutes at 30 ^{o}C, and then starts to grow slowly with Bragg reflections having very low intensities in samples obtained for reaction times less than 20 minutes. This effect is also observed in solution analysis where there was linear and slow increase in the concentration of released Cn in the first 30 minutes (insert in Figure 3.16).
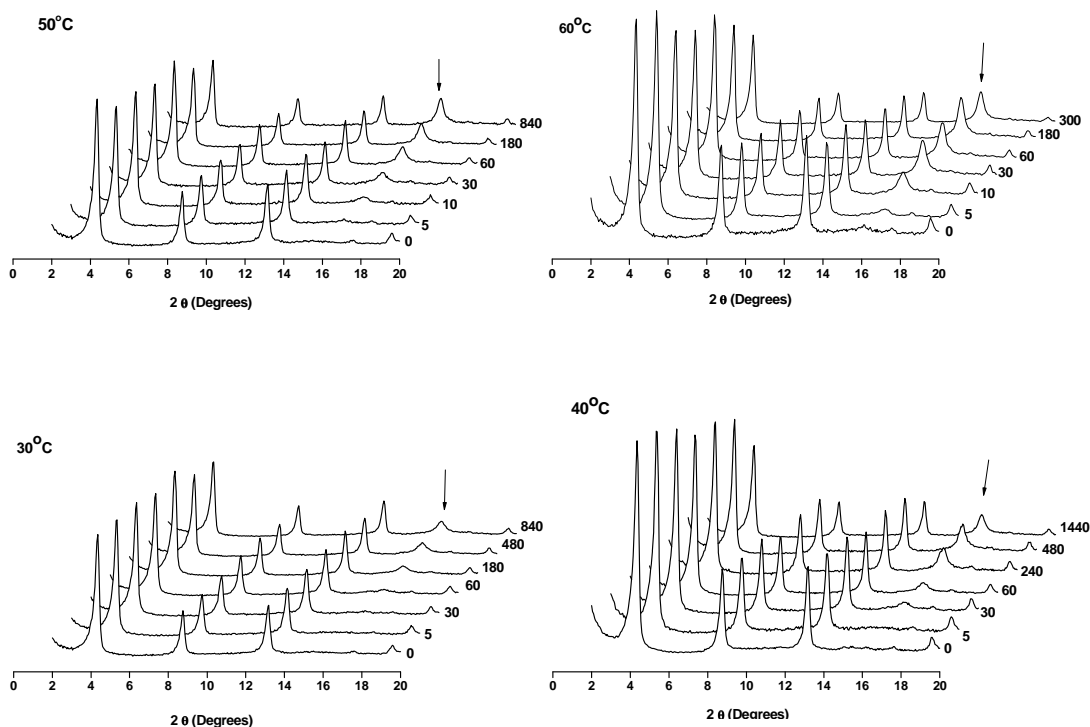
Figure 3.14: PXRD profile for solid samples collected at different times and different temperatures for the reaction of ZC-Cn with chloride anion. The chloride phase is indicated with an arrow.

Possibilities for the slow release of Cn ions without corresponding growth of guest phase include (1) that there were Cn anions present on the edges of interlayer region of the material, or (2) that there where protonated Cn molecules adsorbed on the surface. Only trace amounts of Cn were released when the material was placed in DI water at 40 $^{\circ}$C for 24 hours without any sodium chloride present, much less than the amount released during the induction period. This suggests that the anions released during the induction period were ions on the edges and surface of the lamellar compounds which were exchanged by chloride ions in solution. The chloride phase, which has been indexed as paratacamite, zincian (PDF # 50-1558),[154] has a first peak

(101) at $2\theta = 16.15^{\circ}$ corresponding to a d-spacing of 5.47 ± 0.01 Å which is in agreement with the literature value of 5.45 Å.[180] More detail concerning the phase assignment is shown in Figure 3.15. Similar to the C-o-HCn system, only the first stage compound was observed. The absolute extent of reaction for the exchange is low as indicated by the high intensity of the Cn phase in relation to the guest phase (chloride) at equilibrium. For anion exchange reactions, there are a number of factors which affect the affinity of the HDS layers for guest anion; these include layer-host anion interactions, layer-guest anion interactions, host anion-guest anion interactions within the interlayer space, and the solvation energies of both the host and guest anions. These factors could have resulted in a low equilibrium constant for the exchange reaction.
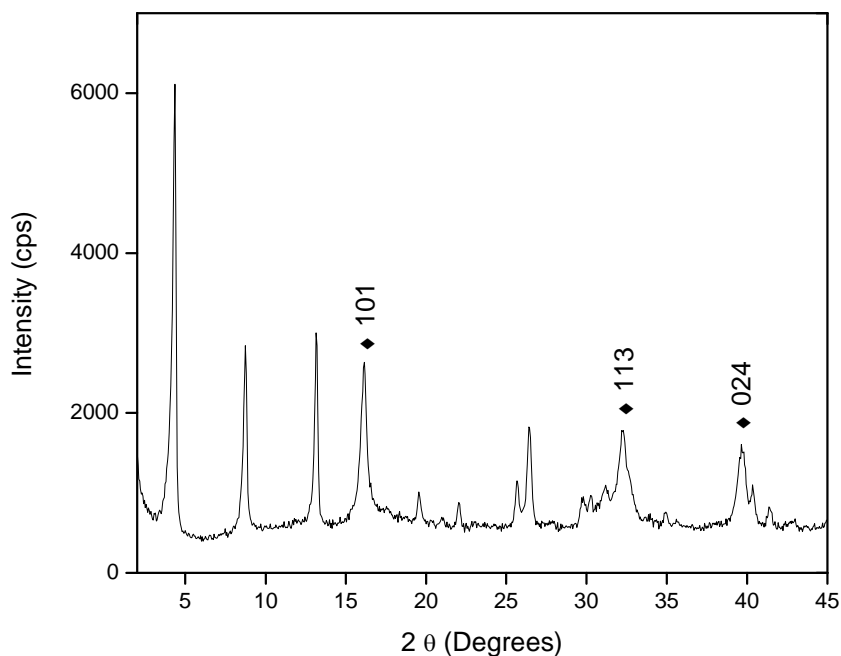
Figure 3.15: XRD profile of ZC-Cn exchanged with chloride for 60 minutes at 50°C. Chloride phase has been indexed as paratacamite represented by closed triangles [PDF# 50-1558].

The extent of reaction versus time plots for solid state transformations at different temperatures are shown in Figure 3.16, the data were again fit to the Avrami–Erofe'ev nucleation-growth model (solid line) using double-logarithmic plots (Figure 3.17). While linear double-logarithmic plots were obtained, the Avrami–Erofe'ev model does not extrapolate to fit the induction region $\alpha< 0.15$ for the lower temperatures, as is evident in the insert in Figure 3.16. The Avrami exponent obtained in this analysis ranged from 0.6 to 0.9, indicating that for the temperatures 30 ^{o}C and 40 ^{o}C (n $\approx$ 0.6) the reaction appears primarily diffusion controlled and for 50 and 60 ^{o}C (n $\approx$ 0.9) there may be contributions from both diffusion and nucleation.[116]
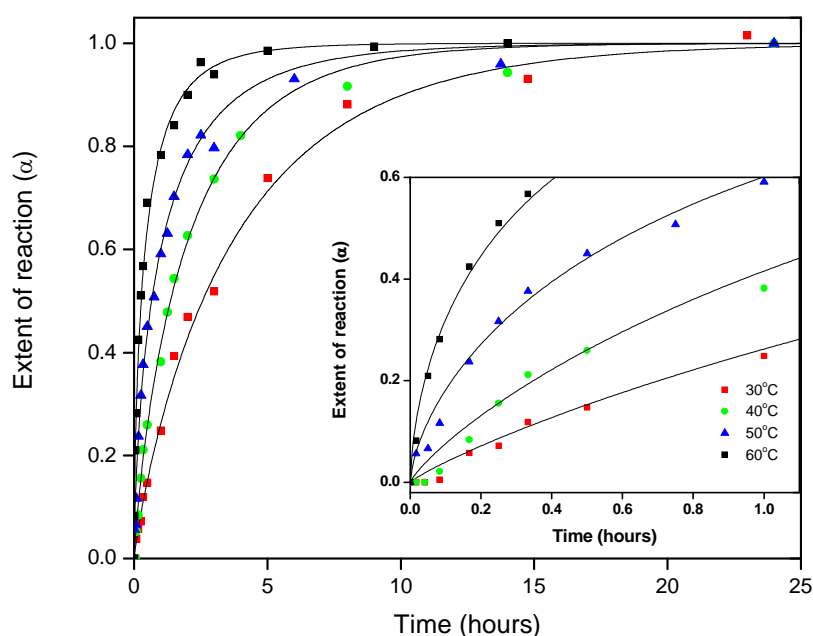
Figure 3.16: Release profile for the exchange reaction of Cl⁻ and ZC-Cn at various temperatures for solid state analysis: 60 ^{o}C (■), 50 ^{o}C (○), 40 ^{o}C (▲), 30 ^{o}C (●). The insert shows low time regime highlighting the induction period for 30 ^{o}C and 40 ^{o}C, note the induction is no longer present at higher temperatures.
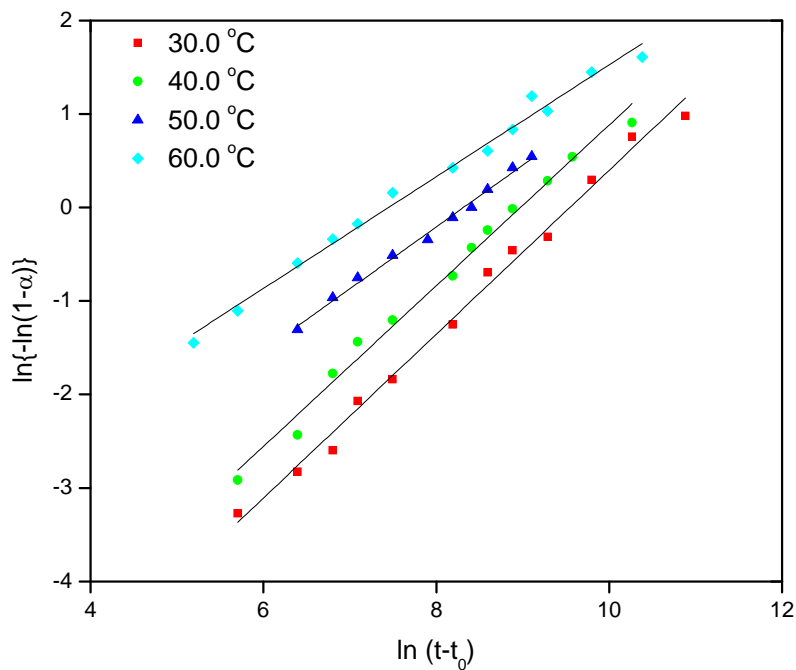
Figure 3.17: Double-logarithmic plots for the exchange reaction of Cl⁻ anion and ZC-Cn at various temperatures for solid state analysis: 60°C (■), 50°C (♦), 40 °C (▲), 30°C (●).

The Avrami –Erofe'ev model was also applied to the solution data obtained from UV-Vis spectroscopy. The release profiles are shown in Figure 3.18 together with the corresponding double-logarithmic plots. The Avrami exponents obtained ranged from 0.4 to 0.8; with a similar temperature dependent variation as observed in the solid phase data. The kinetic parameters obtained from double-logarithmic analysis are presented in Table 3.2. The rate constants obtained for both the solid state transformation and the solution analysis are not significantly different which may indicate that the solid state transformation has the same general kinetics as the release of anions into solution for $0.15 < \alpha < 1.0$. In this case, due to the induction period and the corresponding low initial release of Cn anions into solution, the loss of the host anions and subsequent loss of

coherent diffraction from the host phase occurred at the same rate as the gain in coherent

diffraction from the product phase.

Table 3.2: **A summary of kinetic parameters obtained at different temperatures for the reaction of ZC-Cn with Cl⁻.**

Temperature/ °C	Solid state		solution phase	
	n	$k \ s^{-1}(*10^{-4})$	n	$k \ s^{-1}(*10^{-4})$
60.0	0.61 ± 0.02	6 ± 1	0.41 ± 0.01	4 ± 1
50.0	0.66 ± 0.02	2.4 ± 0.6	0.60 ± 0.02	2.9 ± 0.7
40.0	0.88 ± 0.01	1.3 ± 0.4	0.71 ± 0.02	1.7 ± 0.4
30.0	0.87 ± 0.01	0.7 ± 0.2	0.75 ± 0.02	0.7 ± 0.2

The effective activation energy for the release of Cn was obtained by using both

model fitting methods and model free methods. The Arrhenius plots for the Avrami

model data are shown in Appendix C. For solid state transformation, the Avrami model

led to activation energy of 58 ± 4 kJ /mol while the corresponding E_a for monitoring the

anion release into solution was 45 ± 7 kJ /mol. These values obtained from both solid

state and solution analysis are comparable; this is to be expected since the rate constants

are not significantly different therefore the temperature dependence is not expected to be

different.
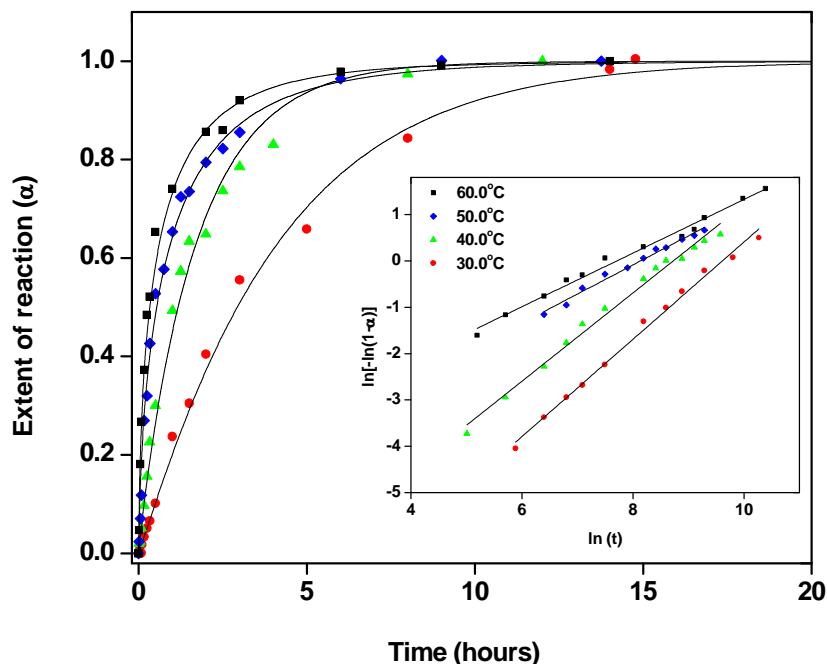
Figure 3.18: Extent of reaction as a function of time for the exchange reaction of Cl⁻ anion and ZC-Cn at various temperatures for solution analysis: 60 °C (■), 50 °C (♦), 40 °C (▲), 30 °C (●), data has been fitted to Avrami –Erofe'ev equation. Insert shows corresponding double-logarithmic plots

The isoconversional treatment of the solid state data shows a linear variation of E_a as a function of extent of reaction (Figure 3.19 A). The E_a start at a value of 102 kJ mol⁻¹ at an extent of reaction of 0.05 and drops linearly to 45 kJ mol⁻¹ at an extent of reaction of 0.8. There is also variation in the E_a with extent of reaction for solution data (Figure 3.19 B), the E_a does not change significantly from extent of reaction of 0.05 up to 0.15 (83-80 kJ mol⁻¹) and then decreases linearly to 41 kJ mol⁻¹ at $\alpha = 0.8$. The variation of E_a as a function of extent of reaction is an indication that the reaction does not proceed via a single mechanism and the decrease in effective E_a may indicate that there is a decreasing

contribution from an initial mechanistic step (or set of steps) with higher E_a. The obtained

activation energy therefore cannot be assigned to a single process or interpreted in terms

of the transition state theory.[124] There is a significant difference between solid state

analysis and solution analysis at low extent of reaction ($0.05<\alpha<0.15$), the E_a for solution

analysis does not significantly change while the variation in effective activation energy

for the solid state reaction is more pronounced. The solution phase analysis showed

almost constant E_a where there is release of Cn from the materials without corresponding

growth of the chloride phase. During this period, the rate of release is low an indication

that this is a high energy transformation. The high energy transformation could be the

chemisorption / desorption of Cl^- and Cn ions on the edges of the interlayer space of the

lamellar compound. After the chemisorption process, the exchange of interlayer Cn ions

results in increased rates of exchange and increased accumulation of released host anions

and subsequent decay and growth of the host and guest anion phases respectively. In the

ZC-Cn structure, the layers are positively charged with the charge being generated when

a quarter of the octahedral sites in the copper hydroxide layers are vacant and Zn^{2+} ions

occupy the tetrahedral sites on either side of the vacant octahedral site, as in Zn,Ni-

Ac.[24;28] Therefore, there is electrostatic interaction between the layers and the interlayer

anions. It has been observed in anion exchange in LDHs that the exchange and complete

replacement of host anions with guest anion within the layers increase the rate of anion-

exchange in the neighboring layers.[171] This has also been observed in intercalation

reactions in TiS_2 where the intercalation of one layer results in the weakening of the

neighboring layer reducing the E_a for intercalation.[181] If the reaction is limited by anion

exchange within the layers then lowering of E_a of exchange in the neighboring layers may result in the gradual lowering of E_a values for the reaction as the exchange proceeds. The gradual lowering of the E_a values is because the exchange reaction occurs from layer to layer as discussed before. This may explain the trend observed in both the solution analysis and solid state analysis. Transition from a chemical reaction controlled process to a diffusion controlled process cannot be ruled out since the E_a values obtained at high extent of reaction are in the range of diffusion controlled reactions. Further work is required to characterize the structure and morphology of exchange products especially during the induction period to ascertain if there are chemical transformations occurring during this period. The E_a values obtained from model-fitting analyses lie within the range of values obtained using isoconversional method which indicates that there is some correlation between the model-fitting methods and the isoconversional method. However, for this reaction, a fit to a single model is not appropriate.
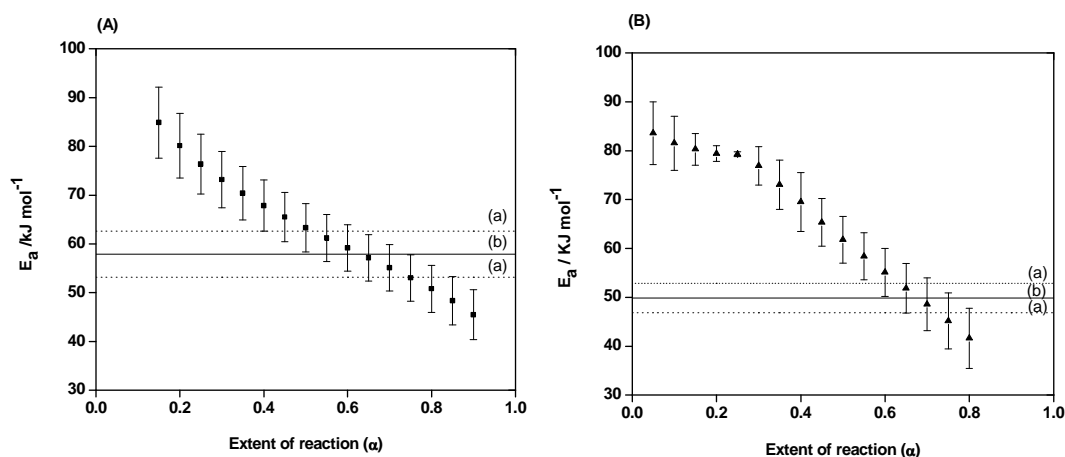
Figure 3.19: Plot of the variation of activation energy with the extent of reaction (α) for (A) solid state analysis and (B) Solution analysis. The solid line (a) represents the Arrhenius determined activation energy and broken lines (b) represent the associated errors.

3.4   Effect of Guest Anions on Anion Exchange Kinetics

The effect of chain length of n-alkyl carboxylate ion on the exchange of C-*o*-HCn was investigated by exposing C-*o*-HCn to solutions containing different n-alkyl carboxylates. The carboxylates tested were formate, ethanoate, propionate, butyrate, pentanoate, hexanoate, and octanoate. From the anions used, only formate, pentanoate, hexanoate and octanoate managed to exchange, the rest were not successful. Fugita and Awagi also failed to exchange n=2-4 carboxylates and they concluded that there was decomposition of the guest anions.[88] The anions which managed to exchange, except for formate, followed the dissolution-reprecipitation mechanism as evidenced by the change in color of the solution to a bluish-green color; there was also a lot of scatter in the data making it difficult to perform kinetic analysis.

Kinetic analyses on the effect of guest anions were performed using bromide and formate anions, in addition to chloride (section 3.3.2.1). The extent of reaction obtained from solution analysis was used to construct release profiles which were fitted to the Avrami –Erofe'ev nucleation-growth model (equation 1.4). The release using chloride anions has been discussed in section 3.3.2.1. The release profiles obtained using bromide and formate anions at 40 ^{o}C were described well by the Avrami –Erofe'ev model as shown in Figure 3.20, where the profiles obtained using formate anions (open circles) and bromide anions (solid squares) are presented. The insert shows the corresponding double-logarithmic plots which are linear over the α range of 0.15 – 1.0. The plots are almost parallel indicating that the reactions occur via the same mechanism for both anions.
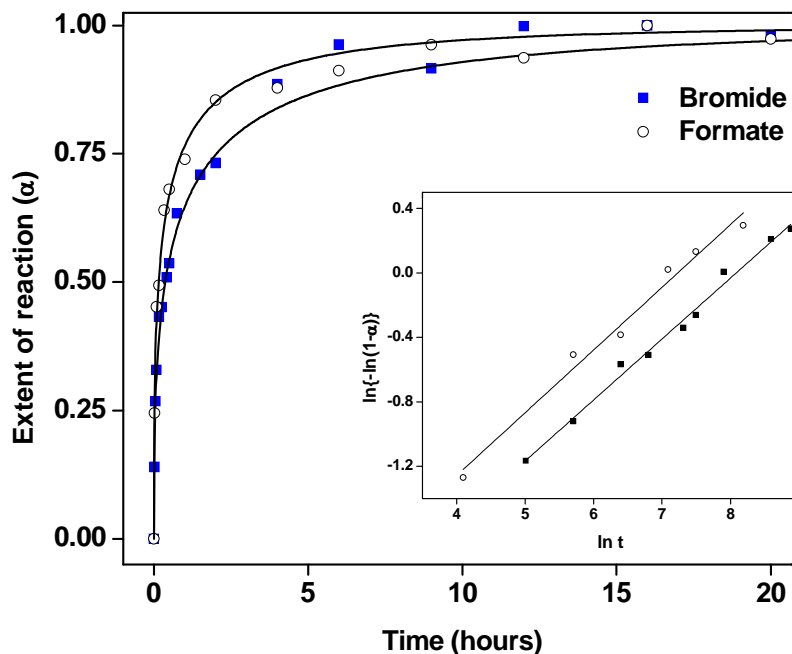
Figure 3.20: Extent of reaction as function of time for the release of *o*-HCn from C-o-HCn following the exposure to formate and bromide anions. The insert shows the corresponding double-logarithmic plots.

The summary of kinetic data is shown in table 3.3. The inorganic anions showed

variation in rate constants which is correlated with their ionic radii, consistent with the

observation of Fogg and O`Hare for the intercalation of lithium salts into Gibbsite.[104] The

value of *n*, which is less than 0.5 for all the anion, is consistent with diffusion controlled

reactions with the rate depending on the transport of the guest anion to the host lattice.

The rate of diffusion of smaller anions is faster than large ones making the exchange

reaction faster as indicated in table 3.3. The organic anion, which has the highest rate,

does not follow this order of size. The differences in charge density which affect the

hydration of the ions and therefore their mobility might be the reason for the observed

differences. Determination of activation energies might give an indication of the factors

making the formate behave unlike the others.

Table 3.3: Summary of the Kinetic Parameters obtained for the exposure of C-o-HCn with various anions

Exchange Anions	n	k (s^{-1})	size (Å)
Cl$^-$	0.39 ± 0.06	(4.3 ± 0.7) x 10^{-4}	1.67[a]
Br$^-$	0.38 ± 0.01	(3.1 ± 0.9) x 10^{-4}	1.82[a]
HCOO$^-$	0.40 ± 0.02	(7.2 ± 1.7) x 10^{-4}	1.98[b]

[a] Thermochemical radii obtained from ref.[104] size of formate was calculated as described in section 2.1.6

PXRD analysis of the solid obtained during the exchange with formate and

bromide at 40 °C are shown in Figures 3.21 A and B respectively. Upon reacting C-*o*-

HCn with sodium formate, a new set of peaks appear, indicated by closed diamonds. The

layered structure of the LHS is maintained during the exchange, which is not complete as

indicated by 00*l* reflections of the precursor anion which are still present. Also the 00*l*

reflections of the guest anion up to 3rd order in the *c* direction can be observed at 2θ =

13.30°, 26.74° and 40.65° which correspond to an average d-spacing of 6.67 ± 0.005 Å.

The appearance of new set of peaks at higher 2θ values is consistent with a smaller anion,

formate with a chain length of 1.98 Å, replacing a much larger anion, *o*-HCn with a chain

length of 8.5 Å. Figure 3.21A also shows that the extent of exchange is much less than

that achieved in Cl$^-$ exchange, section 3.3.2.1 (≈40% for formate exchange as compared

to ≈81% for chloride exchange). This is confirmed by UV-vis analysis data shown in

Figure 3.22 in which the release profiles are plotted in terms of concentration. In this

case, the rate of achieving equilibrium is greater for formate exchange, as indicated by

the higher rate constant, but the equilibrium constant is lower than that of Cl⁻ exchange.
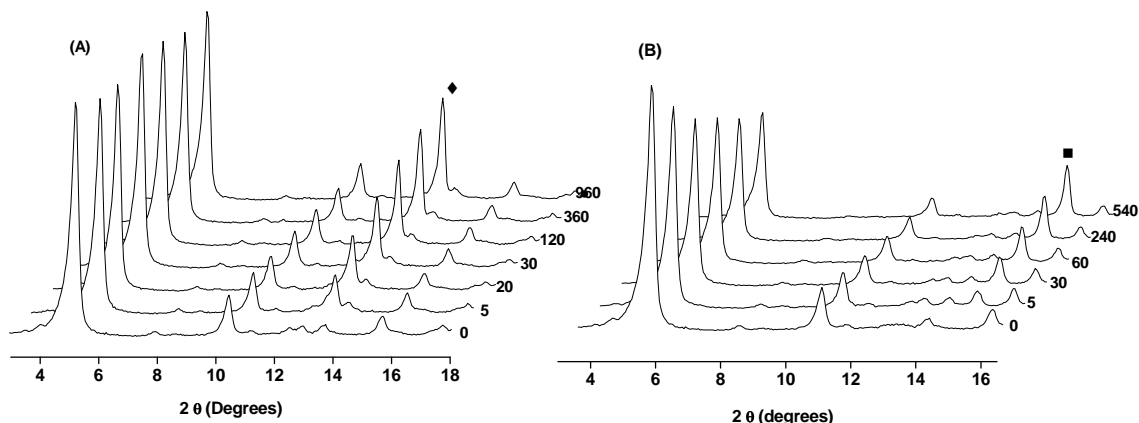
Figure 3.21: PXRD profile for solid sample collected at different times (minutes) for the formate exchange (A) and bromide exchange at 40°C. The formate phase is represented by closed diamonds and the bromide phase is by closed squares.

Just as in the case of formate and chloride exchange, the layered structure was preserved

in Br⁻ exchange. New sets of peaks were observed at higher 2θ values indicating the

contraction of the layers as a smaller anion replaced a large one. The exchange was not

complete as the 00l reflections of the precursor anions are still present. The 00l

reflections of the bromide phase are observed at $2 \theta = 14.59°$ and $29.44°$ corresponding to

an average d-spacing of 6.06 ± 0.00 Å. The bromide phase obtained here is in close

agreement with the phase reported in literature with a d-spacing of 6.056 Å.[5] The extent

of reaction in the Br⁻ exchange is much lower than that in the Cl⁻ exchange ($\approx$54%). This

can be explained by the differences in size affecting the affinity of two ions for the metal

hydroxide layers. Due to the smaller size and the higher charge density of the chloride

anion, the metal hydroxide layers have a greater attraction for the chloride anion as compared to Br⁻ anion. Calculations of thermodynamic parameters for the exchange reactions might shed more light into the behavior of the ions.
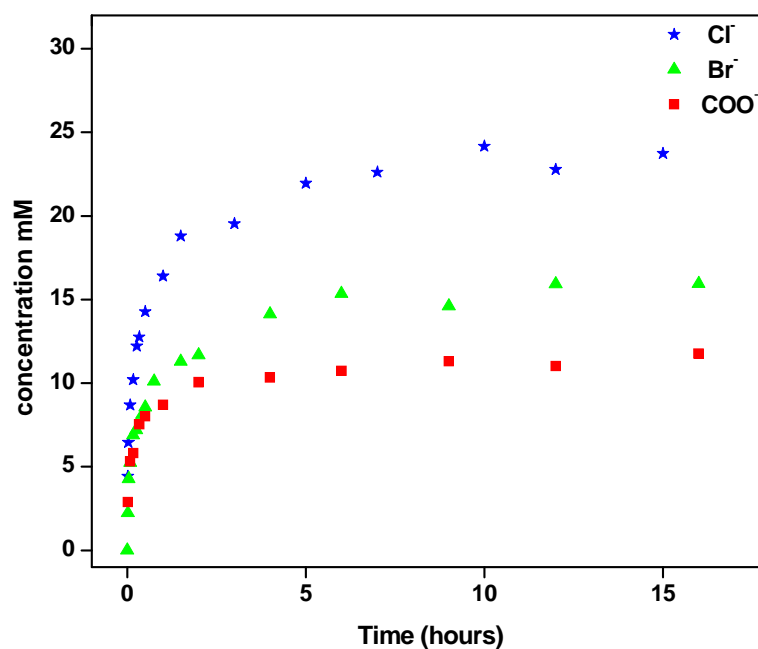
Figure 3.22: Plot of concentration as a function of time (hours) for the release of *o*-HCn using Cl⁻ (asterisk); formate (squares) and bromide (open triangles)

3.5   Conclusions

Isoconversional analysis has been successfully applied, for the first time, to anion release kinetics in layered materials. The effective activation energies obtained from isoconversional analysis indicated that, for the C-o-HCn system, there is no variation in the mechanism of the reaction; the E_a values remained constant with respect to extent of reaction, within the limits of experimental uncertainty. The effective activation energies for replacement of o-HCn by chloride that were extracted from the isoconversional analysis ranged from 87-96 kJ mol^{-1} in solid state analysis and 78-85 kJ mol^{-1} for solution analysis and were found to be in agreement with those obtained from a global fit to the data using the Avrami-Erofe'ev model. In the second model system presented here, ZC-Cn reaction with chloride, there was a clear variation of the E_a with respect to extent of reaction indicating that there where changes in the reaction mechanism as the reaction progressed. The Avrami-Erofe'ev model, or any other single mechanism, is therefore inadequate for modeling the reaction kinetics, particularly for determining the effect of temperature over the entire extent of reaction. Use of isothermal, isoconversional approaches is a convenient method for testing the applicability of the Avrami (or any other model-based) approach.

Chapter 4 :   Controlled Release in Hydroxy Double Salts: Effect of Host Anion Structure.

4.1   Introduction

Anion exchange ability of nanodimensional layered metal hydroxides (LDHs, HDSs and LHSs), potential for sustained release, and their biocompatibility have made them attractive in the uptake, storage and controlled release delivery of bioactive materials such as drugs and pesticides.[60-65] Water contamination due to transport losses in the uses of pesticides can be minimized by using controlled release formulations in which the pesticide is incorporated into a matrix or carrier before application. The pesticides which are encapsulated in the carriers are gradually released over a long period of time thereby limiting the amount of chemicals immediately available for unwanted transport losses. Cardoso *et al.* showed that incorporation of 2,4-dichlorophenoxyacetic acid (2,4-D), 4-chloro-2-methylphenoxyacetic acid, and picloram resulted in sustained release of the herbicides over a period of up to 8 days and also resulted in reduction of leaching from soil.[182] Similar results were also obtained by Hussein *et al*. for the release of 4-chlorophenoxyacetate and 2,4-D from ZnAl-LDH.[121;183] Yang *et al.* observed a sustained release of the plant growth hormone indole-3-acetic acid from ZnAl-LDH and zinc LHS with the release from the LHS being slower.[135]

Encapsulating drugs in nanodimensional layered materials can improve the stability of unstable drug molecules as reported by Panda *et al.* who observed

stabilization of statin drugs by intercalation into MgAl-LDH.[63] The drugs were released over a period of up to 60 hours. Other workers have also observed similar sustained release of other drugs from layered materials, Gu *et al.* [62] for the release of heparin, Li *et al.* for the release of prednisone,[184] and others which include captopril and pamoate among others.[185;186] Khan *et al.* have done systematic investigations on the effects of metal hydroxide layer composition and nature of the intercalated anions in controlling their release into solution.[67]

The rate of release of stored drugs and pesticides has been shown to be affected by the intralayer metal composition of the host metal hydroxide layers and the size of the intercalated drugs and pesticides.[67;135;182] In addition to the effect of the metal hydroxide layer metal ion composition and size of intercalated drugs, the structure of the intercalated drugs is expected to significantly affect their rates of release. In studies involving intercalation reactions, it has been shown that LDHs and HDSs exhibit selectivity when intercalating geometric, and stereoisomers.[64;69-74] This selectivity may be due to differences in the interaction of the isomers with the metal hydroxide layers due to differences in properties such as dipole moments.[72] This difference in affinity of the metal hydroxide layers to isomers may also affect the retention of the molecules within the layers and hence the rate and magnitude of release of the intercalated isomers.

Although a lot of studies have been carried out on the applications of LDHs and HDSs in controlled release of pharmaceuticals,[60;61;63;65;121;135] and while different drugs have been shown to have different release rates,[62;67;137] the systematic study on the effect of anion structure on the rate and extent of release is yet to be investigated. In this study,

isomers of hydroxycinnamate will be used as model compounds to study the effect of structure/isomerism on the controlled release of anions from HDSs. It is anticipated that this study will enable fine tuning of rates of release by altering the structure of drugs and pesticides.

4.2   Experimental

4.2.1   Materials

Copper acetate monohydrate [Cu $(C_2H_3O_2)_2 \cdot H_2O$] (98.0 %) was obtained from Alfer Aesar, *o*-hydroxycinnamic acid [*o*-$(OH)C_6H_4CHCHCO_2H$] (98%), *m*-hydroxycinnamic acid [*m*-$(OH)C_6H_4CHCHCO_2H$] (98%), and *p*-hydroxycinnamic acid [*p*-$(OH)C_6H_4CHCHCO_2H$] (98%) (All isomers were predominantly trans) were obtained from Aldrich Chemical Co. Sodium chloride (100%) and zinc oxide (100%) were obtained from J. T. Baker; Sodium hydroxide (pellets, 98%) was obtained from EMD Chemicals.

4.2.2   Synthesis of nanohybrids

The nanohybrids containing hydroxycinnamate isomers were prepared from ZC-Ac by anion exchange. ZC-*o*-HCn was prepared by mixing 20.0g of ZC-Ac with 1000 cm^3 of a 0.1 M *o*-hydroxycinnamate (*o*-HCn) solution at room temperature for 24 hours with frequent stirring; the exchange reaction was carried out twice using the same conditions. ZC-*m*-HCn was prepared by reacting ZC-Ac with 0.5 M *m*-hydroxycinnamate (*m*-HCn) solution at 40^oC for 24 hours with frequent stirring, the exchange was carried out three times using the same condition each time. High concentration and more exchange time was necessary to ensure complete exchange. 1.0 M *p*-HCn was used in the preparation of ZC-*p*-HCn with the exchange reaction being done once at 40^oC, the higher concentration was necessary to obtain a single *p*-HCn phase.

4.2.3 Characterization

Fourier transform infrared (FTIR) spectra of the nanohybrids were obtained on a Perkin Elmer Spectrum 100 FT-IR spectrometer operated at a 2 cm^{-1} resolution in the 4000 - 650 cm^{-1} spectral range. The obtained spectra were an average of 16 scans. The FTIR spectra were recorded using a single reflection ATR accessory with a ZnSe prism (PIKE MIRacle^{TM}, from PIKE technology).

Powder X-ray diffraction (PXRD) measurements were recorded on a Rigaku Miniflex II diffractometer using Cu Kα (λ =1.54 Å) radiation source at 30kV and 15mA. Powder samples were pressed into the trough of glass sample holders. The patterns were recorded in the 2θ range of 2.0^{o} - 45.0^{o}; data acquisition was performed using a step size of 0.0167^{o} per second. Elemental analysis was carried out by Huffman labs, Colorado, using atomic emission spectroscopy interfaced with inductively coupled plasma (AES-ICP) for metal determination.

4.3   Results and Discussion

4.3.1   Preparation and Characterization of hydroxycinnamate nanohybrids.

Nanohybrids containing isomers of hydroxycinnamate in the interlayer space were prepared from ZC-Ac by anion exchange. The uptake of the isomers and the complete replacement of acetate anions in the interlayer space was confirmed by PXRD and ATR-FTIR. Elemental analysis was used to determine the chemical formulae of the prepared nanohybrids. A summary of elemental analysis and X-ray diffraction data for the nanohybrids is shown in table 4.1. The formulae obtained from elemental analysis (Table 4.1) were used to calculate the total amount of isomers intercalated into the interlayer space and hence the fraction released at any given time. The low amount of water in the gallery (from formulae in Table 4.1) is consistent with TGA results shown in Appendix D. As an example, from TGA results there is 1.6% water loss in the degradation of ZC-*o*-HCn and the formula in Table 4.1 indicates 1.7% water content. From the formulae obtained from elemental analyses, the ratio of copper to zinc in the metal hydroxide layers of ZC-*m*-HCn (2.8) and ZC-*p*-HCn (2.5) is comparable to that of the precursor ZC-Ac (2.8) nanohybrid (section 3.2.3) which may indicate that the exchange reaction was tapotactic, there was no structural changes in the metal hydroxide layers. The ratio in ZC-*o*-HCn nanohybrid (3.5) is higher than in the precursor material which may be an indication that the exchange reaction occurred via the dissolution-recrystallization mechanism. In this case the nature of the cations and the anions determine the ratio of the metal ions in the layers which may have resulted in the higher

copper content, [6;23] XRD analysis shows that there is no identifiable copper hydroxide phase in the material.

Table 4.1. Summary of elemental analysis and XRD data.

Nanohybrid	XRD	Elemental analysis (%): experimental (calculated)			
	d/Å	Zn	Cu	H	C
$ZnCu_{2.8}(OH)_{5.3}(Ac)_{1.7} \cdot 2.6\ H_2O$	9.43	14.72(14.15)	35.84 (34.44)	3.25 (3.39)	9.25 (8.90)
$ZnCu_{3.5}(OH)_{6.8}(o\text{-}HCn)_{2.2} \cdot 0.8\ H_2O$	16.95	8.41 (8.43)	28.69 (28.75)	3.07 (3.07)	30.52 (30.56)
$ZnCu_{2.8}(OH)_{4.8}(m\text{-}HCn)_{2.8} \cdot 0.6H_2O$	20.72	8.35 (8.27)	22.84 (22.61)	3.28 (3.24)	38.4 (38.01)
$ZnCu_{2.5}(OH)_{4.0}(p\text{-}HCn)_{3.0} \cdot 0.3H_2O$	21.03	8.27 (8.30)	20.03 (20.11)	3.32 (3.33)	40.58 (40.74)

The PXRD patterns for ZC-Ac and exchange products are shown in Figure 4.1. All the materials show at least three equally spaced Bragg reflections at low 2θ values indicating that the materials are layered and possess high range ordering. These basal reflections were used to calculate the d spacing using the Bragg equation,[148] the results are summarized in table 4.1. The precursor HDS, ZC-Ac, has been characterized in chapter 3. In all the exchange reactions, the transformation to the exchange product occurred as a single step; there is no evidence for any crystalline intermediates. As table 4.1 reveal, there is an increase in the basal spacing as the acetate anion is replaced by *n*-HCn ions in the interlayer space. The increase in the basal space is consistent with a smaller anion (acetate ion chain length = 1.65Å) being replaced by larger *n*-HCn anions (chain lengths = 8.63 Å for *o*-HCn; 8.64 Å for *m*-HCn and 9.11 Å for *p*-HCn). Considering the chain lengths of the meta and para isomers and the size of the gallery height (about 16 Å if the layer thickness is approximated to be 5 Å as in copper hydroxide)[88] and taking into account the associated van der Waals radii, the anions are likely to be arranged in a slightly tilted bilayer orientation. The interlayer space observed in ZC-*o*-HCn is significantly smaller compared with the other nanohybrids. It was expected that the d-spacings would be comparable considering the similarities in the sizes of the isomers. The smaller d-spacing in ZC-*o*-HCn might be a result of the ortho isomer being in a more tilted orientation as compared to the other isomers. The Bragg reflections due to acetate anions are no longer present in the PXRD traces of the exchange products indicating that the exchange was complete.
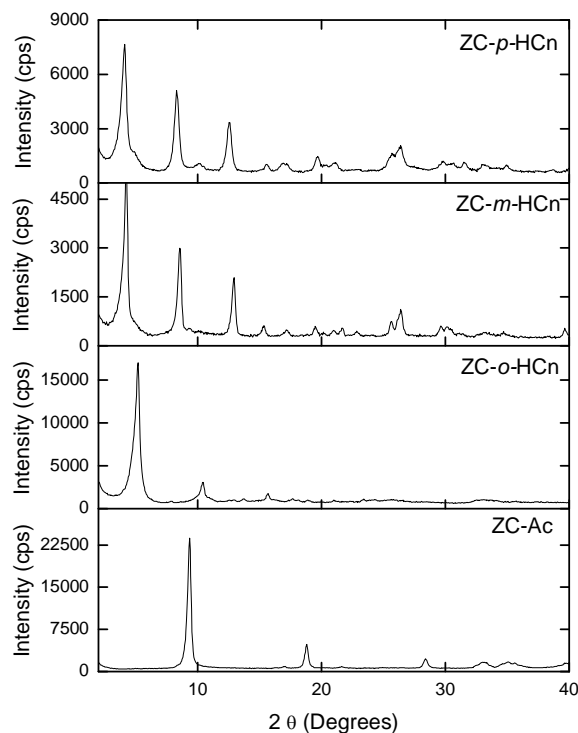
Figure 4.1: PXRD profiles for ZC-Ac and exchange products.

IR spectra presented in Figure 4.2 shows that when acetate ions were replaced by *n*-HCn ions, the peaks due to C=O vibrations of acetate ions in ZC-Ac (υ_{asym} = 1563 cm^{-1} and υ_{sym} =1410 cm^{-1}) where replaced by a series of peaks (1637–1642 cm^{-1}, C=C; 1540–1551cm^{-1}, υ_{asym} C=O and 1413–1428 cm^{-1}, υ_{sym} C=O). The disappearance of vibration peaks from acetate ions is consistent with results inferred from PXRD analysis. The absence of the C=O stretching vibration of the protonated carboxylic groups, which is around 1700cm^{-1}, confirms that the isomers are present in the ionized form. The hydroxyl stretching vibrational modes in the region (3000 cm^{-1}–3600 cm^{-1}) provide information about the level of hydrogen bonding in the interlayer space.[152] The structural properties of

hydroxyl groups within the interlayer space can be correlated to the OH vibrational

modes. Broad absorption bands have been associated with stretching modes of hydrogen

bonded hydroxyl groups.[187] The FTIR profiles of the hydroxyl stretching region of ZC-

Ac and the exchange products are shown in Figure 4.3. ZC-Ac was shown in chapter 3 to

have extensive interlayer hydrogen bonding due to intercalated water molecules. Figure

4.3 shows that when acetate ions were replaced by *m*-HCn ions in ZC-*m*-HCn, the broad

peak centered at 3450 cm^{-1} in ZC-Ac was replaced by 2 sharp peaks, a strong peak at

3513 cm^{-1} and a weak peak at 3574 cm^{-1}. Comparing Figure 4.3 with FTIR spectrum of

ZC-Cn in section 3.3.1 (no OH substitution on the benzene ring) in which 3513 cm^{-1} peak

was absent; The sharp peak at 3574 cm^{-1} can be assigned to layer hydroxyl groups and

the peak at 3513 cm^{-1} to *m*-HCn hydroxyl groups, which are not involved in substantial

hydrogen bonding.[152] ZC-*o*-HCn has a very weak peak around 3600 cm^{-1} and 2 broad

peaks (3489 cm^{-1} and 3131 cm^{-1}). The broadening of peaks and the shift to lower

wavenumbers, as compared to vibrations in ZC-*m*-HCn, is consistent with hydrogen

bonded hydroxyl groups.[158] The low intensity of the sharp band at 3600 cm^{-1} is indicative

of extensive hydrogen bonding between layer OH groups and *o*-HCn hydroxyl groups

resulting in low density of free layer OH groups. In ZC-*p*-HCn, there is a strong sharp

peak at 3574 cm^{-1} which is due to layer OH groups which are not involved in significant

hydrogen bonding and a broad peak at 3497 cm^{-1} due to hydrogen bonded *p*-HCn

hydroxyl groups.
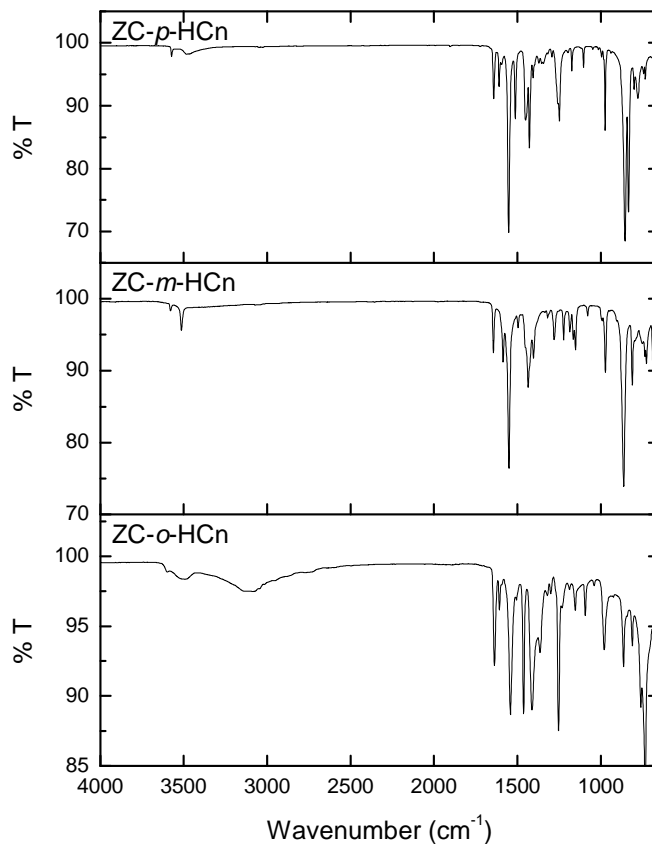
Figure 4.2: FTIR spectra for isomer of hydroxycinnamate intercalates

The presence of strong sharp peaks in ZC-*m*-HCn and ZC-*p*-HCn, which are absent in ZC-*o*-HCn, indicates that there is extensive hydrogen bonding in ZC-*o*-HCn as compared to the other nanohybrids. Since hydrogen bonding is directional, the *m*-HCn anions are not oriented in such a way that the OH groups are able to interact with either the layer OH groups or groups from other anions while the OH groups in *p*-HCn may be involved in intermolecular H-bonding. Since the amount of intercrystalline water in the nanohybrids is low, as indicated from thermogravimetry and elemental analyses, significant hydrogen bonding observed in ZC-*o*-HCn and ZC-*p*-HCn is most likely

between anion and layer hydroxyl groups, and between anion hydroxyl groups respectively. Figure 4.4 shows a schematic representation of the groups involved in hydrogen bonding in ZC-*o*-HCn (Figure 4.4 a) and ZC-*p*-HCn (Figure 4.4 b). In *o*-HCn the OH group may be in an orientation such that the hydroxyl groups are close to the layers enabling formation of hydrogen bonds.[72] The interaction between *o*-HCn and layer hydroxyl groups may have resulted in the *o*-HCn anion being tilted closer to the layers, explaining the smaller gallery height (as compared to that in ZC-*m*-HCn and ZC-*p*-HCn) observed from PXRD analysis.
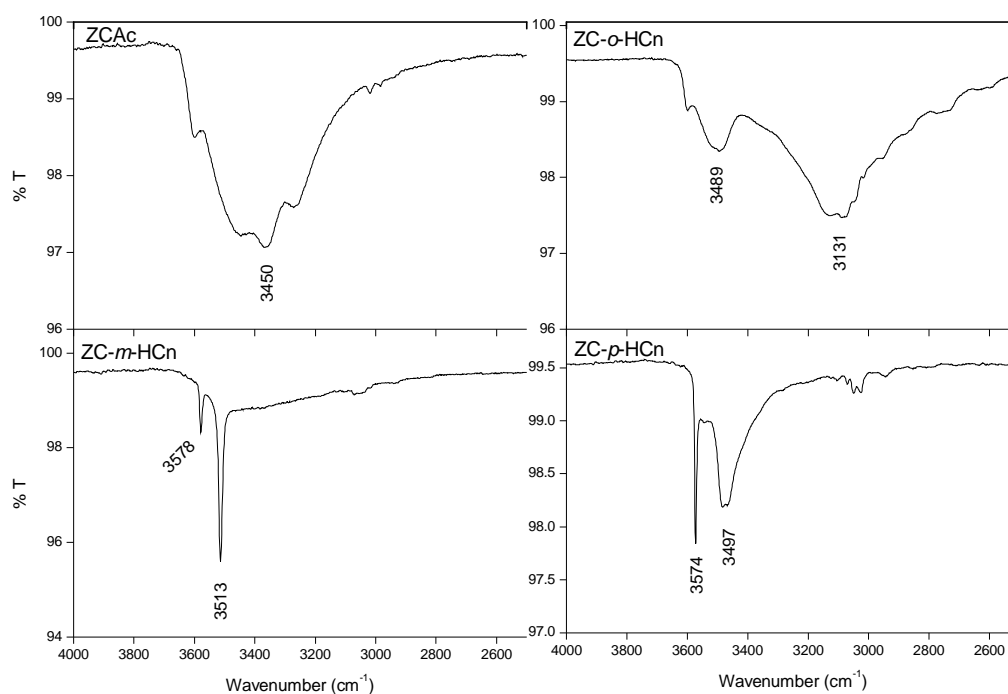
Figure 4.3: FTIR spectra for ZC-Ac and exchange products showing the hydroxyl stretching region.
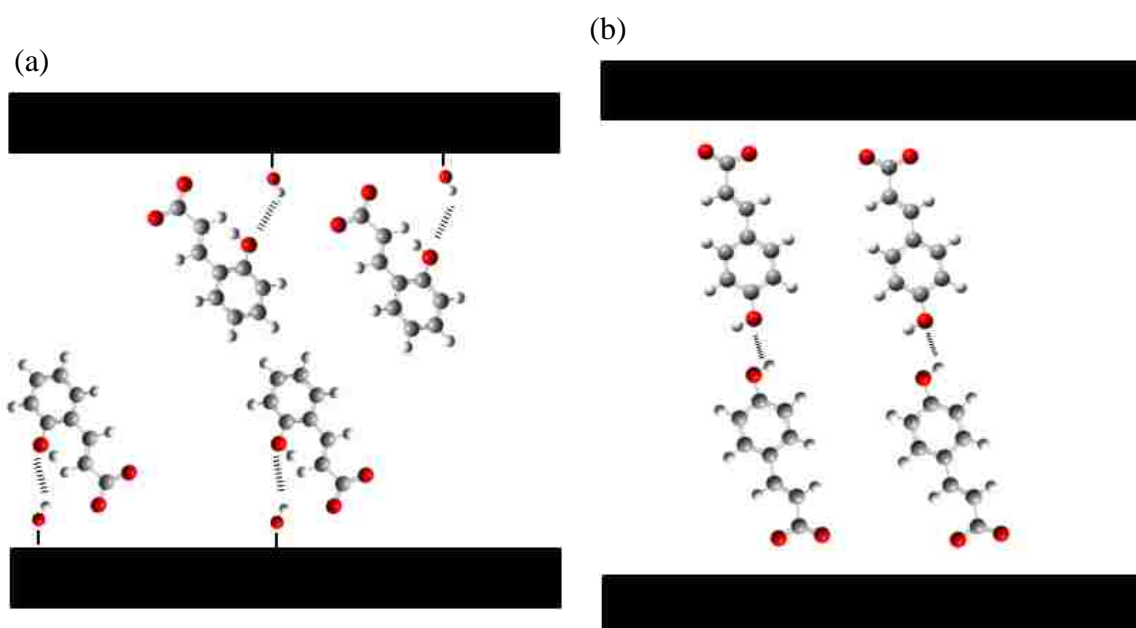
Figure 4.4: Schematic representation of the groups involved in hydrogen bonding in (a) ZC-*o*-HCn and (b) ZC-*p*-HCn. Oxygen atom is represented in red and hydrogen as the small grey ball.

Kinetic Analysis

The release of n-HCn from nanohybrids was achieved by ion exchange using Cl⁻ ions as exchange anions. After specified times, supernatants were collected and analyzed for released anions and the residues were analyzed for solid state transformations using PXRD. Analysis of the solid samples recovered from the reaction mixtures after each contact time indicated that the same chloride phase was obtained for all the nanohybrids. A representative PXRD profile for the zinc copper chloride (ZC-Cl) obtained from exchange reactions is shown in Figure 4.5, the chloride phase has a d-spacing of 5.74 ± 0.01 Å which is in close agreement with literature value of 5.73 Å[188] and has been indexed as kapellasite $Cu_3Zn(OH)_6Cl_2$ (PDF # 56-71).[154;188] The decrease of the interlayer space as the isomers are released is consistent with large anions being replaced by smaller ions.
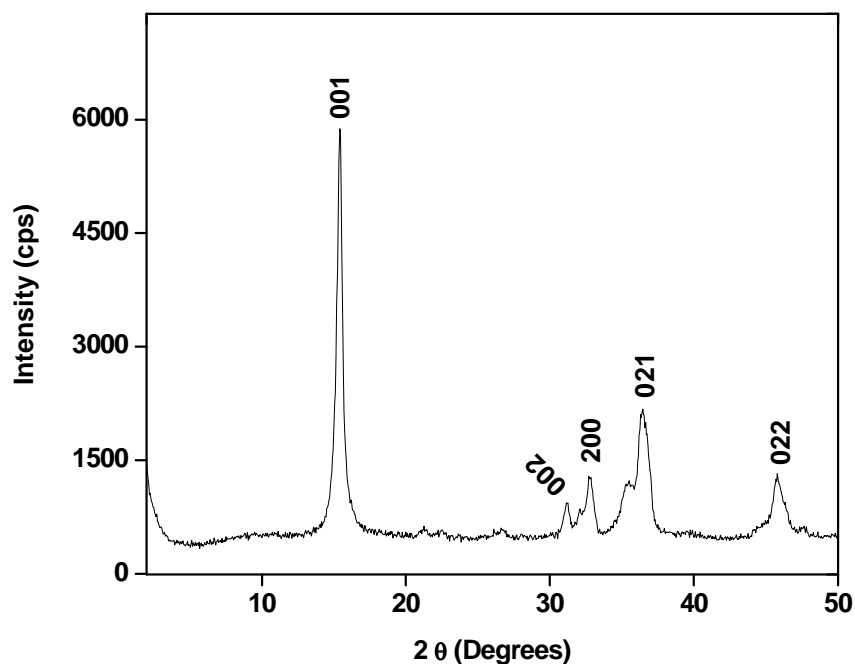
Figure 4.5: PXRD profile of a representative ZC-Cl (kapellasite) obtained from exchange reactions (ZC-*o*-HCn/ Cl- reaction), Miller *hkl* indices for selected Cl⁻reflections are given, PDF # 56-71.

The concentrations of released anions were evaluated using UV-Vis spectroscopy. The fractions of released isomers (*n*-HCn) as a function of time (release profiles) at 40°C are shown in Figures 4.6 (a)-(c) for *m*-HCn, *o*-HCn and *p*-HCn respectively. The release profiles at other temperatures are presented in Appendix E. Although the chemical structures of the isomers are similar and the release medium is the same, the release profiles and hence release properties are significantly different (Figure 4.6). The equilibrium amounts released at 40°C shown in Table 4.2, together with calculated dipole moments and atomic charges, were significantly different. ZC-*o*-HCn released 90% of the intercalated *o*-HCn ions after about 5 hours while ZC-*m*-HCn released about 40% at equilibrium (3 hours) and ZC-*p*-HCn released about 22% after 3 hours. UV-vis analysis

resulted in a 10% underestimation of the amount of o-HCn released at equilibrium, with XRD indicating complete exchange but UV-Vis analysis indicating 90% extent of reaction. This may be a result of differences in the sensitivities of the different methods used; this may also be true for other isomers. The extent of reaction for the release of m-HCn and p-HCn showed temperature dependence increasing with temperature (Appendix E).

Table 4.2: Summary of dipole moments and release data.

Anion	Equilibrium isomer released at 40°C (%)	Dipole moment	Calculated Charges		
			Carbon	Oxygen 1	Oxygen 2
o-HCn	90	13.7 D	+0.036	-0.460	-0.455
m-HCn	40	14.9 D	-0.003	-0.431	-0.457
p-HCn	22	16.7 D	-0.005	-0.461	-0.434
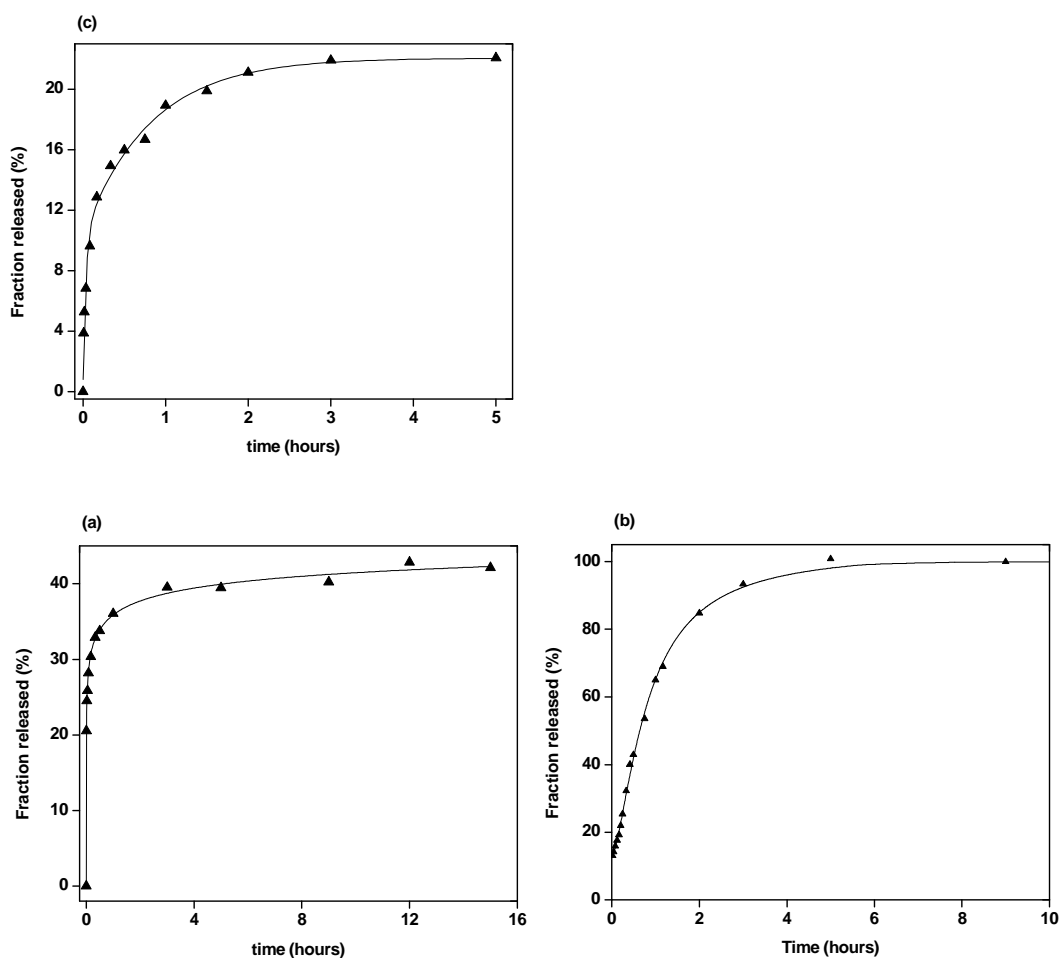
Figure 4.6: Release profiles for (a) ZC-*m*-HCn, (b) ZC-*o*-HCn and (c) ZC-*p*-HCn at 40°C.

The differences in the extent of reaction may indicate differences in the affinity of the HDS for the isomers and/or differences in the thermodynamic equilibrium constants of the systems. The extent of anion exchange depends on several factors which include the solvation enthalpy of the isomers, the binding enthalpy (between the metal hydroxide layers and the isomers), and the inter / intra molecular interactions of the isomers within the layers.[71;72;179] The major contributing factor is expected to be the electrostatic

interaction between the positively charged metal hydroxide layers and the negatively charged anions, with the carboxylate group of the isomers being in close contact with the layers. Since the isomers have the same charge and comparable size, differences in dipole moments could have more influence on the thermodynamics of the release process. Results of dipole moment calculations together with charge density of selected atoms are shown in Table 4.2. The magnitude of dipole moments (an indicator of the charge distribution) have been shown to be correlated with selectivity (affinity) of layered double hydroxides (LDHs) to isomers in intercalation reactions.[71;72;179] The affinity of the metal hydroxide layer is higher for the isomer with the highest dipole moment,[71] therefore this isomer is expected to be retained within the layers more than the other isomers. Although factors which influence the extent of release are expected to be complex due to the processes involved in anion exchange reactions,[75] the results obtained here infer that the magnitude of dipole moments should play a significant role in determining the equilibrium constant and hence anion retention and release. The maximum amount accumulated for anion release follows the following order, o-HCn>m-HCn >p-HCn, which is opposite that of magnitude of dipole moments as shown in Table 4.2. The order of isomer selectivity in intercalation reactions is the reverse of the order of equilibrium amount release observed here, which is expected. Since p-HCn has the highest dipole moments, the metal hydroxide layers are expected to have the greatest affinity for p-HCn as compared to the other isomers,[71] this could explain the order observed here.

From Figure 4.6 it can qualitatively be observed that the release rates of the isomers are significantly different, so are the release profiles. While the profile for o-HCn release is sigmoidal those for meta and para isomer release are deceleratory. Although coulombic interactions might be the major contributor to the overall enthalpy of the exchange reaction and determination of reaction rates, presence of hydrogen bonding could also play a significant role. H-bonding offers additional stability to the anions within the layers affecting their release behavior as observed by Prasanna and Kamath in LDH containing different ratios of nitrate ions.[139] FTIR results (Figure 4.3) indicate different levels of hydrogen bonding in the nanohybrids which affect the stability of the compounds and their release behavior. Hydrogen bonding is directional; therefore specific orientation of the anions in the gallery will result in hydrogen bond formation and improved stability of the nanohybrid.

The release profile for *m*-HCn at 40°C (Figure 4.6 a) shows that there is burst and rapid release in the first 10 minutes followed by a more sustained release afterwards with equilibrium being attained after 3 hours. About 75% of the total amount released at equilibrium was released in the first 20 minutes with the remaining 25% being released in about 2.5 hours. This initial fast release is observed for all the temperatures used here as shown in Appendix E, and has been observed in anion exchange reactions in LDHs[67;189] and in physical mixtures where the anions are adsorbed on the surface of the nanohybrids.[134] The burst release observed here is due to anion exchange as confirmed by PXRD results shown in Figure 4.7. The chloride phase, represented by a square in Figure 4.7, appeared almost instantaneously and was significant after only 30 seconds of ZC-*m*-

HCn being in contact with the chloride solution. This release behavior is consistent with the absence of hydrogen bonding which has been shown to offer additional stability to layered metal hydroxides. Inclusion of water into the interlayer space has been shown to stabilize the compounds by hydrating the anions and solvating the layers.[9] The exclusion of water and the absence of hydrogen bonds make the compound thermodynamically unstable with the anions preferring bulk solution (in which there is stabilization by solvation with water molecules) to gallery space resulting in the burst release observed here. The incorporation of chloride ions during the exchange process results in significant inclusion of water molecules in the gallery resulting in significant hydrogen bonding within the layers. The presence of water in the interlayer and possible H-bonding and solvation of the anion coupled with other interactions discussed before will then determine the extent of release of the anion.
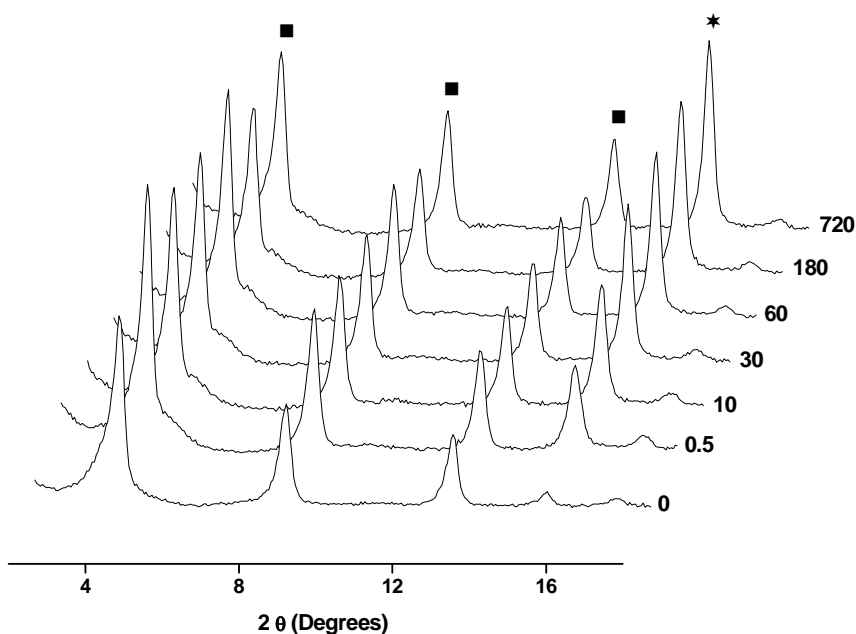
Figure 4.7: PXRD profile for solid sample collected at different times (minutes) for the reaction of ZC-*m*-HCn with Cl⁻ at 40°C, the Cl⁻ phase is represented by an asterisk and *m*-HCn phase by closed square

Figure 4.6 b shows that there are 3 distinct regions in the release profile of *o*-HCn, a slow release during the first stage, a rapid release during the second stage and a slow release in the final stage. Compared to the burst release observed in ZC-*m*-HCn, there was only 8.5 % *o*-HCn released from ZC-*o*-HCn in the first 12 minutes. The initial slow release in ZC-*o*-HCn may be due to the existence of extensive hydrogen bonding as indicated by FTIR data in Figure 4.3. This first stage of release has a strong temperature dependence being more pronounced at low temperature and almost absent at higher temperatures (Appendix E). The slow release is also confirmed by PXRD data in Figure 4.8; the chloride phase starts to appear after 5 minutes of contact time and the increase in intensity of the phase is initially slow. The delayed appearance of the guest anion phase has been observed in other intercalation reactions,[123] and maybe due to the Cl⁻ phase

having low intensity which could not be detected by the diffractometer used here or the chloride phase is initially amorphous and hence could not be detected. The slow release of o-HCn ions without corresponding growth of guest phase maybe due to exchange of anions present on the surface and edges of interlayer space of the material. The release of surface adsorbed protonated o-HCn molecules has been ruled out since trace amounts of o-HCn were released when the material was placed in DI water at 40 ^{o}C for 48 hours without any sodium chloride being present, much less than the amount released during the induction period. The growth of the chloride phase and the subsequent disappearance of the o-HCn phase indicate that release of o-HCn anions from the layers is by anion exchange. Figure 4.8 indicates complete release of o-HCn from the nanohybrids and that the layered structure is maintained during the exchange reaction. There is strong temperature dependence in the release reaction as shown in Appendix E, with 90% of o-HCn being released in 6.5 hours at 30°C, 2.5 hours at 40°C, 53 minutes at 50°C and 31 minutes at 60°C.
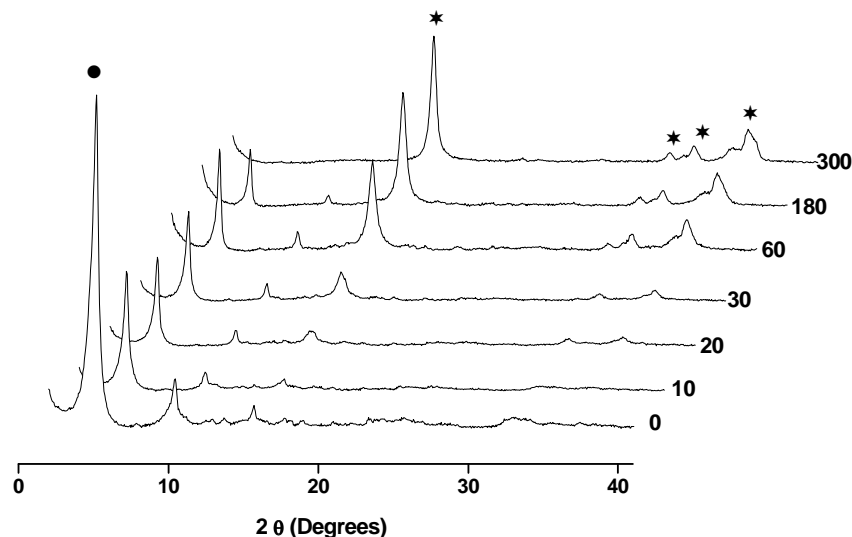
Figure 4.8: **PXRD profile for solid samples collected at different times (min) for the reaction of ZC-*o*-HCn with Cl⁻ at 40°C, selected Cl⁻ phase peaks are represented by asterisks and the *001* phase of *o*-HCn phase is represented by closed circles**

The release of *p*-HCn is gradual and biphasic with an initial fast release during the first 10 minutes in which about 50% of the maximum released (10% of the total amount intercalated) was released, followed by a slower release in which the other 50% was released over a period of about 3 hours. Gu *et al.* observed similar biphasic patterns in the release of the anticoagulant heparin from LDH,[62] whilst Hussein *et al.* observed the same pattern in the release of the herbicide 2,4-dichlorophenoxyacetate from LDH.[121] There is strong temperature dependence in the extent of reaction as shown in Appendix E, the equilibrium amount released significantly increased as the temperature was increased. The fraction released at equilibrium increased from 20% at 30°C to 33% at 60°C, this temperature dependence has been observed by other workers.[67] The incomplete exchange observed in the UV-Vis data is confirmed by PXRD results for solid samples obtained

after release. As shown in Figure 4.9 for the release at 40°C; in addition to reflections from chloride ion, the Bragg reflections from *p*-HCn anions are still present.
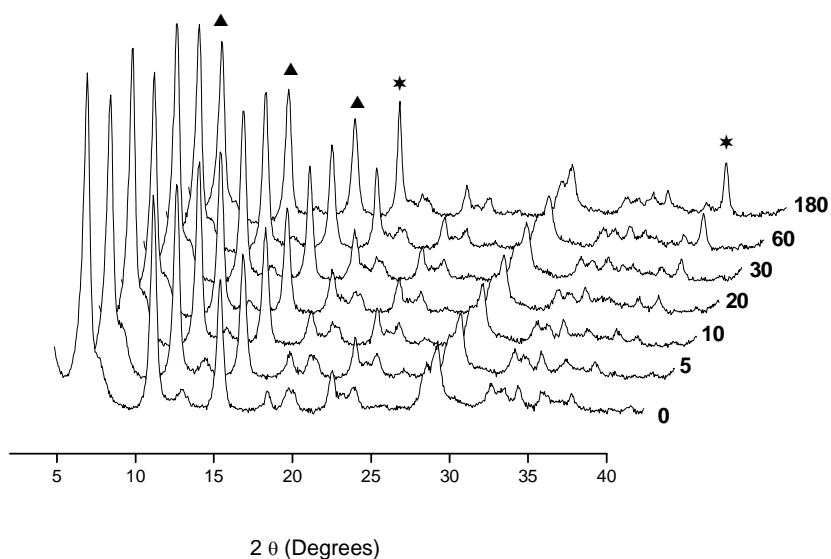
Figure 4.9: PXRD profile for solid sample collected at different times for the reaction of ZC-*p*-HCn with Cl⁻ at 40°C, the *001*Cl⁻phase is represented by an asterisk and the *o*-HCn phase represented by closed circles

We have shown in Chapter 3 that isoconversional methods can be extended to anion exchange reactions in layered metal hydroxide as a strategy to identify when using model based approaches are appropriate. As such the first approach is to use the isoconversional method to evaluate if the reactions occur via a single mechanism before we apply model based approaches. The integral isoconversional method, equation 1.7, was again applied to the kinetic data obtained here. The isoconversional analysis data for all the nanohybrids is shown in Figure 4.10 in which the E_a values remains constant, within experimental error, over the entire conversion range for ZC-*m*-HCn and ZC-*p*-HCn.
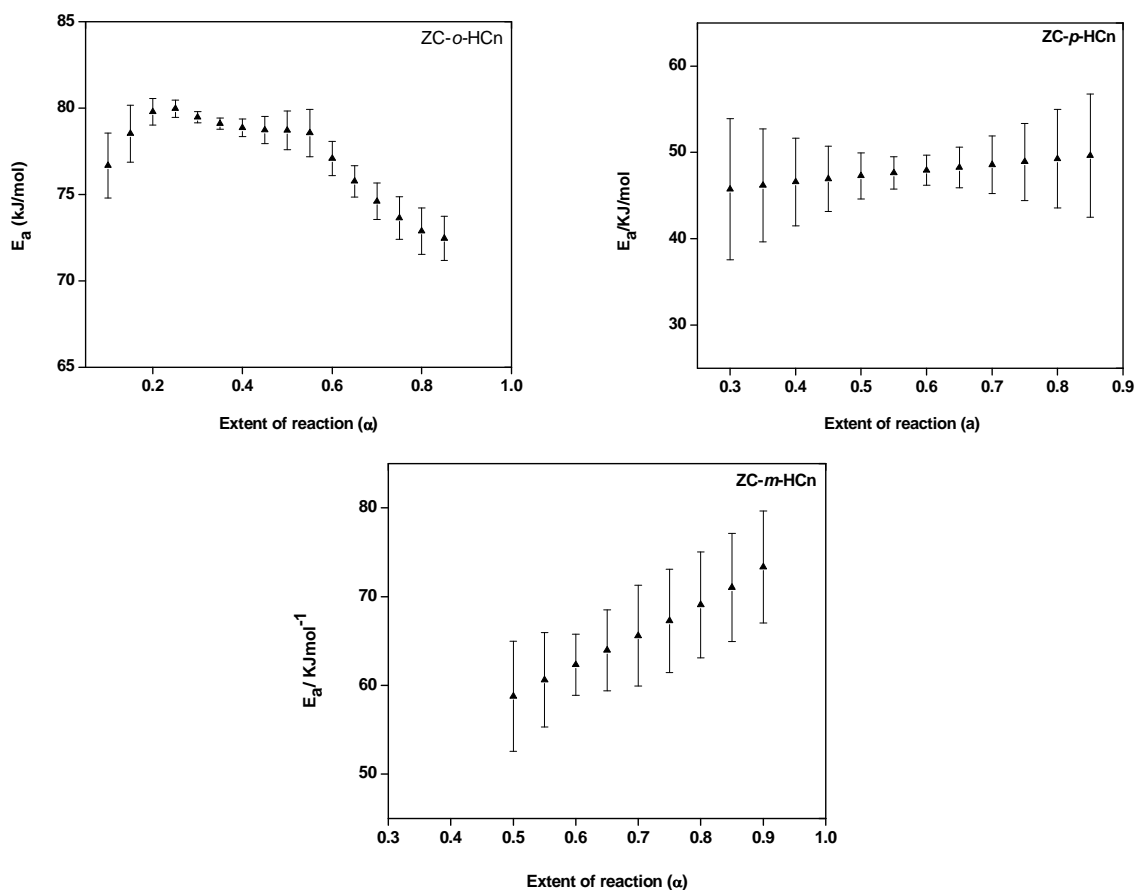
Figure 4.10: Variation of effective E_a with α for ZC-*m*-HCn, ZC-*o*-HCn and ZC-*p*-HCn.

The E_a values for ZC-*o*-HCn are constant up to extent of conversion of 0.5 with values ranging from about 77 kJ mol^{-1} to 79 kJ mol^{-1}, and then drop to a final value of 72 kJ mol^{-1} at the end of reaction. Although there are significant changes in the E_a at higher conversion, the values are still within 10 % so that the mechanism of reaction could still be the same. Ion exchange reactions in layered materials have been shown to occur from layer to layer starting at the outermost layer with the exchange in one layer weakening the electrostatic attraction between the layers and the anions in the neighboring layer.[171]

This might have resulted in the low and linear decrease of E_a as the reaction proceeded at higher conversion, above $\alpha = 0.5$. There may be a high energy transformation occurring at low conversion which might have resulted in the induction period observed in the PXRD analysis. Although the induction period is small, the process might still be governing the energetics of the reaction even during the exchange period resulting in constant energy observed up to extent of reaction of 0.5. Since E_a values for exchange reactions at the anion binding sites have been shown to range from 30-70 kJ mol^{-1} depending on the nature and size of the guest anions,[75;168;179] the reaction may be controlled by chemical reaction at the exchange site. It is also important to note that diffusion of anions in a dense organic matrix can have high E_a values sometimes being more than 100 kJmol^{-1},[178] as such diffusion limited process cannot be ruled out if the anions are closely packed in the gallery. The E_a values for the release of *m*-HCn and *p*-HCn are in the range of both reaction controlled process and diffusion controlled processes.[190] The fact that the E_a does not significantly change over the entire reaction may indicate that the reaction is diffusion controlled. The differences in the mechanism between *o*-HCn release and the other two systems may be due to different strength of interactions with the layers. The presence of H-bonding between the layers and the *o*-HCn anions may bring the anions closer to the layers resulting in increased electrostatic attraction resulting in the process being controlled by reaction at the exchange site.

Since there is no significant variation of the E_a with conversion for *m*-HCn and *p*-HCn release, and the energy difference for *o*-HCn release is too low to reflect a change in mechanism, model based approach was used to obtain the rate constants for the reaction.

The experimental data was fitted to different release kinetic models which include the first order model, parabolic diffusion model, generalized model, and modified Freundlich model. These models have been used extensively to describe solution phase ion exchange reactions in HDSs and LDHs.[135;191;192] Non linear regression analysis was performed on the four kinetic models in order to determine the model which best fit the experimental results. The correlation coefficient (R^2) and the chi-square value (χ^2) were used to discriminate between the models. Summary of the results are shown in Table 4.3, and the linear plots are shown in Appendix E-G. From Table 4.3 it can be observed that the release data for all the three nanohybrids were described by different kinetic models. First order model being the best fit for ZC-*o*-HCn, parabolic diffusion was the best model for ZC-*p*-HCn, and ZC-*m*-HCn was best described by the modified Freundlich model. The fact that the release data for the different isomers was described by different models makes it impossible to compare the release rates of the isomers. To circumvent this problem, the Avrami-Erofe'ev nucleation-growth model was used,[109;110] this model has the advantage that it can be used to describe and compare reactions occurring via different mechanisms.[114]

Table 4.3. Fitting release data to different release kinetic models.

| Nanohybrid | Temperature (°C) | Kinetic models | | |
		First order (R^2)	Modified Freundlich (R^2)	Parabolic diffusion (R^2)
ZC-*o*-HCn	30	**0.9924**	0.9881	0.9504
	40	**0.9955**	0.9736	0.9327
	50	**0.9858**	0.9760	0.9358
	60	**0.9916**	0.9839	0.9623
ZC-*p*-HCn	30	0.5559	0.9750	**0.9827**
	40	0.5565	0.9783	**0.9987**
	50	0.5892	0.9598	**0.9831**
	60	0.7362	0.9682	**0.9949**
ZC-*m*-HCn	30	0.6758	**0.9873**	0.9688
	40	0.6928	**0.9735**	0.9717
	50	0.7338	**0.9715**	0.9594
	60	0.7462	**0.9719**	0.9527

The extent of reaction versus time plots obtained for the ZC-*o*-HCn/Cl⁻exchange reactions at different temperatures are shown in Figure 4.11. The Avrami–Erofe'ev model was applied to, and correctly describes the obtained experimental data within the range of 0.15-1.0. The validity of the Avrami –Erofe'ev model can be confirmed by the corresponding double logarithmic plots in Figure 4.11 (insert) where straight lines were obtained with R^2 values ranging from 0.996-0.999. The double logarithmic plots are almost parallel indicating that the reaction proceeds with the same mechanism over the

temperature range used here. The obtained *n* value was close to 1.0 indicating diffusion controlled mechanism following instantaneous nucleation. The release profiles together with the Sharp-Hancock plots for the release of *m*-HCn and *p*-HCn are shown in Figure 4.12 and Figure 4.13 respectively.
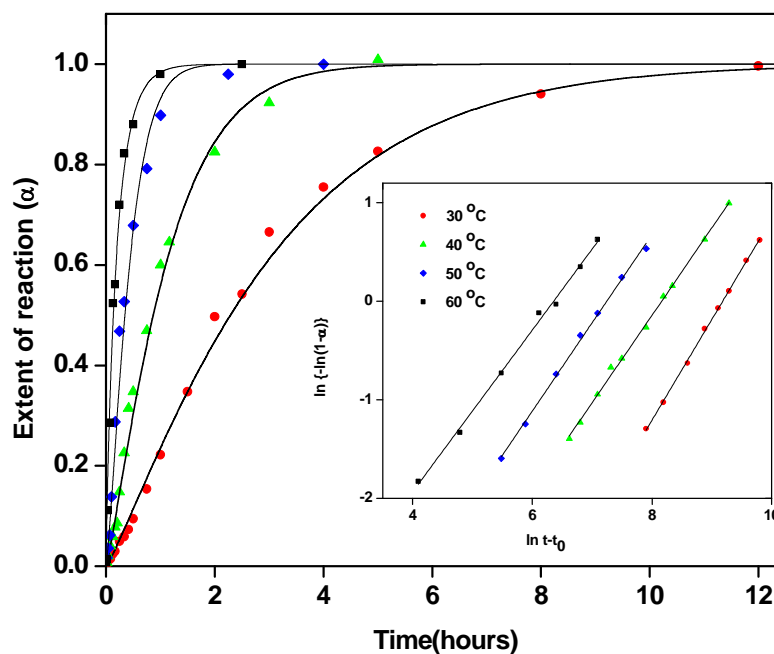
Figure 4.11: Extent of reaction as a function of time for the exchange reaction of Cl⁻ anion and ZC-*o*-HCn at various temperatures: 60°C (■), 50°C (♦), 40 °C (▲), 30°C (●), the extent of reaction data has been fitted to Avrami –Erofe'ev equation. Insert; corresponding Sharp-Hancock plots

The kinetics of *m*-HCn release follows the Avrami –Erofe'ev model, the data provided a good fit within the range $0.15 < \alpha < 0.85$ (Figure 4.12), the fit to limited range of α has been observed in other intercalation reactions.[75;116] Anomalously low values of the Avrami exponent observed here (Table 4.3) have been reported in polymer and alloy crystallization and do not have physical meaning.[193;194] The Avrami exponent values

obtained for the release of *p*-HCn are close to 0.5 which is consistent with diffusion

controlled reactions.[67] Summaries of the kinetic parameters obtained from the Sharp-

Hancock analyses of all the isomers are presented in table 4.4.
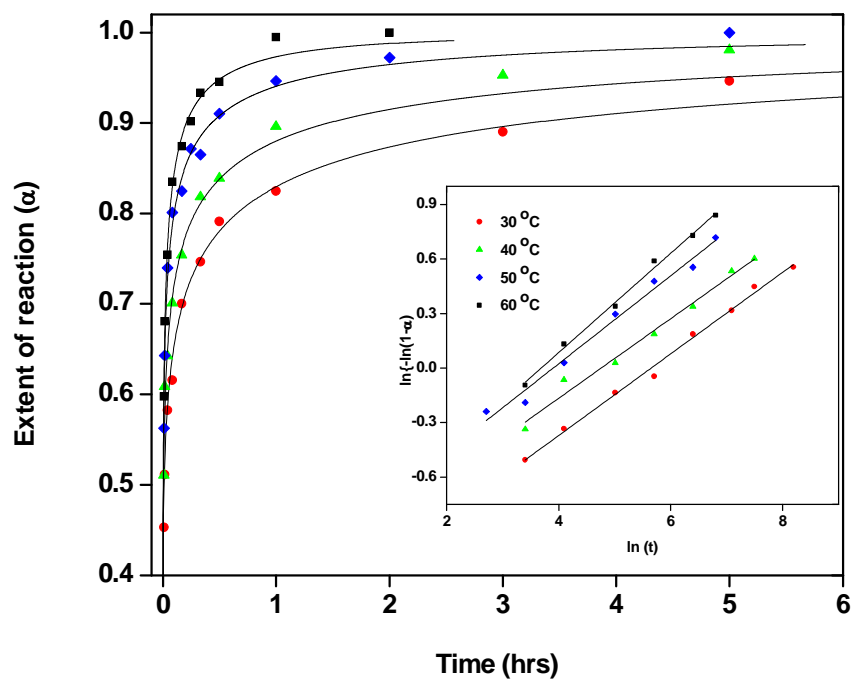
Figure 4.12: Extent of reaction as a function of time for the release of *m*-HCn at various temperatures: 60°C (■), 50°C (♦), 40°C (▲), and 30°C (●), the extent of reaction data has been fitted to Avrami –Erofe'ev equation. Insert shows Sharp-Hancock plots
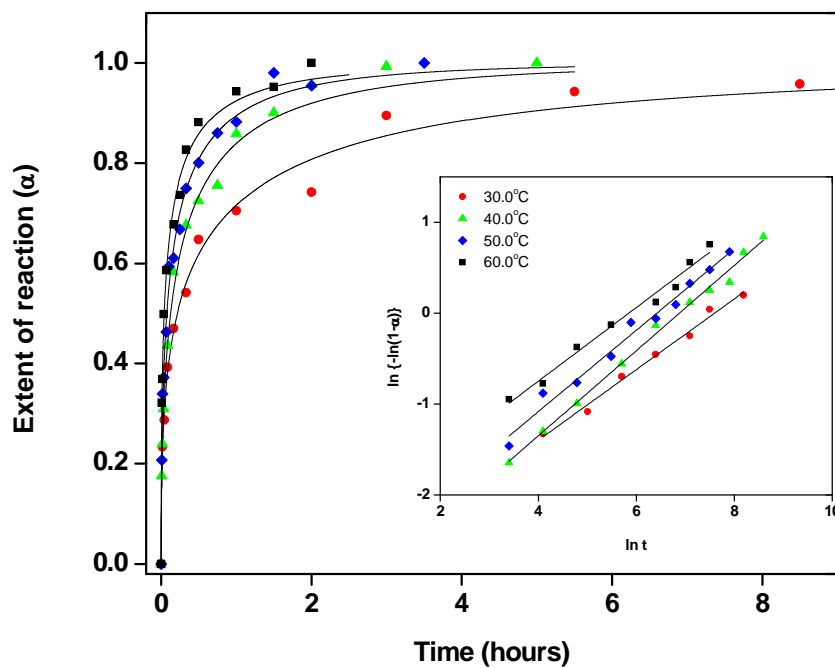
Figure 4.13: **Extent of reaction as a function of time for the release of *p*-HCn at different temperatures: 60°C (■), 50°C (♦), 40°C (▲), and 30°C (●); the extent of reaction data has been fitted to Avrami –Erofe'ev equation. Insert shows Sharp-Hancock plots**

Table 4.4: summary of kinetic parameters obtained at different temperatures

Nanohybrid	Temperature (^{o}C)	n	k s^{-1}($*10^{-3}$)
ZC-*o*-HCn	60.0	0.82± 0.02	1.7 ± 0.3
	50.0	0.90±0.02	0.7 ± 0.1
	40.0	0.88±0.01	0.29 ± 0.05
	30.0	1.02±0.01	0.10 ± 0.01
ZC-*m*-HCn	60.0	0.24± 0.01	31 ± 9
	50.0	0.24± 0.01	20 ± 7
	40.0	0.21± 0.02	7 ± 2
	30.0	0.225 ± 0.007	3.5 ± 0.8
ZC-*p*-HCn	60.0	0.41± 0.01	2.9 ± 0.5
	50.0	0.45± 0.02	1.6 ± 0.4
	40.0	0.46± 0.01	1.0 ± 0.2
	30.0	0.39± 0.01	0.5 ± 0.1

From Table 4.4 it can be concluded that the rate of release of *m*-HCn from the nanohybrids is much faster as compared to the other isomers, the rate constants at 40°C were 7± 2 x10^{-3} s^{-1} for *m*-HCn, 1.0 ± 0.2 x10^{-3} s^{-1} for *p*-HCn, and 0.29 ± 0.05 x10^{-3} s^{-1} for *o*-HCn. The rate of release follows the following order.

m-HCn > *p*-HCn > *o*-HCn

Major factors which may influence the rates of release include interactions between the metal hydroxide layers and the anions, anion-anion interactions within the

layers and in the exchange medium, and solvent-anion interaction.[67] It is expected that these factors will have a complex effect on the reaction rates since they affect each isomer differently, the existence of hydrogen bonding (intra and intermolecular) further complicates these systems. There is a complex interplay of the above mentioned factors and in most cases it is difficult to come up with a simple relationship between the rate of release and any of aforementioned factors.[67] The presence of hydrogen bonding within the interlayer space reduces the Gibbs free energy of formation of the nanohybrids and stabilizes the system. The rate of release of ions then depends on the differences in the enthalpy of nanohybrid formation and the barrier to reaction. As indicated in Figure 4.3, the level of hydrogen bonding in ZC-*o*-HCn is higher than in ZC-*p*-HCn with ZC-*m*-HCn having the least. The less stable nanohybrid proceeds more quickly to equilibrium, this is consistent with results obtained here, and the higher energy of the ZC-*m*-HCn nanohybrid could be responsible for the instant (burst) release observed.

There was considerable effect of position of the OH substituent on the rate and extent of release of the isomers. Additional experiments, including studies on other isomeric anions and effect of metal layer composition will be helpful in further elucidating how the position of substituents control the rate as well as the extent of reaction.

4.5   Conclusions

The kinetics of anion exchange reactions in hydroxy double salts are affected by the structure of intercalated anions. There is a strong interplay between thermodynamics and kinetics of the release reactions. The presence of interlayer hydrogen bonds affected the rates of the reaction while the extent of reaction was correlated to the magnitude of dipole moments. There is a significant effect of isomerism on the rate and magnitude of release of isomers of hydroxycinnamate. While the release of the meta isomer was instantaneous and fast, the ortho isomer release exhibited a slower, more sustained and complete release.

Chapter 5 . The effect of boron-containing layered hydroxy salt (LHS) on the thermal stability and degradation kinetics of poly (methyl methacrylate).

5.1   Introduction

The use of nanoparticles as polymer fillers has been extensively studied; this is largely because the polymer nanocomposites so produced show improved physical and mechanical properties such as reduced flammability, improved barrier properties, increased tensile modulus and deflection temperature.[51;196-199] Nanoscale layered silicates and anionic clays have recently attracted a lot of attention as polymer fillers as they can be used at relatively low loadings and do not have the negative environmental effects associated with halogen-based fillers.[143;144] Although the majority of studies have been focused on montmorillonite (MMT) and layered double hydroxides (LDHs),[34;36;53;57;58;200;201] work in this lab has shown that another class of anionic clays, layered hydroxy salts (LHSs) and hydroxy double salts (HDSs), although not extensively studied as MMT and LDH, improve fire properties of polymeric materials. [38-40]

LHS can be represented as $[M^{2+}_2 (OH)_{3(1-y)/n}] A^{n-}_{(1+3y)/n} \cdot m\ H_2O$ where A^{n-} is an exchangeable interlayer anion.[155] These materials offer the possibility of varying the identity of both the metal constituents and the exchangeable interlayer anions which enable tuning physic-chemical properties of the materials in order to optimize their performance for selected applications. The preparation methods of LHSs usually results in incorporation of small inorganic anions as charge balancing ions in the interlayer

space. To improve compatibility between the LHS and polymer matrix, and tune the physic-chemical properties, the LHSs have to be modified by exchanging the inorganic ions with organic ions, preferable long chain ions.

Boron containing compounds such as borates have been shown to improve the fire properties of polymers by forming glass char which acts as a gas barrier inhibiting oxygen penetration and preventing volatile degradation products being exposed to the fire.[202] Degradation of boron containing polymers have been shown to result in the formation of boric acid which enhance charring,[203-207] and in the presence of zinc oxide, zinc borate (a potent FR) may be formed.[208] Work in this lab has shown that polymer composites of copper LHSs resulted in lowering of total heat release (THR)[40] as compared to LDHs which typically results in lowering of peak heat release rate (PHRR).[35] The significant reduction in THR, of up to 30%, achieved using LHS[40] suggests that with careful choice of intra-layer metal ions and interlayer anions, a system can be obtained in which reductions in both THR and PHRR may be achieved.

The modification of zinc LHS, zinc hydroxy nitrate (ZHN), with boron containing exchangeable anions and compounding with PMMA will result in a polymer composite containing zinc and boron. It is envisaged that during the degradation process boric acid, zinc oxide, and subsequently zinc borate will be formed enhancing char formation, reducing gas permeability and thereby reducing polymer flammability and increasing thermal stability.

5.2   Experimental

5.2.1   Materials

Poly (methyl methacrylate) (PMMA) {MW 120,000, Tg 99.0^{o}C, viscosity 0.200}

containing <5.0% toluene, sodium hydroxide (flakes, 98%) and zinc nitrate hexahydrate,

99% [Zn(NO$_3$)$_2$·6H$_2$O] were all obtained from Sigma Aldrich Chemical Co; Zinc oxide

(99%), was obtained from Mallinckrodt Baker inc; 4-(4,4,5,5-Tetramethyl-1,3,2-

dioxaborolan-2-yl) benzoic acid, 97 % [C$_{13}$H$_{17}$BO$_4$] was purchased from Strem

chemicals, Inc. All chemicals were used without further purification.

5.2.2   Preparation of LHSs and their PMMA nanocomposites

The anion used for modifying ZHN, {4-(4, 4, 5, 5-tetramethyl-1, 3, 2-

dioxaborolan-2-yl) benzoate (TMDBB)}, was prepared by reacting the acid {4-(4, 4, 5, 5-

tetramethyl-1, 3, 2-dioxaborolan-2-yl) benzoic acid, (TMDBBH)} with an equimolar

amount of sodium hydroxide in a volume of deionized water to make a 0.15 M solution.

The exchange reaction was accomplished by reacting ZHN (0.1g) with 3.75 cm^3 of a 0.15

M solution of TMDBB at 40°C for 48 hours with frequent stirring. The exchange product

was filtered, washed several times with deionized water and dried at 40°C in a vacuum

oven for 48 hours. The exchange product is referred herein as ZHTMDBB.

The composites of PMMA and ZHTMDBB were prepared via melt blending. In

this procedure, PMMA and the corresponding amount of ZHTMDBB (to give the desired

percent loading) were thoroughly mixed and placed in a Brabender Plasticorder chamber at a temperature of 185°C. The screw speed was set to 60 rpm and the blending time was 10 minutes. A reference sample of pure PMMA was subjected to the same melt blending treatment in the plasticorder. The resultant composites are identified as PMMA/ZHTMDBB-*n,* with *n* indicating the percent additive loading by mass. For example, 90 g of PMMA was mixed with 10 g ZHTMDBB to give an additive loading of 10% resulting in a composite referred to as PMMA/ZHTMDBB-10. Additive loadings were 3%, 5%, and 10% giving composites referred herein as PMMA/ZHTMDBB-3, PMMA/ZHTMDBB-5 and PMMA/ZHTMDBB-10.

5.2.3   Characterization Methods

Fourier transform infrared spectral data of the synthesized materials and the composites were obtained on a Perkin Elmer Spectrum 100 FT-IR spectrometer operated at a 2 cm^{-1} resolution in the 4000 - 650 cm^{-1} spectral range. The obtained data was an average of 16 scans. Powder X-ray diffraction patterns were recorded in the 2θ range of 2.0^{o} - 45.0^{o} for powders and 2.0^{o} – 10° for composites, data acquisition was performed using a step size of 0.083^{o} per second. The specifications of the diffractometer are presented in chapter 2. Powder samples were pressed in to the trough of glass sample holders while polymer samples were compression molded into thin rectangular plaques and mounted on aluminum sample holders.

Thermogravimetric analysis was conducted using samples in the range of 11.0 ± 0.2 mg, using TGA analyzer specified in chapter 2. The samples were cut into small pieces of

approximately 0.4 mm thick and heated in an aluminum oxide crucible. General thermal

stability data was acquired from 50 ^{o}C to 800 ^{o}C under a constant flow of nitrogen or air

at a flow rate of 20 ml min^{-1} and a heating rate of 20 ^{o}C min^{-1}. For polymer kinetic

analysis, various heating rates ranging from 5 ^{o}C min^{-1} to 25 ^{o}C min^{-1} were used. To

study the effect of sample weight on kinetic parameters, samples containing 10% loading

of the additive were used. Total mass of 5.0-20.0 mg were heated under nitrogen

atmosphere. Flammability analyses were conducted at an incident heat flux of 50 kW/m^2

with the samples in a horizontal orientation. The samples were compression molded into

square plaques of uniform size (100 mm x 100 mm x 3 mm) and weighing about 30.0 g.

The reported values for each sample were the average of three measurements. Bright

image field transmission electron microscopy (TEM) images were collected at 60kV

using a Zeiss 10c electron microscope. Elemental analysis was carried out by Huffman

labs, Colorado, using atomic emission spectroscopy interfaced with inductively coupled

plasma (AES-ICP) for metal determination. **ZHN**; Zn (54.11% exp, 55.38% calc); N

(3.52% exp, 3.61% calc); H (1.88% exp, 1.90 % calc); C < 0.05% corresponding to the

formula $\mathbf{Zn_{6.5}(OH)_{11.2}(NO_3)_2 \cdot 1.8H_2O}$.

5.3   Results and Discussion

5.3.1   Characterization of filler material.

To tune the prepared LHS for flame retardation applications, the precursor LHS (ZHN) was modified by incorporating a larger boron containing anion, TMDBB (shown in Figure 5.1) into the interlayer space. The advantages of having a filler material which contain both zinc and boron have been highlighted in section 5.1. The intercalation of TMDBB into the layers was achieved via anion exchange. The anion exchange process may have resulted in the decomposition of the TMDBB anion as indicated from the formula obtained from elemental analysis, $Zn_5(OH)_{9.3}(C_{13}H_{16}BO_4)_{0.8} \cdot 2.3H_2O \cdot 0.7BO_2$. The elemental composition of ZHTMDBB indicates that nitrogen level was insignificant suggesting complete exchange of nitrate with TMDBB.
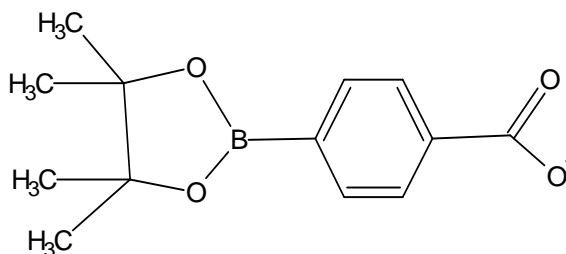
Figure 5.1: Chemical structure of 4-(4,4,5,5-Tetramethyl-1,3,2-dioxaborolan-2-yl) benzoate (TMDBB).

Infrared spectra of ZHN and ZHTMDBB are shown in Figure 5.2 traces (a) and (b) respectively. For both ZHN and ZHTMDBB, the OH stretching vibrations of the

hydroxyl group appear in the region from 3300 cm^{-1} to 3574 cm^{-1}. For ZHN, the sharp

band at approximately 3576 cm^{-1} can be assigned to stretching vibrations of free layer

hydroxyl groups and the band at about 3472 cm^{-1} is due to the stretching of layer

hydroxyl groups that are hydrogen bonded to the interlayer nitrate anion or water

molecules. The broad band at about 3300 cm^{-1} can be assigned to the stretching of water

hydroxyl groups.[152] The band at 1644 cm^{-1} can be assigned to water bending mode, the

D_{3h} symmetry of the free nitrate is slightly distorted as evidenced by the appearance of a

weak NO stretch band at 1022 cm^{-1} which is forbidden for NO_3^- in a D_{3h}

symmetry.[23;209;210] The OH stretching assignments in ZHN can also be used to describe

the OH stretching vibrations in ZHTMDBB. Trace b in Figure 5.2 indicates that after the

exchange reaction, the characteristic asymmetric stretch of free nitrate ion at about 1372

cm^{-1} in ZHN[157;209] had disappeared and a new set of peaks at 1398 cm^{-1} ν (B—O), 1580

cm^{-1} ν_{asym} (C=O) and 1533 cm^{-1} ν_{sym} (C=O)[152;157] appeared indicating that the nitrate

group was completely exchanged consistent with results of elemental analysis.
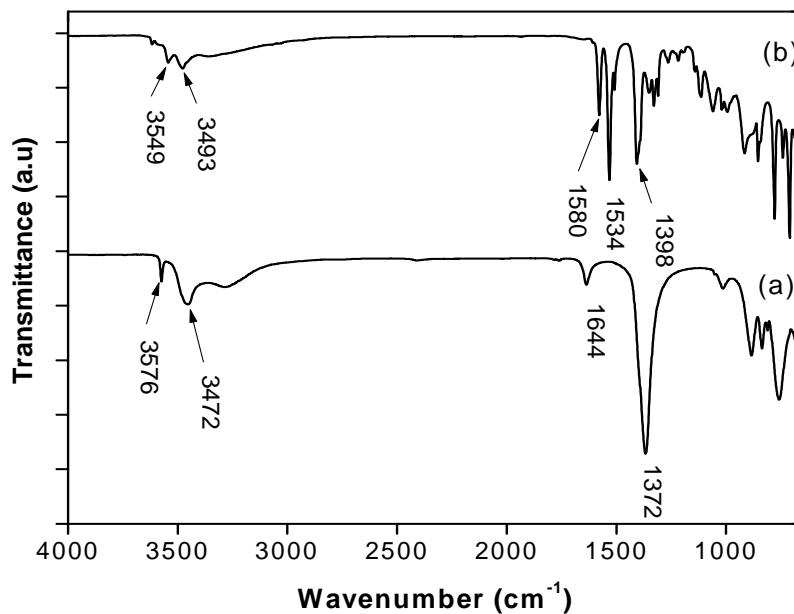
Figure 5.2: FTIR spectra of zinc hydroxy nitrate LHS (trace a) and zinc hydroxy TMDBB LHS (trace b). Traces are offset for clarity but not otherwise scaled.

Both the precursor LHS (ZHN) and the exchange product (ZHTMDBB) are layered and possess high range of ordering in the c direction as indicated in Figure 5.3. ZHN has been indexed as the monoclinic $Zn_5(OH)_8(NO_3)_2 \cdot 2H_2O$ (PDF # 24-1460)[154].The PXRD patterns for both materials show intense *00l (l =*1 to 3) reflections which are equally spaced. The d-spacing of ZHN, 0.97 ± 0.01 nm, calculated using the Bragg equation[148] is comparable to literature values.[4;152] After anion exchange with TMDBB, new (*001-003*) peaks appeared at low 2 theta values corresponding to an average d-spacing of 1.452 ± 0.003 nm. The absence of the nitrate reflections from the ZHTMDBB trace indicates that the exchange was complete, confirming results from elemental analysis and FT-IR analysis. The expansion of the interlayer space, from 0.97 ± 0.01 nm

in ZHN to 1.452 ± 0.003 nm in ZHTMDBB, is consistent with a smaller NO_3^- anion (thermochemical radius = 1.65Å) being replaced by a larger TMDBB anion (chain length = 10.9Å). The average crystallite sizes calculated using the Scherrer formula were found to be 60 ± 3 nm and 42 ± 1 nm for ZHN and ZHTMDBB respectively, an indication that the crystals got smaller during the ion exchange process. From the crystallite sizes and the basal spacings of the materials, the average diffracting domains of ZHN are composed of 61 layers as opposed to ZHTMDBB which is composed of 30 layers.
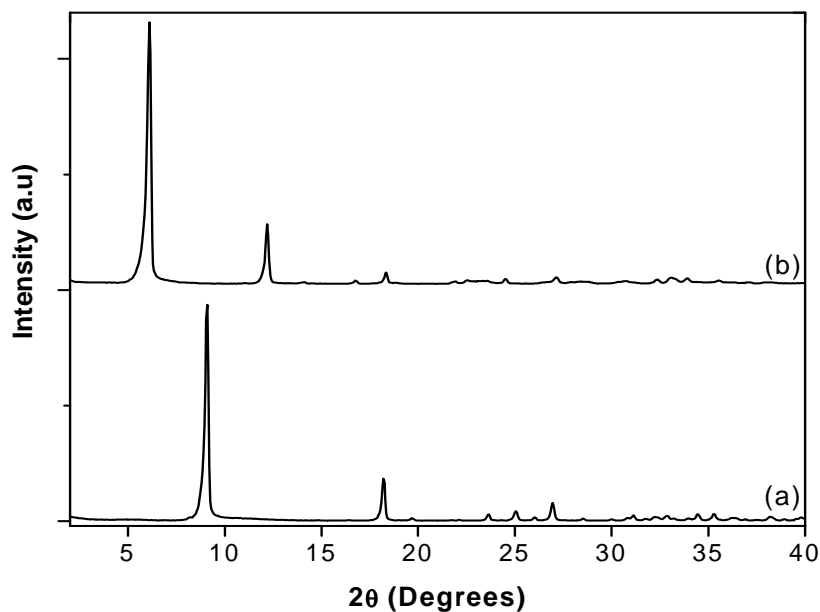
Figure 5.3: Powder x-ray diffraction data for (a): ZHN which has been indexed as Zn$_5$(OH)$_8$(NO$_3$)$_2$·2H$_2$O and JCPDS file 24-1460 and (b): ZHTMDBB. Traces are offset for clarity but not otherwise scaled.

Thermal analysis plots for ZHTMDBB, obtained at a heating rate of 20°C min^{-1}, are shown in Figure 5.4. The DTG curve indicates that there is weight loss from 50-150°C corresponding to the loss of adsorbed and intercalated water. The weight loss at

about 210°C, corresponding to about 10% weight loss, can be assigned to water loss due to dehydroxylation of the layers as confirmed by TGA-FTIR analysis shown in Figure 5.5. The decomposition of TMDBB starts at around 380°C. The TG shows that the decomposition of ZHTMDBB results in 65% inorganic residue at the end of the thermal decomposition process. The inorganic content obtained from TG is in agreement with the value of 68% calculated from elemental analysis results, assuming that the degradation process results in the formation of zinc oxide (ZnO) and zinc borate (ZnB_2O_6).
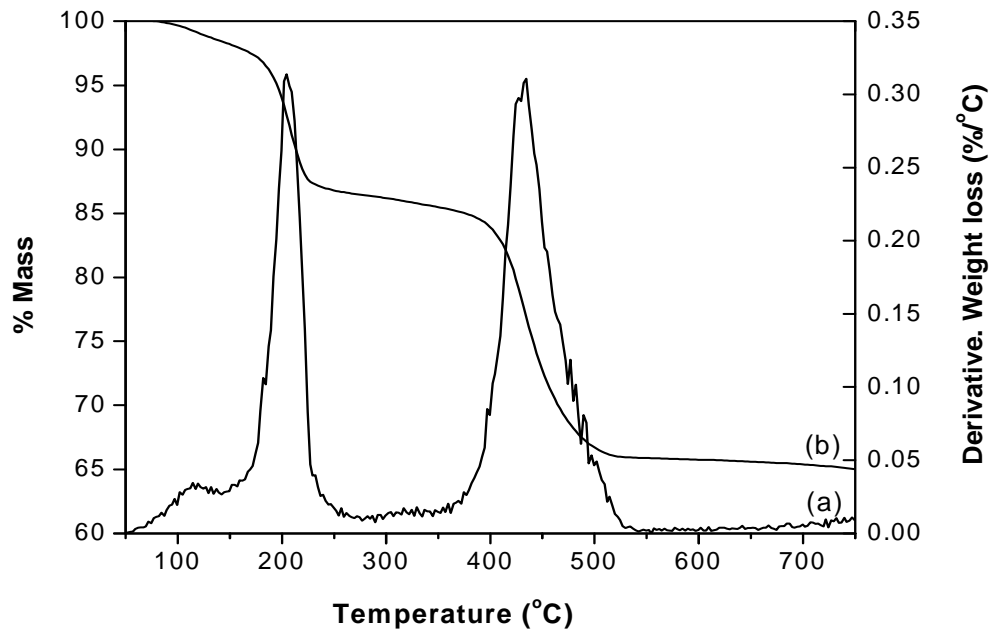
Figure 5.4: (a) DTG and (b) TG profiles for ZHTMDBB degraded in nitrogen at a heating rate of 20°/min.
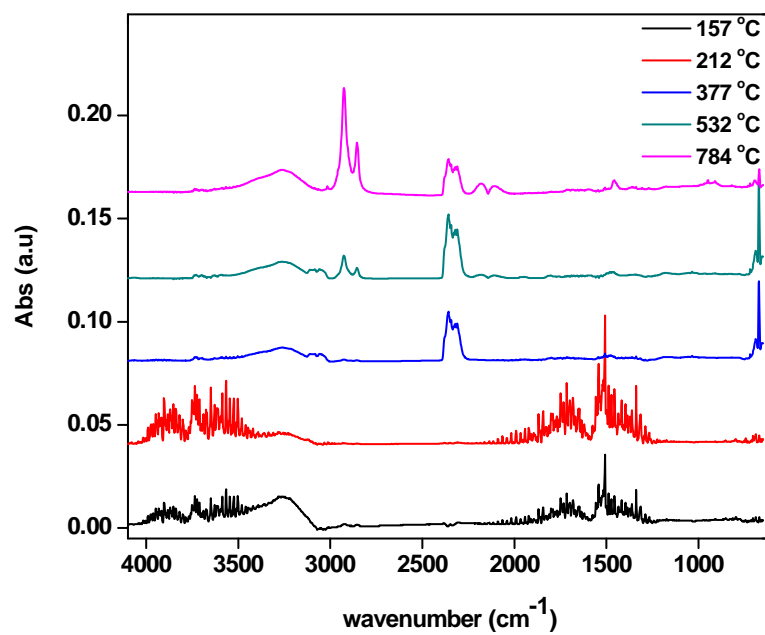
Figure 5.5: TGA-FTIR of ZHTMDBB at a heating rate of 20°C min⁻¹

5.3.2 Characterization of filler and polymer nanocomposites.

When ZHTMDBB was compounded with PMMA during melt blending, new reflections were observed at lower 2 theta values for all the three loadings as indicated in Figure 5.6. After melt blending the interlayer distance increased from 1.452 ± 0.003 nm for ZHTMDBB to 1.88 ± 0.05 nm for the composites. This expansion of the layers is consistent with some degree of intercalation of the polymer into the LHS gallery. The PXRD patterns in Figure 5.6 show at least two orders of reflections indicating that the layered structure of the LHS was maintained during the compounding process.
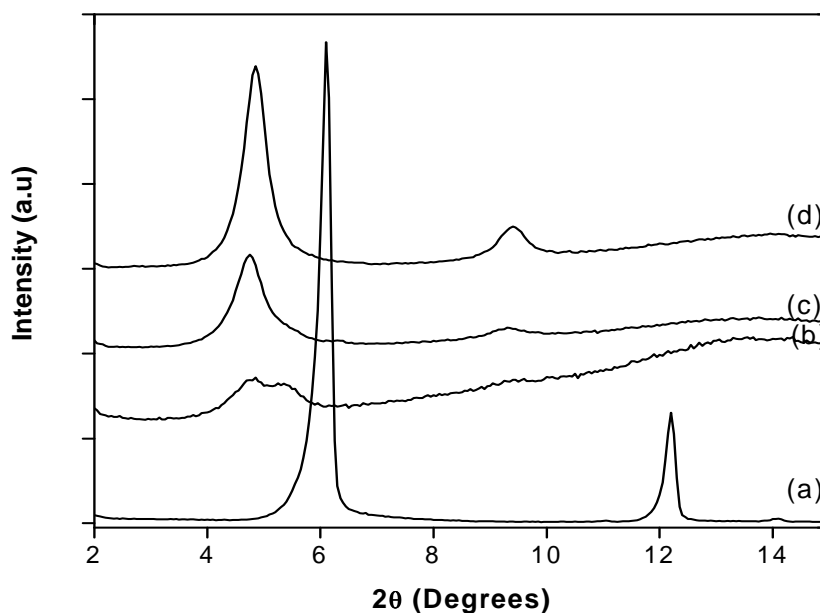
Figure 5.6: Powder x-ray diffraction data: (a) ZHTMDBB. (b) PMMA/ZHTMDBB-5. (c) PMMA/ZHTMDBB-3. (d) PMMA/ZHTMDBB-10. There is an increase in the basal spacing from 1.45 nm in ZHTMDBB to 1.88 nm in the composites.

XRD alone is insufficient to characterize the quality of dispersion of the additive in a polymer matrix; transmission electron microscopy (TEM) is required since it provides direct imaging of the composites allowing visualization of the additive dispersion. Figure 5.7 shows the TEM images for all the composites at both low and high magnifications. The low magnification provides information about the dispersion of the layered material in the polymer matrix while higher magnification provides information about the layered structure. The TEM images at low magnification in Figure 5.7 are consistent formation of microcomposites which are associated with poor dispersion, thus good nanodispersion was not achieved here. At higher magnification, the metal hydroxide sheets, which are represented by the dark regions, seem to have aggregated and formed tactoids, which increased with increase in the additive loading.
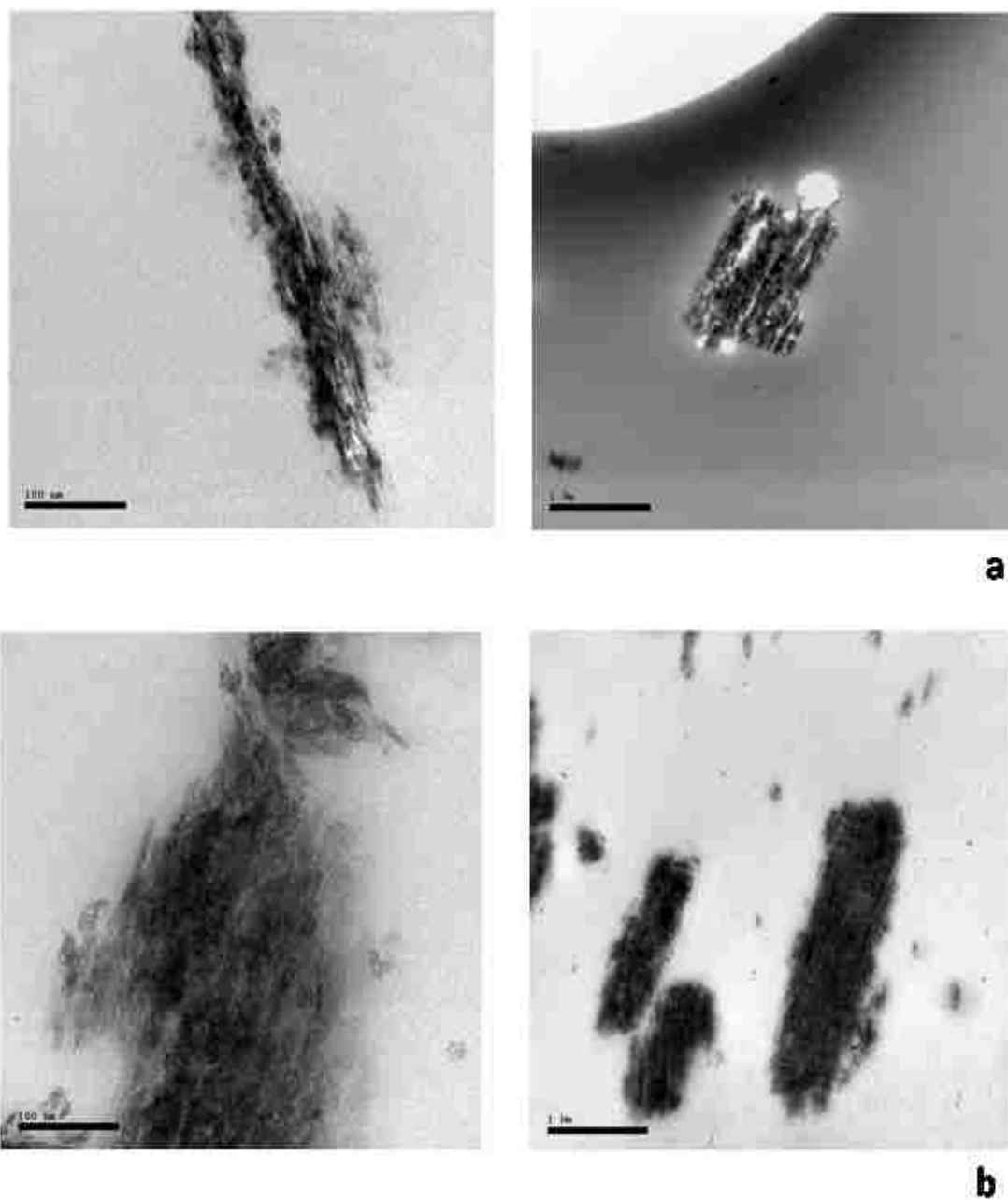
Figure 5.7: TEM images of polymer composites obtained by melt blending, (a) PMMA/ZHTMDBB-3 and (b) PMMA/ZHTMDBB-10; low magnification (right) and higher magnification (left).

The method of producing composites via melt blending has been shown not to result in significant degradation of commercial PMMA (MW 120,000).[35] Results from thermogravimetric analysis of PMMA and its composites degraded in air and nitrogen at a heating rate of 20°C per minute are shown in Figures 5.8 and 5.9 respectively. The plots show that pure PMMA (commercial; MW 120,000) degradation under the heating profiles used here is a two step process regardless of the atmosphere being used which is in agreement with results obtained by other workers.[36] The two steps in the degradation of pure PMMA have been attributed to scission at the vinyl terminated end and to random scission of the PMMA back bone respectively.[211] The initial stabilization of PMMA in air, although not very distinct in this work, has been reported elsewhere.[212;213] Hirata and core workers[212] have attributed the stabilization of PMMA at early stage to the modification of the terminal double bond in PMMA, by oxygen, which results in the suppression of the end initiation process. The destabilization of PMMA by oxygen at higher temperatures, the step which is due to random scission of the chain, is due to oxygen reacting with polymer chains enhancing the random scission process.

ZHTMDBB has a pronounced effect on the degradation of PMMA in air as shown in Figure 5.8a. The degradation profile changed significantly as can be observed from the DTG curves (Figure 5.8b) in which the rate of mass loss of the first step is significantly lowered in all the composites and there is a third step observed in the temperature range of 475 ^{o}C-550 ^{o}C. The degradation in air showed that the composites were more thermally stable than the virgin polymer. The onset of degradation, corresponding to 10% conversion ($T_{0.1}$), increased by between 32 and 44°C depending on

additive loading. There was also a corresponding increase in the temperature at 50% mass loss ($T_{0.5}$), the largest being 31°C for 10 % additive loading. The additive also had a stabilizing effect in inert atmosphere with increases in $T_{0.1}$ and $T_{0.5}$ being observed for the composites, although the magnitudes were lower than those achieved in air. The results obtained here indicate that the additive is more effective in air than in a nitrogen environment. These results are in agreement with those reported by Lee and Viswanath, who used aluminum nitride and alumina as additives,[214] and Laachachi and coworkers, who used the additives ZnO, Cloisite 30B[50] and antimony oxide. [215] Wang *et al.* have attributed the increased stability of PMMA composites in air, as compared to nitrogen, to the stabilization of free radicals by the inorganic compounds.[216] Increased thermal stability of PMMA when compounded with anionic clays has been reported before.[35;55;56]
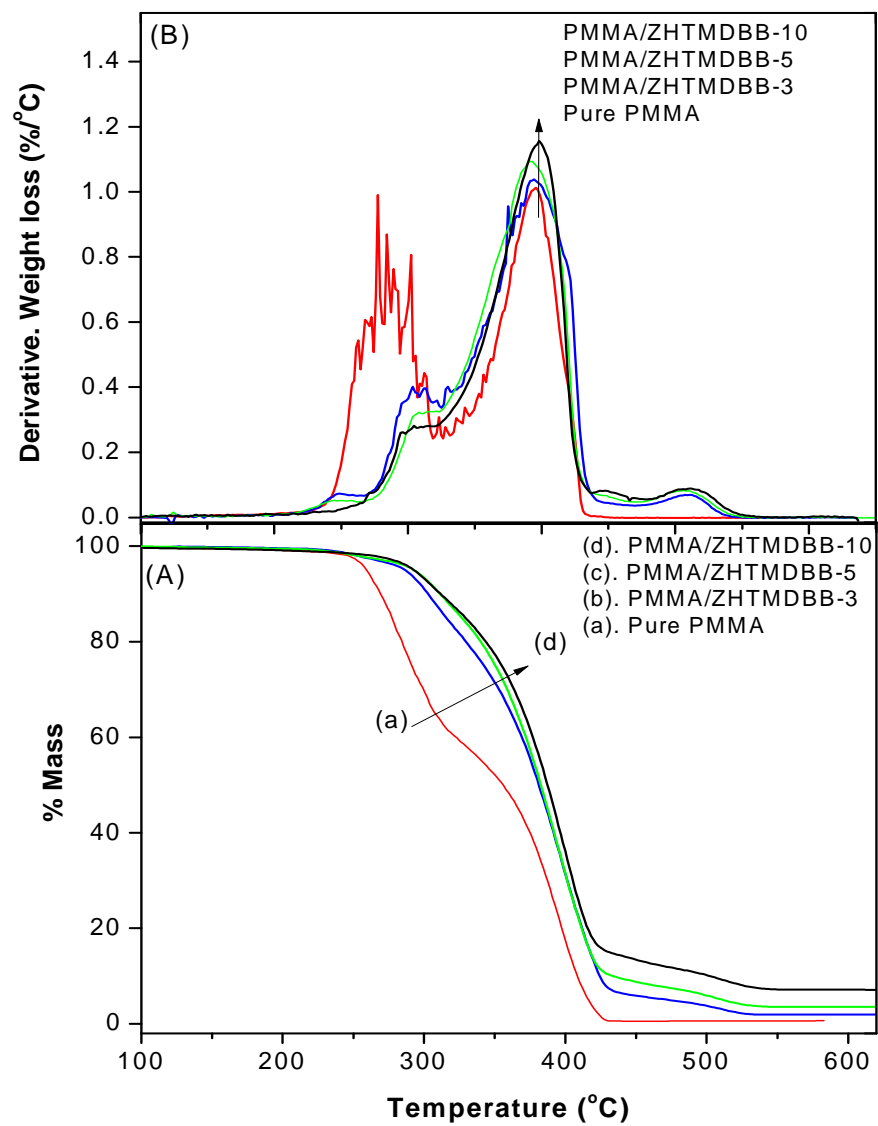
Figure 5.8: (A). TGA curves for PMMA and composites. (B). DTG curves for PMMA and composites degraded in air at a heating rate of 20°/min.
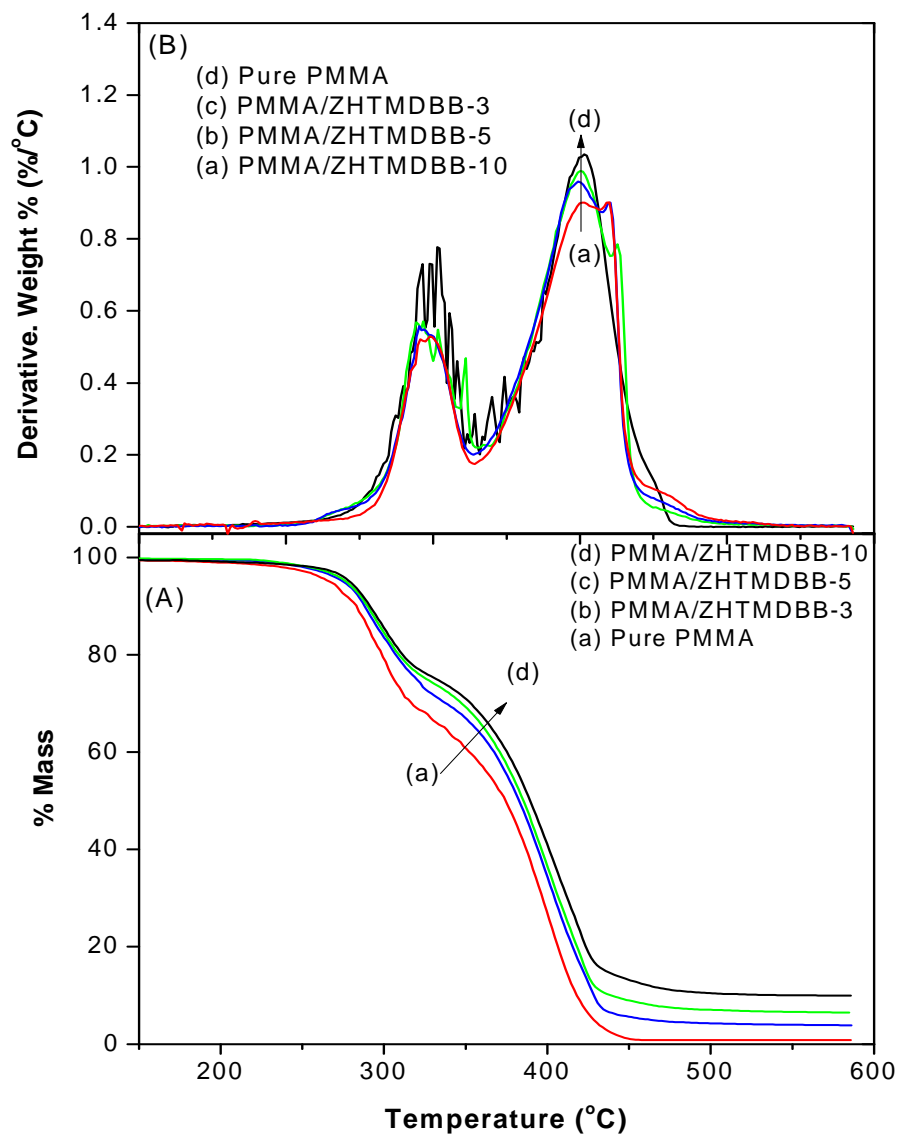
Figure 5.9: (A). TGA curves for PMMA and composites. (B) DTG curves for PMMA and composites degraded in nitrogen at a heating rate of 20°/min.

Details of the thermal properties of PMMA and its composites are summarized in Tables 5.1 and 5.2. The expected char yield was calculated from the amount of char remaining from the separately measured degradation of ZHTMDBB and pure PMMA. The percent loading of the additive was then factored in to calculate the individual contribution of the polymer and the additive. The results show that, under pyrolysis

conditions, the amount of char remaining is significantly higher than the expected char yield suggesting that under these conditions, the additive enhances char formation. The char yields for the degradation in air are lower than those obtained in nitrogen and almost equal to the expected yield. The low chair yield obtained under thermo-oxidative conditions maybe because there is initial formation of char which burnt off after the critical temperature was reached resulting in complete degradation of PMMA, these results are in agreement with those obtained by other workers.[216-218]

Table 5.1: Summary of TGA data for pure PMMA and composites at 20° C min^{-1} in N_2

Sample	T_{10} (^{o}C)	T_{50} (^{o}C)	ΔT_{50} (^{o}C)	% Char (expected)
Pure PMMA	284±1	374.1±0.5	—	0.78±0.05
PMMA/ZHTMDBB-3	289.4±0.5	384±1	10±1	4.0±0.1 *(2.6)*
PMMA/ZHTMDBB-5	290±1	385±1	11±1	6.5±0 *(3.9)*
PMMA/ZHTMDBB-10	293.0±0.5	389±0.5	14.9±0.7	9.8±0 *(7.0)*

Note: T_{10}, temperature at which 10 % mass loss occurs and is regarded as the onset of degradation; T_{50}, temperature at which 50% mass loss occurs; ΔT_{50} difference between T_{50} of the composite and pure PMMA. Entries in italics are the expected char based on the residue obtained during the decomposition of ZHTMDBB and pure PMMA samples.

Table 5.2: Summary of TGA data for pure PMMA and composites at 20°C min^{-1} in air

Sample	T_{10} (^{o}C)	T_{50} (^{o}C)	ΔT_{50} (^{o}C)	Char(%) (expected)
Pure PMMA	269.9±0.8	356±1.5	—	0.65± 0.08
PMMA/ZHTMDBB-3	303±2	382±1	26±1	2.2±0.4 *(2.0)*
PMMA/ZHTMDBB-5	311±3	383.7±0.8	27±1	3.6±0.1 *(3.6)*
PMMA/ZHTMDBB-10	314.0±0.8	387.1±0.8	31±1	7.0±0.1 *(6.7)*

Note: T_{10}, temperature at which 10 % mass loss occurs and is regarded as the onset of degradation; T_{50}, temperature at which 50% mass loss occurs; ΔT_{50} difference between T_{50} of the composite and pure PMMA. Entries in italics are the expected char based on the residue obtained during the decomposition of ZHTMDBB and pure PMMA samples.

Degradation of PMMA mainly results in the formation of the monomer (MMA) which is transported from the bulky polymer to the surface as bubbles rather than by diffusion.[219] Although the transport of the monomer does not limit the weight loss for pure PMMA, the formation of char or inorganic residue in the composites provides a barrier to the transport of MMA and should result in the transport process limiting the mass loss. The mixing of the polymer with the additive, which has about 65% inorganic content by mass, may result in the increase of thermal capacity which, together with the barrier to heat transfer due to char formation, leads to degradation of the composites occurring at higher temperatures than the pristine PMMA. Figure 5.10 shows mass difference curves, Δ mass % (difference between mass % of composites and pure PMMA) for composites in both air and nitrogen. A positive profile of the mass difference curve indicates that the composites are more stable than the pure polymer at a given temperature and the additive has thus enhanced the thermal stability of the polymer.

Conversely negative profiles indicate a destabilization effect of the additive. At all levels of loadings, in both air and nitrogen, the profiles are positive in the entire temperature regime indicating that the additive has a stabilizing effect in the entire degradation temperature range. The graphs also clearly show the effect of the additive in different environment, as the environment is changed from air to nitrogen the maximum stabilization temperature shifts from around 300°C to 420°C and the stabilization effect is lower in nitrogen as compared to air.
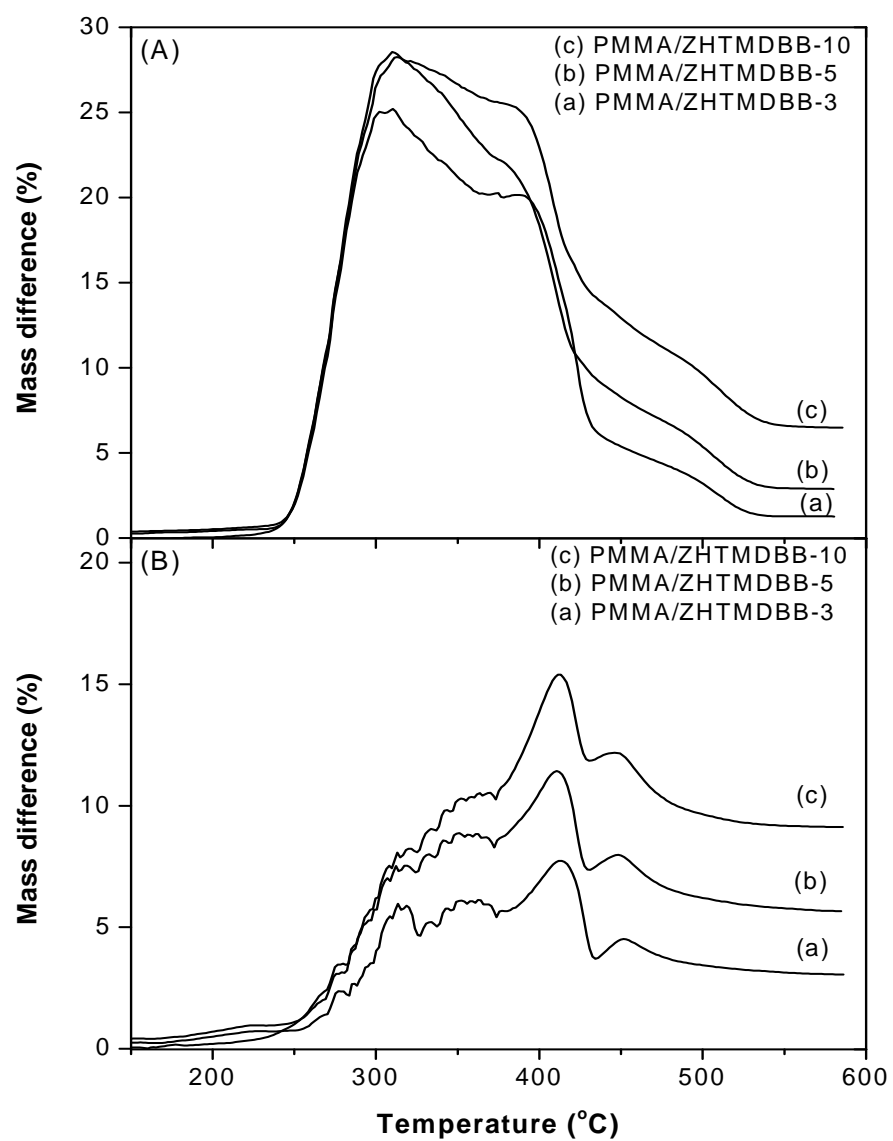
Figure 5.10: Mass loss difference curves for PMMA composites degradation at a heating rate of 20°/min. (A). Degradation in air atmosphere. (B). Degradation in nitrogen atmosphere.

5.3.3 Kinetic analysis

In order to get a better understanding of the degradation process and the effect of the additive on the thermal stability of PMMA, it is useful to determine kinetic parameters for the degradation process. The parameter generally found to be most useful in explaining the degradation process is the effective activation energy (E_a) which can be evaluated by carrying out kinetic analysis of the solid state reaction. For thermal methods of analysis, the techniques mainly used for the kinetic analysis are thermogravimetry (TG), differential scanning calorimetry (DSC) and differential thermal analysis (DTA). Both isothermal and non-isothermal methods can be used in kinetic experiments. Isothermal methods have a disadvantage because the sample requires time to reach the prescribed temperature and, during the temperature ramping process, the sample might undergo transformations that are likely to affect the results, therefore the process is restricted to lower temperatures.

Both isothermal and non-isothermal methods have been used in the determination of kinetic parameters in the degradation of polymers.[38;48;213;220;221] Dynamic thermogravimetric analysis was employed in this study to calculate the E_a for the degradation of PMMA and its composites by making use of the multiple heating rate kinetics (MHRK). Accordingly, a series of experiments were conducted at varying heating rates ranging from 5°C min^{-1} to 25°C min^{-1}. The Flynn-Wall-Ozawa method[222] incorporating Flynn's correction to the Doyle approximation[223] (referred herein as the cFWO method) together with the Friedman[224] and the Kissinger[225] methods were used in

the calculation of the E_a. The Flynn-Wall-Ozawa method can be written in a simplified

form expressed as:

$$\log f(\alpha) = \log\left(A\frac{E_a}{R}\right) - \log(\beta) - 2.315 - 0.4567\left(\frac{E_a}{RT}\right) \qquad \textbf{Equation 5.1}$$

In the above expression, $f(\alpha)$ is a conversional functional relationship; A is the pre-

exponential factor (min^{-1}); E_a is the activation energy ($kJ\ mol^{-1}$); R is the molar gas

constant; β is the heating rate ($^oC\ min^{-1}$) and T is the temperature (K).

Equation 5.1 can be rewritten as follows; [48]

$$\log(\beta) = -0.4567\left(\frac{E_a}{RT}\right) + constant \qquad \textbf{Equation 5.2}$$

From the linear form above, the isoconversional plot of log (β) vs 1/T should result in a

straight line in which the E_a can be extracted from the slope. To obtain this simple

equation, Flynn, Wall and Ozawa utilized the Doyle's approximation of the exponential

integral. [226] However this may result in significant errors of the calculated activation

energies. Flynn proposed a correction to the Doyle's approximation by using tabulated

correction factors which reduces the error of the calculated E_a.[223] Figure 5.11 shows a

plot of the E_a, estimated from the isoconversional plots, for the degradation of PMMA

and the composites in nitrogen. The TGA and DTG curves for the degradation of PMMA

and the composites in nitrogen (Figure 5.9) show that the degradation occurs in two steps

which were assigned to end initiation from the unsaturated double bonds and random

scission of the chain respectively.[211] The onset of the degradation process for pure

PMMA, which corresponds to 10% mass loss, has an E_a value of 143 kJ mol^{-1}. The E_a value increases gradually as the degradation process continues up to a value of 168 kJ mol^{-1} at 30% conversion, and then drops to 164 kJ mol^{-1} at 35% conversion, which corresponds to the transition from the first step to the second step of degradation. The E_a then increases to 184 kJ mol^{-1} at 40% conversion as the second step of degradation start, this increase is maintained throughout the latter part of the process up to a value of 329 kJ mol^{-1} at 90% conversion. The results obtained here are consistent with the mechanism of PMMA degradation whereby the first step is initiated from weak links therefore has a lower E_a than the second step which is due to random C-C scission.
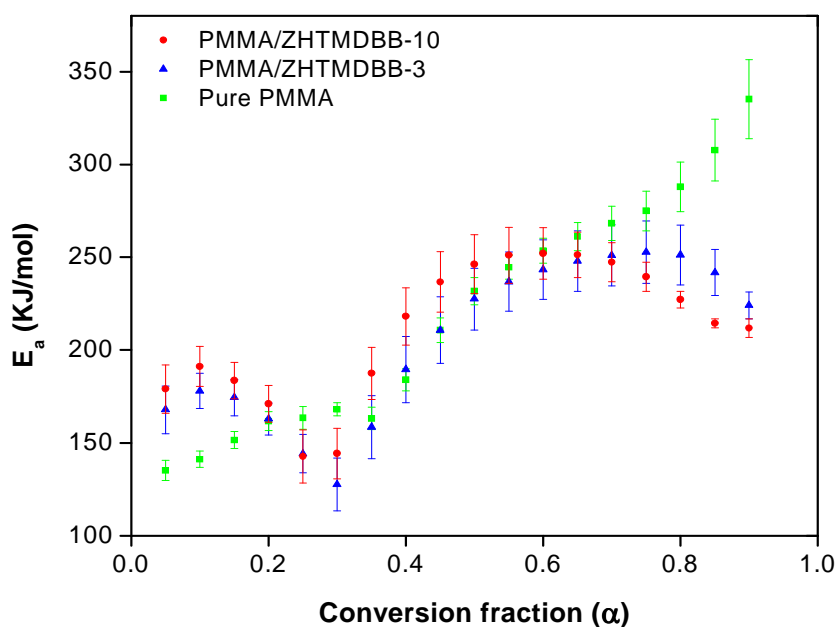
Figure 5.11: Dependence of Ea on the extent of reaction obtained by cFWO method under nitrogen atmosphere for pure PMMA (closed squares), PMMA/ ZTMDBB -3 (closed triangles) and PMMA /ZTMDBB -10 (closed circles).

Hu and Chen[227] carried out a study to determine the effect of weak links on the degradation of PMMA polymerized by using different initiators {lactans, thiols and 2,2´-azobisisobutyronitrile (AIBN)} producing PMMA with different end groups. Free radically polymerized PMMA had unsaturated end groups and degraded in two steps; they observed that the activation energy of the first step was lower than that of the second step (151-146 kJ mol^{-1} for 5-20% weight loss as compared to 218-222 kJ mol^{-1} for 80 - 90% weight loss). The E_a values obtained by Hu and Chen[227] agree qualitatively with those obtained in this work in that the first step has lower activation energy than the second step. The same general trend was also observed by Peterson *et al.* who reported effective E_a values of 190 kJ mol^{-1} for the first step and 230 kJ mol^{-1} for the second step.[213] Hirata *et al.*[212] did isothermal analysis of PMMA (obtained by free radical polymerization) and concluded that both steps follow first order kinetics with activation energy of the first step lower than that of the second step (31 kJ mol^{-1} and 210 kJ mol^{-1} respectively). The low Ea for the first step has, however, been attributed to volatilization of impurities by Holland and Hay.[228] It is important to note that the activation energies of the degradation process depend largely on the polymerization methods which determine the nature of end groups.[228]

The effect of the additive can clearly be seen in Figure 5.11, in which the composites have a significantly higher initial E_a at low conversion, corresponding to the first step of degradation, and lower activation energy towards the end of the reaction. The E_a of the composites at 3% and 10% loading show the same trend and the E_a values are not significantly different, this suggests that the level of additive loading does not have a

significant effect on the E_a values. The activation energy of the composites are higher at the onset of degradation (10% conversion) with PMMA/ZHTMDBB-10 having a value of 190 ± 10 kJ mol^{-1} and that of pure PMMA being 142 ± 4 kJ mol^{-1}. During the early part of the second degradation step, the E_a values of the composites and pure PMMA are not significantly different up to 80% conversion where the activation energies of the composites drop below those of pure PMMA. This trend was also observed by other workers,[229] and can be explained by considering that the additives act as barrier to heat and mass transfer thereby retarding the degradation process. The barrier effect require close contact between the polymer matrix and the additive, as the degradation process proceeds this close contact decreases leading to decrease of E_a of the composites. The effect of additives on the E_a of PMMA under nitrogen atmosphere has been investigated by many workers and the general trend of additives increasing the E_a has been observed, some additives increasing the E_a over the entire degradation process .[58;218;227;229]

The dependence of E_a on the extent of reaction for the degradation of PMMA and its composites in air is shown in Figure 5.12 which indicates that the degradation in air follows the general trend as in nitrogen with the additive increasing the E_a of the first step. The activation energies of the first degradation step of the pure polymer in air are comparable to those in nitrogen, ranging from 136-148 kJ mol^{-1} in air and 136-164 kJ mol^{-1} in nitrogen for 5% – 35% conversion. The activation energies of PMMA in air at higher conversions, corresponding to the second degradation step, are significantly lower than those obtained in nitrogen. These results are consistent with those obtained by Chang and Wu[217] who observed that the E_a in air at low conversion was significantly

higher than in nitrogen (217 – 172 kJ mol^{-1} in air and 125 – 160 kJ mol^{-1} in N$_2$ for conversions of 10-30%). The order was reversed at higher conversions (145 – 140 kJ mol^{-1} in air and 175 – 190 kJ mol^{-1} in N$_2$ for 40- 70% conversion), with the transition being at about 35% conversion. This is consistent with the stabilizing effect of oxygen on the degradation of PMMA.[213] The additive had the effect of increasing the activation energy of the first step of degradation, but did not have a significant effect on the E$_a$ of the second step. The additive may act by stabilizing or scavenging the free radicals generated during the initial stages of the thermal oxidative degradation process thereby increasing the barrier for reaction to occur. It was also noted that the additive resulted in much higher increases of the activation energy in air than in nitrogen (from 142 kJ mol^{-1} to 250 kJ mol^{-1} in air compared to 143 kJ mol^{-1} to 190 kJ mol^{-1} in nitrogen at 10% conversion) which is consistent with the additive stabilizing free radicals generated during thermal oxidative degradation.
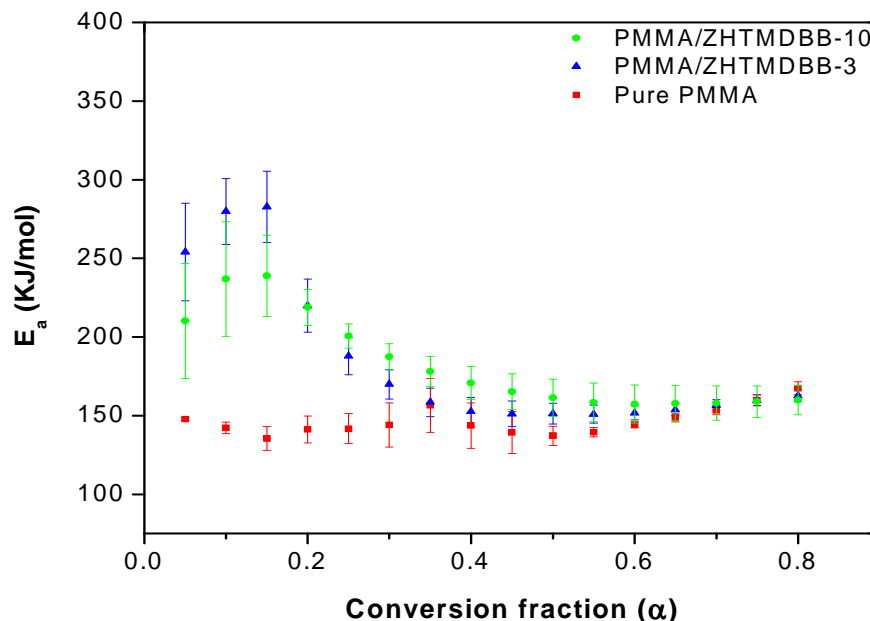
Figure 5.12: Dependence of Ea on the extent of reaction obtained by cFWO method for degradation under air for pure PMMA (closed squares), PMMA/ ZTMDBB -3 (closed triangles) and PMMA /ZTMDBB -10 (closed circles).

The Friedman method is a differential isoconversional approach for the calculation of E_a which is based on the rate of weight loss as a function of temperature. The method is based on the following equation

$$\ln \frac{d\alpha}{dt} = \ln\{A(1-\alpha)^n\} - \frac{E}{RT} \qquad \text{Equation 5.3}$$

Using the above equation, the activation energy is obtained from the slope of a plot of natural logarithms of the rate of weight loss at different heating rates against reciprocal absolute temperature at a given weight loss. Activation energies obtained using the Friedman method follow the same trend obtained by using the cFWO method. Figure 5.13 shows the comparison of the Friedman method and cFWO method for the

degradation of PMMA and PMMA/ZHTMDBB-10 in nitrogen. The same trend was

observed for E_a values for the degradation under air as shown in Figure 5.14.
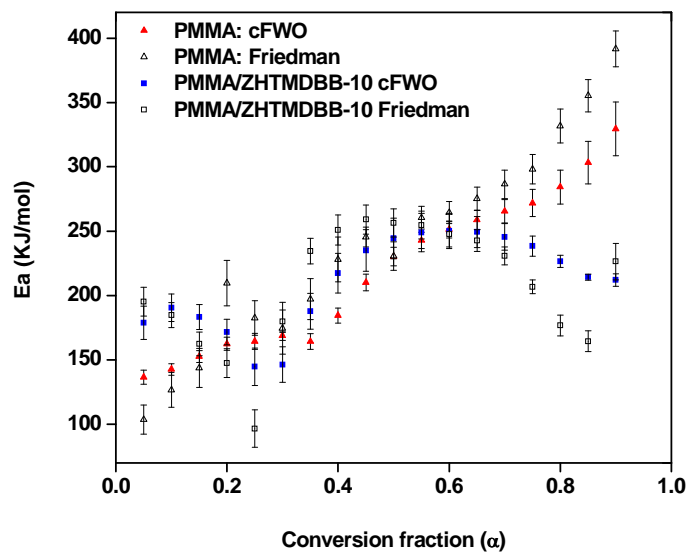
Figure 5.13: Comparison of corrected Flynn-Wall-Ozawa (cFWO) and Friedman methods for PMMA and PMMA/ZHTMDBB-10 degradation under nitrogen.
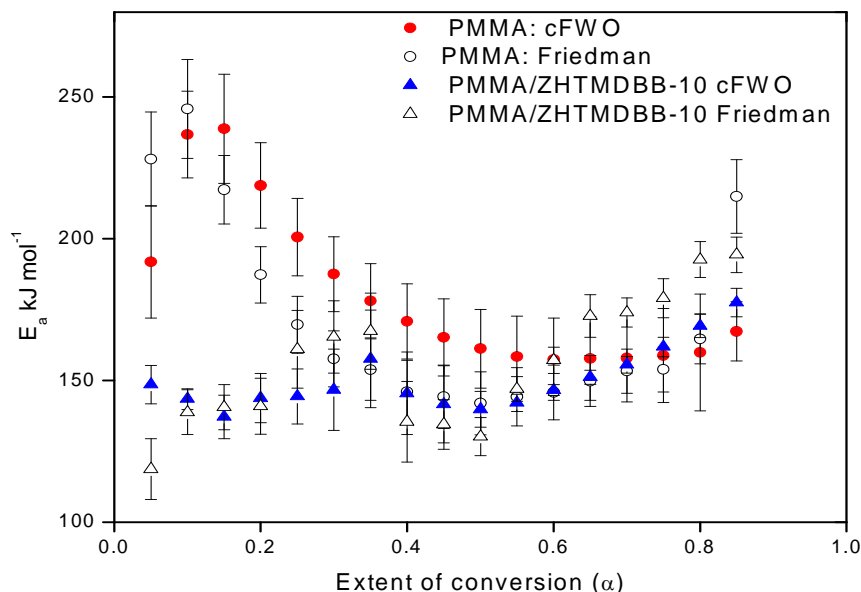
Figure 5.14: Comparison of corrected Flynn-Wall-Ozawa (cFWO) and Friedman methods for PMMA and PMMA/ZHTMDBB-10 degradation in air.

The third method used to determine the activation energy is the Kissinger method in which only the temperature at maximum rate of weight loss is required for computing E_a.[225] The E_a is calculated according to the following expression

$$\ln\left(\frac{\phi}{T_m^2}\right) = \ln(nRAW_m^{n-1}/E) - \frac{E}{R}\left(\frac{1}{T_m}\right)$$

Equation 5.4

in which Φ a is the heating rate, T_m is the temperature at the maximum rate of weight loss, R is the universal gas constant, E is the activation energy, A is the pre-exponential factor, W_m is the weight of the sample at the maximum rate of weight loss, and n is the apparent order of the reaction with respect to the sample weight. The E_a is obtained from the slope of a plot of $\ln(\frac{\Phi}{T_m^2})$ against $\frac{1}{T_m}$ at various heating rates. As can be seen from

Figure 5.8, the DTG for the first step of composites degraded in air exhibit a shoulder and it is difficult to accurately determine the exact temperature of maximum rate of degradation, as such it was not possible to calculate the activation energy for composites degraded in air. Table 5.3 gives a summary of the E_a values obtained from the Kissinger method. The results are consistent with results from the cFWO and Friedman methods in that the activation for the first step in the degradation of PMMA in nitrogen is lower as compared to that of the second step (180 kJ mol^{-1} for the first step and 274 kJ mol^{-1} for the second step). It is also noted that the activation energies of the composites are higher for the first step of degradation as compared to pure PMMA. The value obtained for the second degradation step of pure PMMA compares well with that obtained by Hirata *et al.*[212] who obtained 224 kJ mol^{-1}. Degradation of pure PMMA in air also show that the E_a for the two steps are not very different, which is consistent with what was obtained with the other methods.

Table 5.3: Summary of Ea values obtained from the Kissinger method

	E_a (kJ mol^{-1}) in nitrogen		E_a (kJ mol^{-1}) in air	
	First step	**Second step**	**First step**	**Second step**
Pure PMMA	180 ± 8	274 ± 6	138 ± 8	152 ± 4
PMMA/ZHTMDBB-10	225 ± 6	220 ± 13	-	-
PMMA/ZHTMDBB-3	212 ± 6	304 ± 18	-	-

Note: The composites degraded in air did not show a distinct first degradation peak so it was not possible to calculate the activation energies

It has also been noted that values of activation energies obtained for polymer degradation vary widely depending on molecular weight, sample thickness, polymerization conditions and sample weight used in the TGA analysis.[228;230] For the work reported here, sample size and morphology are expected to be most important. The influence of sample weight on the degradation of PMMA/ZHTMDBB-10 in nitrogen atmosphere was investigated using sample weights (w) ranging from 5 mg to 20 mg; the data were analyzed using cFWO method. Results shown in Figure 5.15 indicate that the activation energy is not significantly different at low w (5 mg and 11 mg), but the difference is significant when w is increased to 20 mg. The results suggests that for low sample weights (5-11 mg) the mechanism of degradation remains the same or diffusion of molecules (especially products of decomposition) is not effected and product (monomer) recombination is not significant. When w was increased to 20 mg, the E_a values obtained increased significantly, the increase being more pronounced during the second step of the degradation process which is due to random scission of the chain. This increase could be due to the large sample size affecting heat and/ or mass transfer. Comparable results were obtained by Carrasco and Pagès who analyzed the degradation of polystyrene using TGA sample weights ranging from 6.0-25.0 mg, they observed an increase of E_a from 128 kJ mol^{-1} to 161 kJ mol^{-1} when the sample weight was increased from 6 mg to 25 mg.[230]
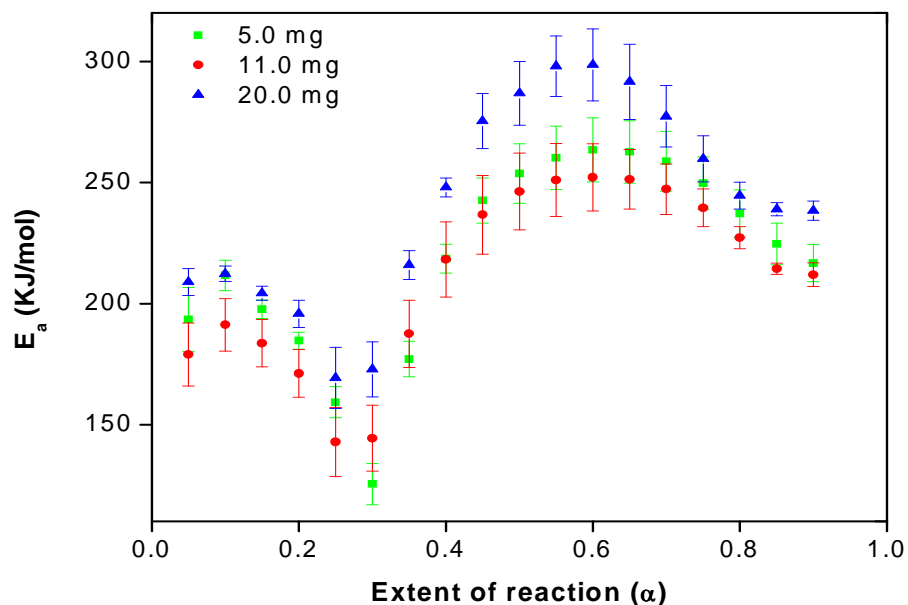
Figure 5.15: Effect of TGA sample weight on activation energy of PMMA/ZHTMDBB-10 degraded in nitrogen atmosphere.

5.3.4 Flammability properties

The effect of the additive on the flammability of PMMA was investigated by making use of cone calorimeter. The parameters obtained from the cone calorimeter which are relevant to the evaluation of additive as flame retardant include the heat release rate (HRR), peak of HRR (PHRR), total heat release (THR), smoke production (reported here as average specific extinction area, ASEA), and time to ignition, (t_{ig}). The ideal additive will result in the lowering of PHRR, THR, ASEA, and an increase in the time to ignition (t_{ig}). Figure 5.16 shows the variation of the heat release rate as a function of combustion time for pure PMMA, PMMA/ZHTMDBB-3, PMMA/ZHTMDBB-5, and

PMMA/ZHTMDBB-10 at a heat flux of 50kW/m^2. The heat flux of 50 kW/m^2 was chosen so as to simulate the radiant heat in a developing fire,[231] which enables assessment of fire retarding performance of the additive during the development of fire. The HRR curves for the composites are spread over a wider range as compared to pure PMMA indicating that the composites burn with less intensity but for a longer time. The integration of the area under the respective curves for each composite and pure PMMA gives the total heat release (THR). The additive did not significantly reduce the THR which means the additive did not affect the extent of PMMA burning, this has been reported by other workers[55] who used LDH additives. The summary of cone calorimetry data presented in table 5.4 shows that the additive resulted in a significant increase in the average smoke produced (ASEA). The amount of smoke produced increased as the level of loading increased, this could be due to the presence of benzene ring on the additive which has been shown to increase the amount of smoke produced.
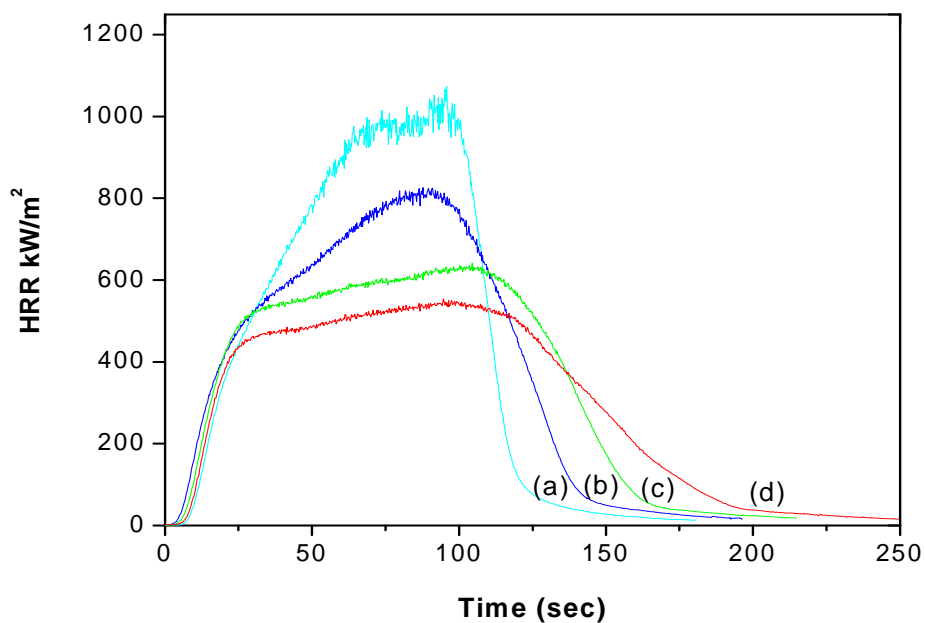
Figure 5.16: Heat release rate curves for (a) pure PMMA, (b) PMMA/ZHTMDBB-3 (c) PMMA/ZHTMDBB-5 (d) PMMA/ZHTMDBB -10 from cone calorimetry measurements at a heat flux of 50 kW/m².

Table 5.4: Summary of the cone calorimetry data

Sample	TSC	PHRR (kW/m²)	T_PHRR	THR (MJ/m²)	AMLR	ASEA
	(s)	(% red)	(s)	(% red)	(g/secm²)	(m²/kg)
Pure PMMA	10±2	1092±29	93±4	79.9±0.7	31±4	134±8
PMMA/ZHTMDBB-3	7±1	849±73 (22)	90±3	77.0±0.7 (3.7)	33±5	179±12
PMMA/ZHTMDBB-5	8±2	646±6 (41)	91±5	75.5±0.4 (5.0)	24±0	192±2
PMMA/ZHTMDBB-10	9±1	568±34 (48)	96±1	72.4±0.2 (10.0)	19±1	201±27

The important feature of Figure 5.16 and the summary of results presented in table 5.4 is the significant lowering of the peak heat release rate by up to 48% for PMMA/ZHTMDBB-10. The reduction of PHRR obtained here is comparable to values obtained for LDH systems[36;55;56] and this shows that the LHS system studied here is equally effective in reducing PHRR of PMMA as LDH systems. The lowering of the PHRR or increase in the limiting oxygen index has been shown to correspond with an increase in the production of char for condensed phase FR.[49;232] Work reported by Martín *et al.* and Armitage *et al.* have shown that incorporating boron into polymers lead to an increase in char production and a corresponding increase in the limiting oxygen index.[203;205;233] The combustion process of polymers involves heating the polymer using an external heat source resulting in the decomposition of the polymer. For PMMA the initial product of the decomposition is the monomer (MMA) and small amounts of other products such as propylene and acetone.[140;201] The MMA molecules then further decomposes producing volatile (combustible) compounds (methane, methanol, formaldehyde and acetylene) which then undergo oxidation, releasing heat which is then fed back to the bulk polymer causing further decomposition of the polymer thereby sustaining the flame even when the external heat source has been removed. For an additive to be effective as a fire retardant, it should be able to break the above cycle. This can be achieved in a variety of ways which include; (i) improvement of thermal stability of the polymer, (ii) dilution and subsequent quenching of the flame, and (iii) providing a barrier for heat and mass transfer.[48] ZHTMDBB might act by diluting and quenching the flame by generation of non combustible materials such as CO_2 and water from its

decomposition. In addition, the char produced during the burning process may act as a barrier to heat and mass transfer reducing the diffusion of combustible products of decomposition, or a combination of the two mechanisms. ZHTMDBB may also act by changing the degradation pathway of the polymer as indicated by the effects the additive had on the activation energy of degradation. Boron containing polymers have been shown to produce boric acid during thermal degradation,[207] the boric acid or oxides of boron may then react with zinc oxide, formed from the metal hydroxide layers, forming zinc borate.[208;234] XRD analysis of the char after cone calorimetry test shown in Figure 5.17 provides evidence for the formation of zinc borate. The XRD profile reveals the presence of ZnO phase (PDF # 36-1451) and zinc borate (ZnB_2O_6) phase (PDF # 27-983).[154] Since zinc borates have been shown to reduce the flammability of polymers by promoting char formation, its presence may have contributed to the reduction in PHRR observed here.[235] Since zinc borate was still present after the cone test, further studies are required to investigate the contribution of the lamella compound and zinc borate in reducing PHRR observed in this study.
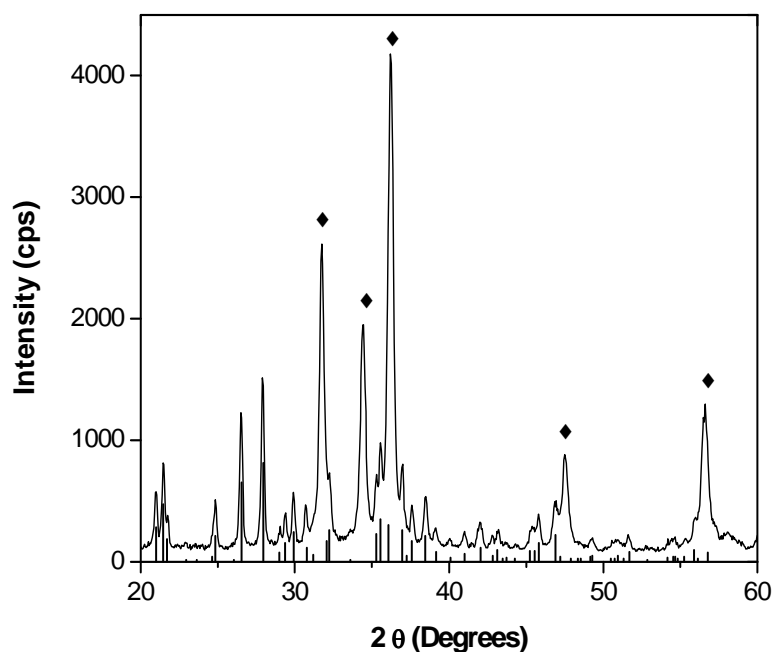
Figure 5.17: XRD profile of char residue after cone calorimetry test of PMMA/ZHTMDBB-10 revealing the presence of ZnO [PDF# 36-1451] marked with closed diamonds and stick spectrum provided for ZnB$_2$O$_6$ phase [PDF# 27-983].

The reduction in PHRR observed in this work can be attributed to char production with the char acting as a protective layer and a barrier to heat and mass transfer. The burning of pure PMMA is characterized by bubbling and cracking of the surface which enhances the transport of pyrolysis products to the surface thereby enhancing the degradation process.[140;232] With this in mind, the production of a continuous layer of char covering the whole surface should, in principle, lead to a much higher improvement in PHRR as well as other flammability measures such as the limiting oxygen index (LOI). A continuous barrier does not allow degradation products below the heated surface to be exposed to the fire during cone calorimetry test or external heat flux in the gasification

process. Kashiwagi *et al.* [232] showed that additives which cross-linked and formed a network char structure produced better improvements in flammability behavior than additives which formed aggregates and pillars. The morphology of the char formed when anionic clays are used varies with the metal constituents of the metal hydroxide layers, the intercalated anion and the polymer. In some instances char covering the whole surface can be obtained resulting in greater reduction in PHRR and sometimes small aggregates spread throughout the surface are observed.[35;236]

The charring process in this work exhibited significant pillaring. The initial char formed covered the surface of the polymer but as the degradation continued, cracks formed on the surface and bubbles from underneath the surface escaped. The movement of these bubbles results in the coagulation of the char, forming discrete pillars which grew as the burning progressed. The pillars can be observed in Figure 5.18. The coagulation of the char into pillars may be the results of the poor dispersion of the LHS in the polymer, as indicated by TEM images discussed previously.

PMMA/ZHTMDBB-10

PMMA/ZHTMDBB-5

PMMA/ZHTMDBB-3

Figure 5.18: Char of PMMA composites after cone calorimetry test

The pillars obtained in this work had two distinct regions: the top part which was white/light gray in color and the lower part which was black. Samples from these two regions showed the following elemental compositions; white part: 71.81% Zn, 0.35% C, 13.65% O, 3.25% B, < 0.05% N, < 0,05% H. The mole ratio of Zn:B for the white part was found to be 3.6:1 and that of Zn:C was 37.7:1. For the black, lower part of the pillar elemental analysis determined a relative composition of: 70.99% Zn, 0.47% C, 14.72% O, 3.01% B, < 0.05% N, < 0,05% H. The mole ratio of Zn:B for the lower part was found

to be 3.9:1 and that of Zn:C was 27.7:1. These results indicate that carbonaceous char was formed at the lower part of the pillar. When the material started to decompose the char started to form pillars as explained above, as the char limited heat and matter (air) transfer carbonaceous particles began to form underneath the char (also becoming part of the char) resulting in the black part of the char. The stacking of the char can be clearly seen in Figure 5.18 which shows that the amount of char, size of the char pillars and the surface coverage of the aluminum foil holder increased with the loading of the additive. The cracking of the char and formation of char pillars exposed the polymer and its degradation products to the fire during the burning process and this resulted in the char not providing sufficient protection to effectively reduce the burning of the polymer. The char in this case served to slow the flow of combustibles thereby reducing flame intensity as shown by the reduction in PHRR; however the amount of polymeric material which is combusted was not significantly affected as evidenced by the small reduction in THR observed (Table 5.4).

5.4   Conclusions

The ZHTMDBB layered additive exhibited some intercalation by PMMA when melt blended, with poorly dispersed additive tactoids observed in TEM images. The thermal stability, degradation kinetics and fire properties of PMMA and its composites with ZHTMDBB have been studied by TGA and cone calorimetry. TGA results showed that there was significant increment in T_{10} and T_{50} for all the composites as compared to the pristine PMMA in both air and nitrogen and the additive has more stabilizing effect in

air as compared to nitrogen and this has practical benefits in that fires occurs in an oxygen environment. The degradation kinetics of PMMA and the composites showed that the additives increased the activation energies for the first step in the degradation; the activation energies of the second step in air were not significantly affected but in nitrogen the E_a was reduced at higher conversion. The activation energy for the degradation in air is lower than in nitrogen for the second step but for the first step the activation energies were not significantly different. All three methods used in this study were in agreement. The additive significantly reduced the peak heat release rate (PHRR) of PMMA, despite pillaring of the char. Similar to most LDHs, it did not reduce THR. Further optimization is necessary to decrease smoke production.

Chapter 6 :   Proposed future work

6.1   Effect of Guest Anions on Anion exchange Kinetics

In section 3.4 we observed that the release of *o*-HCn from C-*o*-HCn depends on the nature and size of the guest anions. We only investigated the effects of three anions namely chloride, bromide and formate. For a more comprehensive study we need to extent the investigation to other anions including the other members of the halogen series, (fluoride and iodine). Divalent anions such as carbonate will provide another dimension for comparison; they have a higher charge density which may result in complete exchange for all the systems. The release reactions in section 3.4 were carried out at a single temperature, 40^oC. It would be informative to study the temperature dependence and evaluate the Arrhenius parameters in order to gain more insight into the differences due to guest anions. Isoconversional analysis would be most useful as we will be able to determine whether the reactions occur via a single mechanism as in the Cl^- exchange or the mechanism changes as the reaction proceeds. The exchange using bromide anions has been carried out at three temperatures as shown in 6.1, and the reaction show temperature dependence. Two more temperatures are required in order to obtain more reliable Arrhenius parameters.
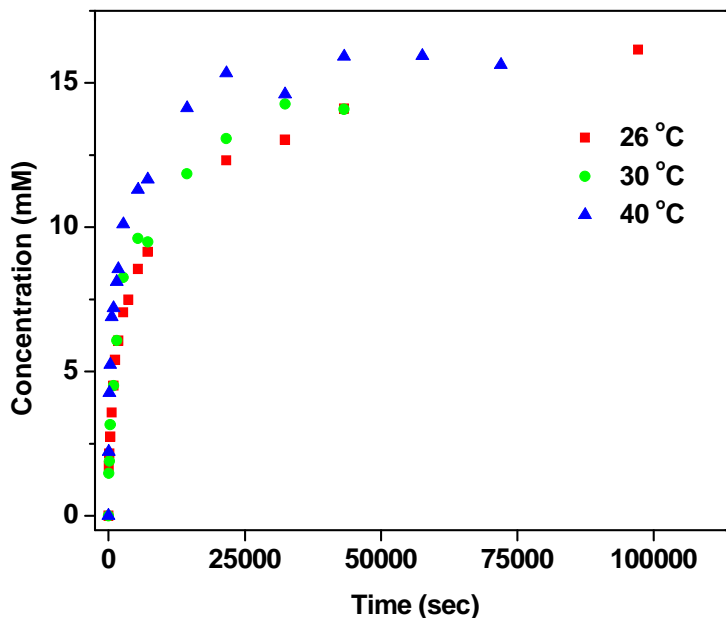
Figure 6.1: Plot of concentration as a function of time (seconds) for the release of o-HCn using Br⁻ at 26°C, 30°C and 40°C.

6.2   Effect of metal hydroxide layer on anion exchange kinetics.

The studies in chapter 3 and 4 have included the release of *o*-HCn from layered

metal hydroxide with different metal ion compositions, namely copper based (C-*o*-HCn,

chapter 3) and zinc copper based (ZC-*o*-HCn, chapter 4). We have observed some

intriguing results in these systems; while the release from ZC-*o*-HCn was complete and

the profile sigmoidal (section 4.3.2), the release from C-*o*-HCn was incomplete and the

profile was deceleratory (section 3.3.2.1). The release rates were also significantly

different, with rate constants being $(4.3 \pm 0.7) \times 10^{-4}$ s^{-1} and $(2.9 \pm 0.05) \times 10^{-4}$ s^{-1} for C-*o*-

HCn and ZC-*o*-HCn respectively. We need to extent this investigation to other metal hydroxides composed of a variety of metal ions. The layered metal hydroxides may include HDSs and LHSs based on the following; zinc-cobalt, cobalt, zinc-nickel, and nickel ions. Since the ortho isomer exhibited the greatest extent of reaction (chapter 4), we will use this isomer for the metal hydroxide composition effect. Preparatory work on zinc,acetate LHS has indicated that the exchange was complete but the product is biphasic as shown in Figure 6.5. Work still needs to be done in order to obtain a single *o*-HCn phase.
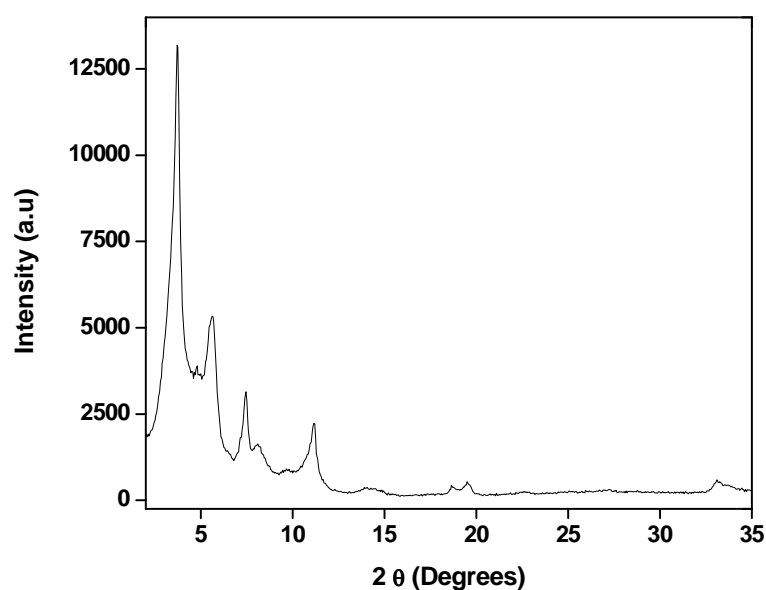
Figure 6.2: ZH-*o*-HCn obtained from zinc hydroxy acetate

6.3   Effect of Host anion structure

Understanding the effects of functional and substituent groups, hydrogen bonding and chain length on anion release will enable tuning of layered metal hydroxides for controlled release delivery. In chapter 4 we observed that the position of hydroxyl groups had an effect on hydrogen bonding network which resulted in significant differences in the kinetics of anion release, with dipole moments influencing the extent of release. To be able to tune controlled release delivery it is important to extend the study to other substituent groups on the kinetics of anion exchange reactions. Some of the anions proposed for this study are shown in Figure 6.3. The nitro isomers would be most interesting because, in addition to being capable of hydrogen bonding, the $-NO_2^-$ group is electron withdrawing as compared to the other groups which reverses the dipole moments.

(a)   chlorocinnamates   (b)   Aminocinnamates   (c)   Nitrocinnamates
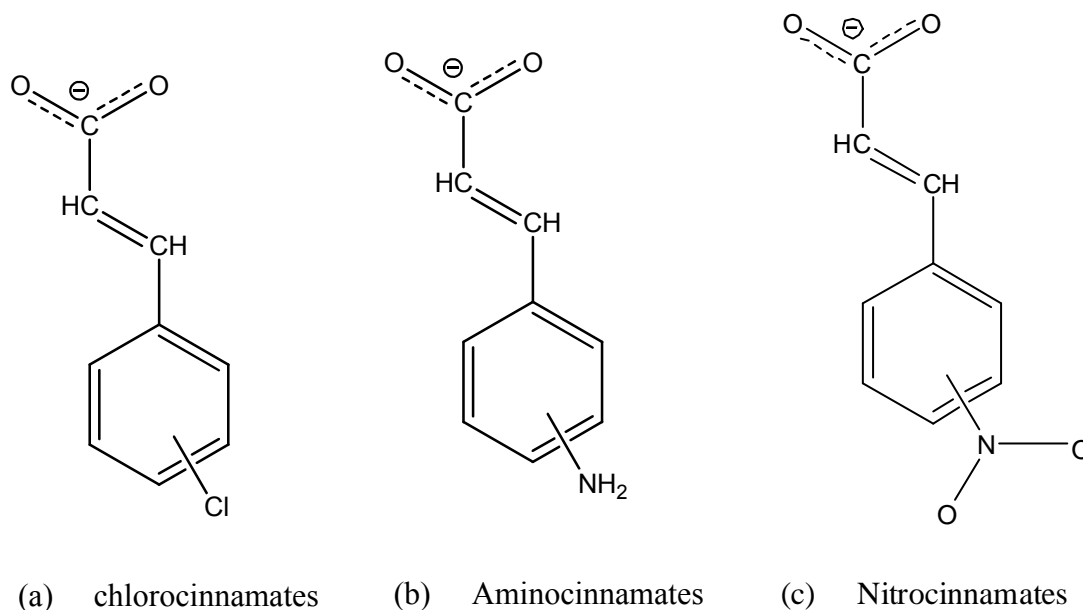
Figure 6.3: Substituted cinnamates as model compounds for anions release kinetics

Comparing these effects of substituent groups would provide more insight into the effects of secondary bonding networks in stabilization and retention of the anions in the interlayer. Preliminary results in intercalation of chlorocinnamates in zinc,copper HDS have indicated that the para isomer can be intercalated as a single phase while the ortho and meta isomer intercalates are biphasic as shown in Figure 6.4. Thus more work is needed to obtain single phases of the ortho and meta isomer intercalates.
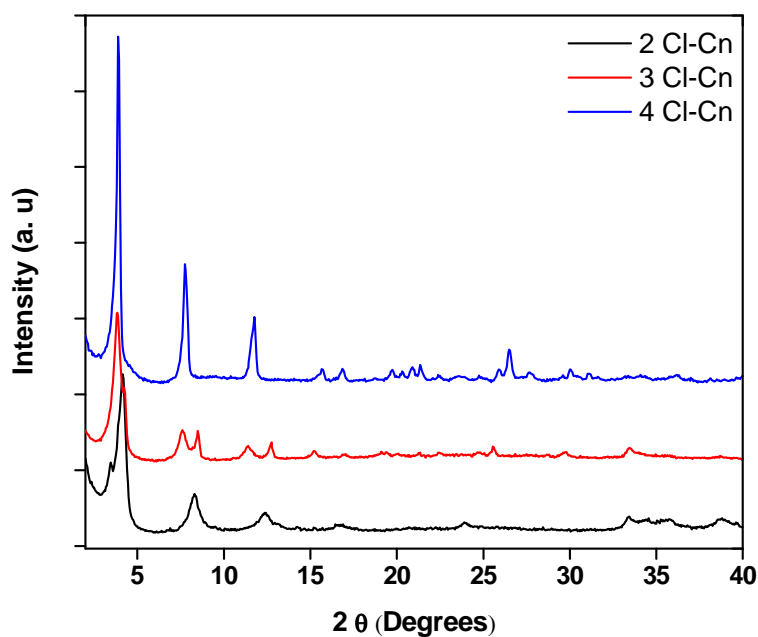
Figure 6.4: PXRD profiles of zinc copper based HDSs intercalated with isomers of chlorocinnamate

Even though the ortho and meta isomer compounds where biphasic, during exchange with chloride anions, the ortho isomer exchanged completely while the para and meta intercalates exchanged to a very low extent. This is shown in Figure 6.5 where

there are no reflections from *o*-ClCn in the exchange product (Figure 6.5 b) while reflections from meta and para chlorocinnamates are still the major reflections in Figure 6.5 a and c respectively.
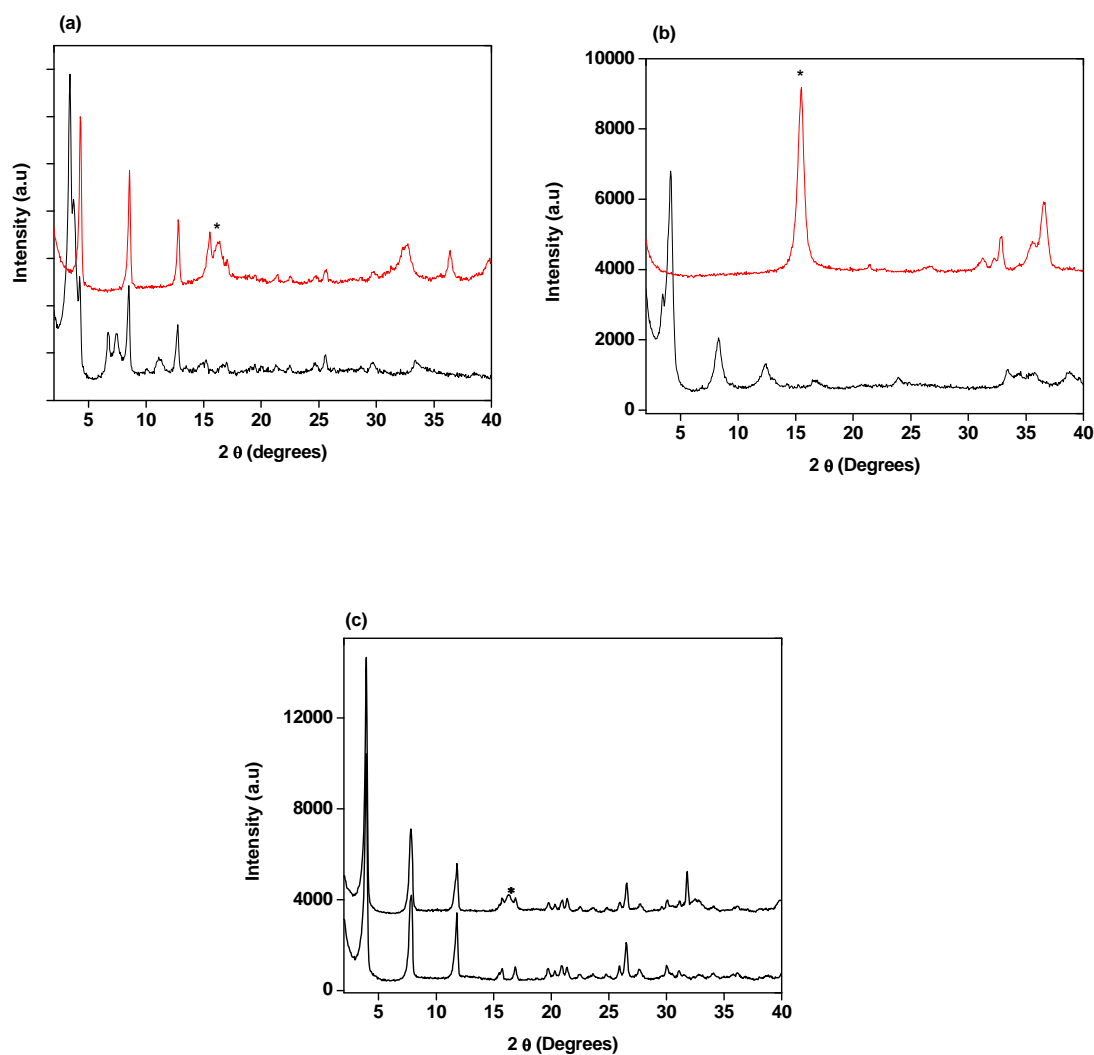
Figure 6.5: Chlorocinamate intercalates and their chloride exchange products. (a) ZC-*m*-ClCn, (b) ZC-*o*-ClCn and (c) ZC-*p*-ClCn

Initial release reactions have been conducted for ZC-*p*-ClCn using chloride ion as the exchange anion. Although the extent of release was low, the kinetics of release was slow which allowed us to obtain measurable kinetics without data scatter. There was a

large induction period of close to 3 hours observed in both XRD and UV-Vis analysis as shown in Figure 6.6 a and b respectively. From XRD it can be observed that there was a dramatic change in the crystallinity of the materials at the onset of the exchange process as observed in the basal reflections which became sharper and increased in intensity. This is an indication of a chemical transformation which results in the increase of the crystallite size.
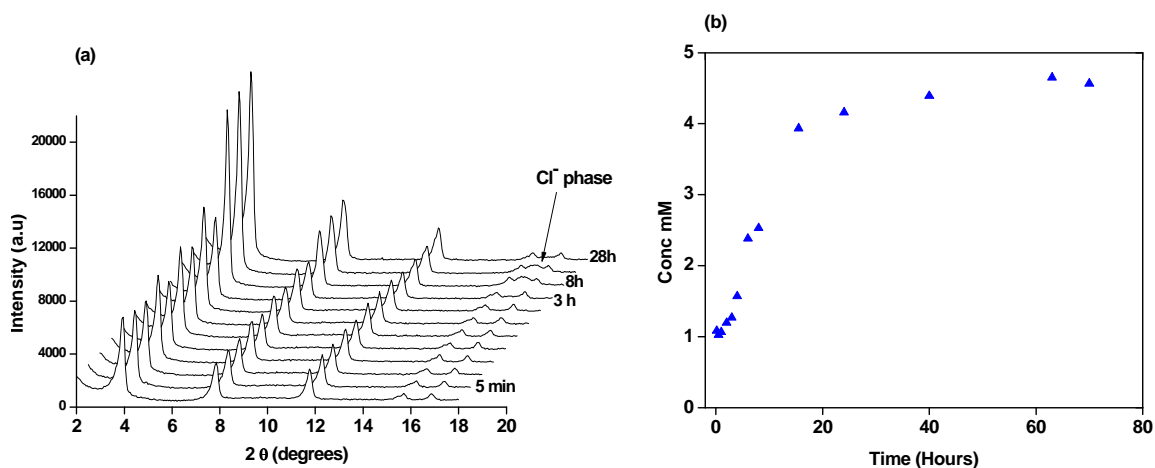
Figure 6.6: PXRD (a) and release profile (b) of p-ClCn obtained at 40°C using 1 M chloride solution

It would be interesting to study the temperature dependence of the release and also the effects of the position of the Cl group on the release behavior. The first step would be to cleanly obtain intercalates of the ortho and meta isomers by varying preparation conditions.

6.4   Competitive uptake

The study of the competitive uptake of the isomers will give an indication of the selectivity of the precursor LHS (ZC-Ac); the results may provide vital information to explain the differences in the obtained anion release kinetic parameters. Preliminary work in CHN has shown that in a 50:50 mixture of *o*-HCn and *p*-HCn, *p*-HCn is preferentially intercalated. The results though need to be treated with caution as PXRD which was used to deduce this preferential intercalation is inconclusive. Absence of reflections from *o*-HCn was taken as an indication that there was no intercalation of the isomer, more accurate methods will be used to be able, not only to give a qualitative solution, but also quantitative results of the relative amounts of each isomer intercalated. One possibility will be to carry out the competitive intercalation reaction and then completely exchange out the isomers. Isomer specific analytical techniques will be used to qualitatively and quantitatively analyze the isomer mixture. The limitation of such a procedure though, is that the secondary exchange should be complete so as to determine the exact amounts of molecules originally intercalated. Ragavan *et al.* used ^{1}H NMR to study the selective intercalation of chlorophenoxyacetates, but separation methods such as HPLC can be very useful in this study.

BIBLIOGRAPHY

1. Ikeda, T.; Amoh, H.; Yasunaga, T. *J. Am. Chem. Soc.* **1984**, *106*, 5772-5775.

2. Miyata, S.; Kumura Teruhiko. *Chem. Lett.* **1973**, 843-848.

3. Miyata, S. *Clays Clay Miner.* **1983**, *31*, 305-311.

4. Morioka, H.; Tagaya, H.; Karasu, M.; Kadokawa, J.; Chiba, K. *J. Mater. Res.* **1998**, *13*, 848-851.

5. Yamanaka, S.; Sako, T.; Hattori, M. *Chem. Lett.* **1989**, 1869-1872.

6. Meyn, M.; Beneke, K.; Lagaly, G. *Inorg. Chem.* **1993**, *32*, 1209-1215.

7. Taylor H.F.W. *Mineral. Mag.* **1973**, *39*, 377-389.

8. Drits V.A; Bookin S.A. *Layered double hydroxide*; Nova Science Publishers, Inc: New York, 2001; Chapter 2, pp. 41-99.

9. Kalinichev, A. G.; Kumar, P. P.; Kirkpatrick, R. J. *Philos. Mag.* **2010**, *90*, 2475-2488.

10. Kovar, P.; Pospisil, M.; Nocchetti, M.; Capkova, P.; Melanova, K. *J Mol Model.* **2007**, *13*, 937-942.

11. Hou, X. Q.; Kirkpatrick, R. J. *Chem. Mater.* **2002**, *14*, 1195-1200.

12. Hou, X. Q.; Kalinichev, A. G.; Kirkpatrick, R. J. *Chem. Mater.* **2002**, *14*, 2078-2085.

13. Allmann, R. *Acta Crystallogr., Sect. B: Struct. Sci.* **1968**, *24*, 972-977.

14. Bish, D. L.; Brindley, G. W. *Am. Mineral.* **1977**, *62*, 458-464.

15. Jambor, J. L.; Dutrizac, J. E.; Roberts, A. C.; Grice, J. D.; Szymanski, J. T. *Can. Mineral.* **1996**, *34*, 61-72.

16. Brindley, G. W.; Kikkawa, S. *Am. Mineral.* **1979**, *64*, 836-843.

17. Carrado, K. A.; Kostapapas, A.; Suib, S. L. *Solid State Ionics* **2002**, *26*, 77-86.

18. Marcelin, G.; Stockhausen, N. J.; Post, J. F. M.; Schutz, A. *J. Phys. Chem.* **1989**, *93*, 4646-4650.

19. Frondel C. *Am. Mineral.* **1941**, *26*, 295-315.

20. Wang, J.; Kalinichev, A. G.; Kirkpatrick, R. J.; Hou, X. *Chem. Mater.* **2000**, *13*, 145-150.

21. Padma Kumar, P.; Kalinichev, A. G.; Kirkpatrick, R. J. *J. Phys. Chem. B*. **2006**, *110*, 3841-3844.

22. Barriga, C.; Gaitan, M.; Pavlovic, I.; Ulibarri, M. A.; Hermosin, M. C.; Cornejo, J. *J.Mater.Chem.* **2002**, *12*, 1027-1034.

23. Chouillet, C.; Krafft, J. M.; Louis, C.; Lauron-Pernot, H. *Spectrochim. Acta, Part A.* **2004**, *60*, 505-511.

24. Morioka, H.; Tagaya, H.; Karasu, M.; Kadokawa, J.; Chiba, K. *Inorg. Chem.* **1999**, *38*, 4211-4216.

25. Rajamathi, J. T.; Britto, S.; Rajamathi, M. *J. Chem. Sci.* **2005**, *117*, 629-633.

26. Bozorth, R. M. *J. Am. Chem. Soc.* **1922**, *44*, 2232-2236.

27. Stahlin, W.; Oswald, H. R. *Acta Crystallogr., Sect. B: Struct. Sci.* **1970**, *26*, 860-863.

28. Choy, J. H.; Kwon, Y. M.; Han, K. S.; Song, S. W.; Chang, S. H. *Mater. Lett.* **1998**, *34*, 356-363.

29. Fujita, W.; Awaga, K.; Yokoyama, T. *Inorg. Chem.* **1997**, *36*, 196-199.

30. Jimenez-Lopez, A.; Rodriguez-Castellon, E.; Olivera-Pastor, P.; Maireles-Torres, P.; Tomlinson, A. A. G.; Jones, D. J.; Roziere, J. *J.Mater.Chem.* **1993**, *3*, 303-307.

31. Rojas, R.; Barriga, C.; Angeles Ulibarri, M.; Malet, P.; Rives, V. *J.Mater.Chem.* **2002**, *12*, 1071-1078.

32. Choy, J. H.; Kwon, Y. M.; Song, S. W.; Chang, S. H. *Bull. Korean Chem. Soc.* **1997**, *18*, 450-453.

33. Bovio, B.; Locchi, S. *J Cryst Spectrosc.* **1982**, *12*, 507-517.

34. Zhang, J.; Wang, X. Y.; Zhang, F.; Horrocks, A. R. *Polym. Test.* **2004**, *23*, 225-230.

35. Manzi-Nshuti, C.; Wang, D. Y.; Hossenlopp, J. M.; Wilkie, C. A. *J.Mater.Chem.* **2008**, *18*, 3091-3102.

36. Manzi-Nshuti, C.; Songtipya, P.; Manias, E.; Jimenez-Gasco, M. M.; Hossenlopp, J. M.; Wilkie, C. A. *Polymer* **2009**, *50*, 3564-3574.

37. Nyambo, C.; Kandare, E.; Wang, D.; Wilkie, C. A. *Polym Degrad Stab* **2008**, *93*, 1656-1663.

38. Kandare, E.; Deng, H. M.; Wang, D. Y.; Hossenlopp, J. M. *Polym. Adv. Technol.* **2006**, *17*, 312-319.

39. Kandare, E.; Chigwada, G.; Wang, D.; Wilkie, C. A.; Hossenlopp, J. M. *Polym Degrad Stab* **2006**, *91*, 1209-1218.

40. Kandare, E.; Chigwada, G.; Wang, D.; Wilkie, C. A.; Hossenlopp, J. M. *Polym Degrad Stab* **2006**, *91*, 1781-1790.

41. Majoni, S.; Su, S.; Hossenlopp, J. M. *Polym Degrad Stab* **2010**, *95*, 1593-1604.

42. Hornsby, P. R.; Cusack, P. A.; Cross, M.; Toth, A.; Zelei, B.; Marosi, G. *J. Chem. Sci.* **2003**, *38*, 2893-2899.

43. Wilkie C. A. *Fire Retardancy of Polymers*; Royal Society of Chemistry: Cambridge, 2005; Chapter 1, pp. 1-18.

44. Babrauskas, V. *Fire Mater.* **1984**, *8*, 81-95.

45. Gilman, J. W.; Kashiwagi, T.; Lichtenhan, J. D. *Sampe J.* **1997**, *33*, 40-46.

46. Chigwada, G.; Jiang, D. D.; Wilkie, C. A. *Fire and Polymers Iv: Materials and Concepts for Hazard Prevention* **2006**, *922*, 103-116.

47. Costache, M. C.; Heidecker, M. J.; Manias, E.; Gupta, R. K.; Wilkie, C. A. *Polym Degrad Stab.* **2007**, *92*, 1753-1762.

48. Chigwada, G; Kandare, E; Wang, D; Majoni, S; Mlambo, D; Wilkie, C.A; Hossenlopp, J.M. *J. Nanosci. Nanotechnol.* **2008**, *8*, 1927-1936.

49. Kashiwagi, T.; Harris, R. H.; Zhang, X.; Briber, R. M.; Cipriano, B. H.; Raghavan, S. R.; Awad, W. H.; Shields, J. R. *Polymer* **2004**, *45*, 881-891.

50. Laachachi, A.; Ruch, D.; Addiego, F.; Ferriol, M.; Cochez, M.; Lopez Cuesta, J. M. *Polym Degrad Stab.* **2009**, *94*, 670-678.

51. Tyan, H. L.; Leu, C. M.; Wei, K. H. *Chem. Mater.* **2001**, *13*, 222-226.

52. Wang, L. J.; Xie, X. L.; Su, S. P.; Feng, J. X.; Wilkie, C. A. *Polym Degrad Stab.* **2010**, *95*, 572-578.

53. Zhang, J.; Wilkie, C. A. *Polym Degrad Stab.* **2003**, *80*, 163-169.

54. Costa, F. R.; Wagenknecht, U.; Heinrich, G. *Polym Degrad Stab.* **2007**, *92*, 1813-1823.

55. Manzi-Nshuti, C.; Hossenlopp, J. M.; Wilkie, C. A. *Polym Degrad Stab.* **2008**, *93*, 1855-1863.

56. Nyambo, C.; Wang, D.; Wilkie, C. A. *Polym. Adv. Technol.* **2008**, *20*, 332-340.

57. Nyambo, C.; Kandare, E.; Wilkie, C. A. *Polym Degrad Stab.* **2009**, *94*, 513-520.

58. Wang, G. A.; Wang, C. C.; Chen, C. Y. *Polym Degrad Stab.* **2006**, *91*, 2443-2450.

59. Wang, L. J.; Su, S. P.; Chen, D.; Wilkie, C. A. *Polym Degrad Stab.* **2009**, *94*, 1110-1118.

60. bin Hussein, M. Z.; Zainal, Z.; Yahaya, A. H.; Foo, D. W. V. *J. Controlled Release* **2002**, *82*, 417-427.

61. Bringley, J. F.; Liebert, N. B. *J. Dispersion Sci. Technol.* **2003**, *24*, 589-605.

62. Gu, Z.; Thomas, A. C.; Xu, Z. P.; Campbell, J. H.; Lu, G. Q. *Chem. Mater.* **2008**, *20*, 3715-3722.

63. Panda, H. S.; Srivastava, R.; Bahadur, D. *J.Phys.Chem. B* **2009**, *113*, 15090-15100.

64. Wei, M.; Guo, J.; Shi, Z. Y.; Yuan, Q.; Pu, M.; Rao, G. Y.; Duan, X. *J. Chem. Sci.* **2007**, *42*, 2684-2689.

65. Zaemah bt Jubri. *The Malaysian Journal of Analytical Sciences* **2008**.

66. Khan, A. I.; Lei, L. X.; Norquist, A. J.; O'Hare, D. *Chem. Commun.* **2001**, 2342-2343.

67. Khan, A. I.; Ragavan, A.; Fong, B.; Markland, C.; O'Brien, M.; Dunbar, T. G.; Williams, G. R.; O'Hare, D. *Ind. Eng. Chem. Res.* **2009**, *48*, 10196-10205.

68. Raki, L.; Beaudoin, J. J.; Mitchell, L. *Cem. Concr. Res.* **2004**, *34*, 1717-1724.

69. Fogg, A. M.; Dunn, J. S.; Shyu, S. G.; Cary, D. R.; O'Hare, D. *Chem. Mater.* **1998**, *10*, 351-355.

70. Kooli, F.; Chisem, I. C.; Vucelic, M.; Jones, W. *Chem. Mater.* **1996**, *8*, 1969-1977.

71. Lei, L.; Vijayan, R. P.; O'Hare, D. *J.Mater.Chem.* **2001**, *11*, 3276-3280.

72. Lei, L. X.; Khan, A.; O'Hare, D. *J. Solid State Chem.* **2005**, *178*, 3648-3654.

73. Lotsch, B.; Millange, F.; Walton, R. I.; O'Hare, D. *Solid State Sci.* **2001**, *3*, 883-886.

74. Tagaya, H.; Sasaki, N.; Morioka, H.; Kadokawa, J. *Mol. Cryst. Liq. Cryst.* **2000**, *341*, 1217-1222.

75. Ragavan, A.; Khan, A.; O'Hare, D. *J.Mater.Chem.* **2006**, *16*, 4155-4159.

76. Jin, S.; Fallgren, P. H.; Morris, J. M.; Chen, Q. *Sci. Adv. Mater.* **2001**, *8*, 67-70.

77. Vance, G. F.; Sparks, D. L.; Zhuang, J.; Jin, Y. *J.Environ.Qual.* **2003**, *32*, 2046-2053.

78. Inacio, J.; Taviot-Gueho, C.; Forano, C.; Besse, J. P. *Appl. Clay Sci.* **2001**, *18*, 255-264.

79. Lim, T. T.; Goh, K. H.; Goei, R.; Dong, Z. L. *Water Sci. Technol.* **2009**, *59*, 1011-1017.

80. Liu, Y. T.; Chen, T. Y.; Wang, M. K.; Huang, P. M.; Chiang, P. N.; Lee, J. F. *Appl. Clay Sci.* **2010**, *48*, 485-491.

81. Lv, L.; He, J.; Wei, M.; Evans, D. G.; Zhou, Z. L. *Water Res.* **2007**, *41*, 1534-1542.

82. Mantilla, A.; Tzompantzi, F.; Fernandez, J. L.; Gongora, J. A. I. D.; Mendoza, G.; Gomez, R. *Catal Today.* **2009**, *148*, 119-123.

83. Barrabes, N.; Cornado, D.; Foettinger, K.; Dafinov, A.; Llorca, J.; Medina, F.; Rupprechter, G. *J. Catal.* **2009**, *263*, 239-246.

84. Choudary, B. M.; Lakshmi Kantam, M.; Kavita, B.; Venkat Reddy, C.; Figueras, F. *Tetrahedron* **2000**, *56*, 9357-9364.

85. Ruiz, J. R.; Jimqnez-Sanchidribn, C.; Mora, M. *Tetrahedron* **2006**, *62*, 2922-2926.

86. Xi, Y.; Davis, R. J. *J. Catal.* **2008**, *254*, 190-197.

87. Dutta, P. K.; Puri, M. *J.Mater.Chem.* **1989**, *93*, 376-381.

88. Fujita, W.; Awaga, K. *Inorg. Chem.* **1996**, *35*, 1915-1917.

89. Hayashi, H.; Hudson, M. J. *J.Mater.Chem.* **1995**, *5*, 781-783.

90. Taibi, M.; Ammar, S.; Jouini, N.; Fievet, F.; Molinie, P.; Drillon, M. *J.Mater.Chem.* **2002**, *12*, 3238-3244.

91. Poznyak, S. K.; Tedim, J.; Rodrigues, L. M.; Salak, A. N.; Zheludkevich, M. L.; Dick, L. F. P.; Ferreira, M. G. S. *ACS Appl. Mater. Interfaces* **2009**, *1*, 2353-2362.

92. Wong, F.; Buchheit, R. G. *Prog. Org. Coat.* **2004**, *51*, 91-102.

93. Williams, G. R.; O'Hare, D. *J.Mater.Chem.* **2006**, *16*, 3065-3074.

94. Schildermans, I.; Mullens, J.; Vanderveken, B. J.; Yperman, J.; Franco, D.; Vanpoucke, L. C. *Thermochim. Acta* **1993**, *224*, 227-232.

95. Iyi, N.; Matsumoto, T.; Kaneko, Y.; Kitamura, K. *Chem. Lett.* **2004**, *33*, 1122-1123.

96. Costantino, U.; Marmottini, F.; Nocchetti, M.; Vivani, R. *Eur.J.Inorg.Chem.* **1998**, *1998*, 1439-1446.

97. Ogawa, M.; Kaiho, H. *Langmuir* **2002**, *18*, 4240-4242.

98. Poul, L.; Jouini, N.; Fievet, F. *Chem. Mater.* **2000**, *12*, 3123-3132.

99. Prevot, V.; Forano, C.; Besse, J. P. *Chem. Mater.* **2005**, *17*, 6695-6701.

100. McIntyre, L. J.; Jackson, L. K.; Fogg, A. M. *J. Phys. Chem. Solids* **2005**, *69*, 1070-1074.

101. Nayak, M.; Kutty, R. N.; Jayaraman, V.; Periaswamy, G. *J.Mater.Chem.* **1997**, *7*, 2131-2137.

102. Ogawa, M.; Asai, S. *Chem. Mater.* **2000**, *12*, 3253-3255.

103. Zhang, H.; Li, H.; Guo, Y.; Li, G.; Fan, C.; Wang, K.; Chen, J. *Particuology* **2010**, *8*, 192-197.

104. Fogg, A. M.; O'Hare, D. *Chem. Mater.* **1999**, *11*, 1771-1775.

105. Marchi, A. J.; Apestegua, C. R. *Appl. Clay Sci.* **1998**, *13*, 35-48.

106. Misra, C.; Perrotta, A. J. *Clays Clay Miner.* **1992**, *40*, 145-150.

107. Rocha, J.; del Arco, M.; Rives, V.; Ulibarri, A. *J.Mater.Chem.* **1999**, *9*, 2499-2503.

108. Vyazovkin, S.; Sbirrazzuoli, N. *Macromolecules* **1996**, *29*, 1867-1873.

109. Avrami, M. *J. Chem. Phys.* **1939**, *7*, 1103-1112.

110. Avrami, M. *J. Chem. Phys.* **1940**, *8*, 212-224.

111. Vyazovkin, S. *Int. Rev. Phys. Chem.* **2000**, *19*, 45-60.

112. Sharp, J.H; Brindley, G.W; Achar, B.N.N. *J. Am. Ceram. Soc.* **1966**, *49*, 379-382.

113. Vyazovkin, S.; Wight, C. A. *Int. Rev. Phys. Chem.* **1998**, *17*, 407-433.

114. Hancock, J.D; Sharp, J.H. *J. Am. Ceram. Soc.* **1972**, *55*, 74-77.

115. Francis, R. J.; O'Brien, S.; Fogg, A. M.; Halasyamani, P. S.; O'Hare, D.; Loiseau, T.; Ferey, G. *J. Am. Chem. Soc.* **1999**, *121*, 1002-1015.

116. Kandare, E.; Hossenlopp, J. M. *J.Phys.Chem. B* **2005**, *109*, 8469-8475.

117. Young D.A *Decomposition of solids*, Pergamon Press Ltd: Oxford, 1966.

118. Saitoh, H.; Machida, A.; Katayama, Y.; Aoki, K. *Appl. Phys. Lett.* **2009**, *94*.

119. Sperling L.H. *Introduction to Physical Polymer Science*; 4 ed.; John Wiley & Sons: New Jersey, 2006; Chapter 6, pp. 239-323.

120. Fogg, A. M.; Dunn, J. S.; O'Hare, D. *Chem. Mater.* **1998**, *10*, 356-360.

121. Hussein, M. Z. b.; Yahaya, A. H.; Zainal, Z.; Kian, L. H. *Science and Technology of Advanced Materials* **2005**, *6*, 956-962.

122. Khan, A. I.; O'Hare, D. *J.Mater.Chem.* **2002**, *12*, 3191-3198.

123. Williams, G. R.; Norquist, A. J.; O'Hare, D. *Chem. Mater.* **2004**, *16*, 975-981.

124. Vyazovkin, S.; Wight, C. A. *Annu. Rev. Phys. Chem.* **1997**, *48*, 125-149.

125. Vyazovkin, S. V.; Lesnikovich, A. I. *Thermochim. Acta* **1990**, *165*, 11-15.

126. Vyazovkin, S.; Wight, C. A. *Thermochim. Acta* **1999**, *340-341*, 53-68.

127. Vyazovkin, S. *Int.J.Chem.Kinet.* **2002**, *34*, 418-420.

128. Flynn, J. H.; Wall, L. A. *J. Res. Nat. Bur. Stand.* 1966, *70*, 487.

129. Vyazovkin S. *Handbook of Thermal Analysis and Calorimetry*; Elsevier: Amsterdam, 2008; Chapter 13, pp. 503-538.

130. Vyazovkin, S.; Goryachko, V.; Bogdanova, V.; Guslev, V. *Thermochim. Acta* **1993**, *215*, 325-328.

131. Budrugeac, P.; Homentcovschi, D.; Segal, E. *J. Therm. Anal. Calorim.* **2001**, *63*, 457-463.

132. Popescu, C.; Segal, E. *Int.J.Chem.Kinet.* **1998**, *30*, 313-327.

133. Quaas, M.; Wulff, H.; Ivanova, O.; Helm, C. A. *Z. Kristallogr.* **2009**, 241-246.

134. Ambrogi, V.; Fardella, G.; Grandolini, G.; Perioli, L.; Tiralti, M. C. *aaps pharmscitech* **2003**, *3*, 1-6.

135. Yang, J. H.; Han, Y. S.; Park, M.; Park, T.; Hwang, S. J.; Choy, J. H. *Chem. Mater.* **2007**, *19*, 2679-2685.

136. Millange, F.; Walton, R. I.; O'Hare, D. *J.Mater.Chem.* **2000**, *10*, 1713-1720.

137. Trikeriotis, M.; Ghanotakis, D. F. *Int. J. Pharm.* **2007**, *332*, 176-184.

138. Allada, R. K.; Pless, J. D.; Nenoff, T. M.; Navrotsky, A. *Chem. Mater.* **2005**, *17*, 2455-2459.

139. Prasanna, S. V.; Kamath, P. V. *Ind. Eng. Chem. Res.* **2009**, *48*, 6315-6320.

140. Zeng, W. R.; Li, S. F.; Chow, W. K. *J. Fire Sci.* **2002**, *20*, 401-433.

141. Bertelli, G.; Camino, G.; Costa, L.; Locatelli, R. *Polym Degrad Stab* **1987**, *18*, 225-236.

142. Bertelli, G.; Costa, L.; Fenza, S.; Marchetti, E.; Camino, G.; Locatelli, R. *Polym Degrad Stab* **1988**, *20*, 295-314.

143. Hajšlová, J.; Pulkrabová, J.; Poustka, J.; Cajka, T.; Randák, T. *Chemosphere* **2007**, *69*, 1195-1203.

144. Kitamura, S.; Kato, T.; Iida, M.; Jinno, N.; Suzuki, T.; Ohta, S.; Fujimoto, N.; Hanada, H.; Kashiwagi, K.; Kashiwagi, A. *Life Sci.* **2005**, *76*, 1589-1601.

145. P.J Haines; M Reading *Thermal Methods of Analysis Principles, Applications and Problems*, first ed.; Blackie Academic & Professional: Glasgow, 1995.

146. Brown. M.E. *In Introduction to thermal analysis*, 2nd ed.; Kluwer Academic Publishers: Dordrecht, 2001.

147. Hull, A. W. *J. Am. Chem. Soc.* **1919**, *41*, 1168-1175.

148. Vitalij K.Pecharsky; Peter Y.Zavalij. *In Fundamentals of Powder Diffraction and Structural Characterization of Materials*; Kluwer Academic Publishers: Boston, 2001; Chapter 2, pp. 100-260.

149. Huggett, C. *Fire Mater.* **1980**, *4*, 61-65.

150. Gilman JW, Kashiwagi T, Nyden M, Brown JET, Jackson CL, Lomakin S, Gianellis EP, Manias E. In: Al-Malaika S, Golovoy A, Wilkie CA, editors. Flammability Studies of Polymer Layered Silicate Nanocomposites: Polyolefin, Epoxy and Vinyl Ester Resins, Chemistry and technology of polymer additives. London: Blackwell Science, 1999. p. 249

151. Gaussian 98, Revision A.11.4. Frisch MJ, Trucks GW, Schlegel HB, Scuseria GE, Robb MA, Cheeseman JR, Zakrzewski VG, Montgomery J A. Jr, Stratmann R E, Burant JC, Dapprich S, Millam JM, Daniels AD, Kudin KN, Strain MC, Farkas O, Tomasi J, Barone V, Cossi M, Cammi R, Mennucci B, Pomelli C, Adamo C, Clifford S, Ochterski J, Petersson GA, Ayala P Y, Cui Q, Morokuma K, Rega N, Salvador P, Dannenberg J J, Malick DK, Rabuck AD, Raghavachari K, Foresman JB, Cioslowski J, Ortiz JV, Baboul AG, Stefanov BB, Liu G, Liashenko A, Piskorz P, Komaromi I, Gomperts R, Martin RL, Fox DJ, Keith T, Al-Laham MA, Peng CY, Nanayakkara A, Challacombe M, Gill PMW,

Johnson B, Chen W, Wong MW, Andres J L, Gonzalez C, Head-Gordon M, Replogle ES, Pople JA, Gaussian, Inc., Pittsburgh PA, 2002

152. Biswick, T.; Jones, W.; Pacula, A.; Serwicka, E.; Podobinski, J. *J. Solid State Chem.* **2007**, *180*, 1171-1179.

153. Hwang, S. H.; Han, Y. S.; Choy, J. H. *Bull. Korean Chem. Soc.* **2001**, *22*, 1019-1022.

154. Powder Diffraction File. Andrews, L. C, Bernstein, L. R, Foris, C. M, McClune, W. F, Rendle, D. F, Rohrman, A. C, Rotella, F. J, Ryba, E, and Wallace, P. L. *Alphabetical Indexes for Experimental Pattern*. Set 1-59. 2009. Newtown Square, International Centre for Diffraction Data. Inorganic Phases.

155. Pereira, D. C.; de Faria, D. L. A.; Constantino, V. R. L. *J. Braz. Chem. Soc.* **2006**, *17*, 1651-1657.

156. Biswick, T.; Jones, W.; Pacula, A.; Serwicka, E. *J. Solid State Chem.* **2006**, *179*, 49-55.

157. Addison, C. C.; Gatehouse, B. M. *J. Chem. Soc.* **1960**, 613-616.

158. Rabu, P.; Drillon, M.; Hornick, C. *Analusis* **2000**, *28*, 103-108.

159. Kandare, E.; Hossenlopp, J. M. *Inorg. Chem.* **2006**, *45*, 3766-3773.

160. Prasanna, S. V.; Kamath, P. V. *J. Colloid Interface Sci.* **2009**, *331*, 439-445.

161. Neil Baerlett; B.W.McQuillan. *Intercalation Chemistry*; Academic Press: London, 1982; Chapter 2, pp. 19-98.

162. Williams, G. R.; O'Hare, D. *Chem. Mater.* **2005**, *17*, 2632-2640.

163. Solin, S. A. *J. Mol. Catal. A: Chem.* **1984**, *27*, 293-303.

164. Solin, S. A. *Annu. Rev. Mater. Sci.* **1997**, *27*, 89-115.

165. Iyi, N.; Kurashima, K.; Fujita, T. *Chem. Mater.* **2002**, *14*, 583-589.

166. Williams, G. R.; Fogg, A. M.; Sloan, J.; Taviot-Gueho, C.; O'Hare, D. *Dalton Trans.* **2007**, 3499-3506.

167. Miladinovic, Z.; Zakrzewska, J.; Kovacevic, B.; Bacic, G. *Mater. Chem. Phys.* **2007**, *104*, 384-389.

168. Williams, G. R.; Dunbar, T. G.; Beer, A. J.; Fogg, A. M.; O'Hare, D. *J.Mater.Chem.* **2006**, *16*, 1222-1230.

169. Mckelvy, M. J.; Sharma, R.; Glaunsinger, W. S. *Solid State Ionics* **1993**, *63-5*, 369-377.

170. McKelvy, M.; Sidorov, M.; Marie, A.; Sharma, R.; Glaunsinger, W. *Chem. Mater.* **1994**, *6*, 2233-2245.

171. Johnsen, R. E.; Krumeich, F.; Norby, P. *J. Appl. Crystallogr.* **2010**, *43*, 434-447.

172. Evans, J. S. O.; Price, S. J.; Wong, H. V.; O'Hare, D. *J. Am. Chem. Soc.* **1998**, *120*, 10837-10846.

173. Williams G.; Khan, A.; O'Hare, D. *Layered Double Hydroxides*; 119 ed.; Springer Berlin / Heidelberg: 2006; pp. 161-192.

174. Taviot-Gueho, C.; Feng, Y.; Faour, A.; Leroux, F. *Dalton Trans.* **2010**, *39*, 5994-6005.

175. Pilling, M.J; Seakins, P.W. *Reaction Kinetics*, Oxford University Press: Oxford, 1995.

176. Ho, Y. S.; Ng, J. C. Y.; Mckay, G. *Sep. Purif. Technol.* **2000**, *29*, 189-232.

177. Haque, R.; Lindstrom, F. T.; Freed, V. H.; Sexton, R. *Environ. Sci. Technol.* **1968**, *2*, 207-211.

178. ten Hulscher, T.; Cornelissen, G. *Chemosphere* **1996**, *32*, 609-626.

179. Ragavan, A.; Khan, A. I.; O'Hare, D. *J.Mater.Chem.* **2006**, *16*, 602-608.

180. Braithwaite, R. S. W.; Mereiter, K.; Paar, W. H.; Clark, A. M. *Mineral. Mag.* **2004**, *68*, 527-539.

181. Acrivos, J.V. *Intercalated Layered Materials*; D. Reidel Publishing Company: Dordrecht, 1979; Chapter 1, pp. 33-98.

182. Cardoso, L. P.; Celis, R.; Cornejo, J.; Valim, J. B. *J. Agric. Food Chem.* **2006**, *54*, 5968-5975.

183. Hussein, M. Z. b.; Siti Halimah; Yahaya, A. H.; Zainal, Z. *J. Nanosci. Nanotechnol.* **2007**, *7*, 2852-2862.

184. Li, F.; Jin, L.; Han, J.; Wei, M.; Li, C. *Ind. Eng. Chem. Res.* **2009**, *48*, 5590-5597.

185. Jubri, Z. b.; Hussein, M. Z. b.; Yahaya, A. H.; Zainal, Z.; Sarijo, S. H. *The Malaysian Journal of Analytical Sciences* **2008**, *12*, 491-499.

186. Zhang, H.; Zou, K.; Guo, S.; Duan, X. *J. Solid State Chem.* **2006**, *179*, 1792-1801.

187. Park, S. H.; Lee, C. E. *Bull. Korean Chem. Soc.* **2006**, *27*, 1587-1592.

188. Krause, W.; Bernhardt, H. J.; Braithwaite, R. S. W.; Kolitsch, U.; Pritchard, R. *Mineral. Mag.* **2006**, *70*, 329-340.

189. Ambrogi, V.; Fardella, G.; Grandolini, G.; Perioli, L. *Int. J. Pharm.* **2001**, *220*, 23-32.

190. Majoni, S.; Hossenlopp, J. M. *J. Phys. Chem. A* **2010**, *114*, 12858-12869.

191. Kodama, T.; Harada, Y.; Ueda, M.; Shimizu, K.; Shuto, K.; Komarneni, S. *Langmuir* **2001**, *17*, 4881-4886.

192. Li, Z. H. *Langmuir* **1999**, *15*, 6438-6445.

193. Auriemma, F.; De Rosa, C.; Triolo, R. *Macromolecules* **2006**, *39*, 9429-9434.

194. Ramanujan, R. V.; Zhang, Y. R. *Phys. Rev. B: Condens. Matter Mater. Phys.* **2006**, *74*.

195. Steel, W. H.; Foresman, J. B.; Burden, D. K.; Lau, Y. Y.; Walker, R. A. *J.Phys.Chem. B* **2009**, *113*, 759-766.

196. Kojima, Y.; Usuki, A.; Kawasumi, M.; Okada, A.; Fukushima, Y.; Kurauchi, T.; Kamigaito, O. *J. Mater. Res.* **1993**, *8*, 1185-1189.

197. Lan, T.; Kaviratna, P. D.; Pinnavaia, T. J. *Chem. Mater.* **1994**, *6*, 573-575.

198. Sinha Ray, S.; Okamoto, K.; Okamoto, M. *Macromolecules* **2003**, *36*, 2355-2367.

199. Xu, R. J.; Manias, E.; Snyder, A. J.; Runt, J. *Macromolecules* **2001**, *34*, 337-339.

200. Ye, L.; Ding, P.; Zhang, M.; Qu, B. J. *J.Appl.Polym.Sci.* **2008**, *107*, 3694-3701.

201. Zeng, W. R.; Li, S. F.; Chow, W. K. *Key Eng.Mat.* **2002**, *20*, 297-317.

202. Pitts, A. *Flame retardancy of polymeric materials*, Marcel Dekker: NY, 1973.

203. Armitage, P.; Ebdon, J. R.; Hunt, B. J.; Jones, M. S.; Thorpe, F. G. *Polym Degrad Stab* **1911**, *54*, 387-393.

204. Gerard, W. *The organic chemisry of boron*, Academic press: London, 1961.

205. Martin, C.; Hunt, B. J.; Ebdon, J. R.; Ronda, J. C.; Cadiz, V. *J. Polym. Sci., Part A: Polym. Chem.* **2005**, *43*, 6419-6430.

206. Martin, C.; Hunt, B. J.; Ebdon, J. R.; Ronda, J. C.; Cadiz, V. *React. Funct. Polym.* **2006**, *66*, 1047-1054.

207. Martin, C.; Ronda, J. C.; Cadiz, V. *J. Polym. Sci., Part A: Polym. Chem.* **2006**, *44*, 1701-1710.

208. Eltepe, H. E.; Balkőse, D.; Ülkü, S. *Ind. Eng. Chem. Res.* **2007**, *46*, 2367-2371.

209. Rosenthal, M. R. *J. Chem. Educ.* **1973**, *50*, 331.

210. Stahlin, W.; Oswald, H. R. *J. Solid State Chem.* **1971**, *3*, 252-255.

211. Kashiwagi, T.; Inaba, A.; Brown, J. E.; Hatada, K.; Kitayama, T.; Masuda, E. *Macromolecules* **2002**, *19*, 2160-2168.

212. Hirata, T.; Kashiwagi, T.; Brown, J. E. *Macromolecules* **1985**, *18*, 1410-1418.

213. Peterson, J. D.; Vyazovkin, S.; Wight, C. A. *J.Phys.Chem. B* **1999**, *103*, 8087-8092.

214. Lee, Y. M.; Viswanath, D. S. *Polym. Eng. Sci.* **2000**, *40*, 2332-2341.

215. Laachachi, A.; Cochez, M.; Ferriol, M.; Leroy, E.; Lopez Cuesta, J. M.; Oget, N. *Polym Degrad Stab* **2004**, *85*, 641-646.

216. Wang, H.; Xu, P.; Zhong, W.; Shen, L.; Du, Q. *Polym Degrad Stab* **2005**, *87*, 319-327.

217. Chang, T.; Wu, K. H. *Polym Degrad Stab* **1997**, *57*, 325-330.

218. Wang, H. T.; Meng, S.; Xu, P.; Zhong, W.; Du, Q. G. *Key Eng.Mat.* **2002**, *47*, 302-307.

219. Kashiwagi, T.; Du, F. M.; Winey, K. I.; Groth, K. A.; Shields, J. R.; Bellayer, S. P.; Kim, H.; Douglas, J. F. *Polymer* **2005**, *46*, 471-481.

220. Gao, Z.; Kaneko, T.; Hou, D.; Nakada, M. *Polym Degrad Stab* **2004**, *84*, 399-403.

221. Lin, J. P.; Chang, C. Y.; Wu, C. H.; Shih, S. M. *Polym Degrad Stab* **1996**, *53*, 295-300.

222. Ozawa, T. *Bull. Chem. Soc. Jpn.* **1965**, *38*, 1881-1886.

223. Flynn, J. H. *J J. Therm. Anal.* **1983**, *27*, 95-102.

224. Friedman JH. *J Polym Sci Polym Symp* **1964**, *6*, 183-195.

225. Kissinger, H. E. *Anal. Chem.* **1957**, *29*, 1702-1706.

226. Doyle, C. D. *J.Appl.Polym.Sci.* **1962**, *6*, 639-642.

227. Hu, Y. H.; Chen, C. Y.; Wang, C. C. *Polym Degrad Stab* **2004**, *84*, 545-553.

228. Holland, B.J; Hay, J.N. *Polym Degrad Stab* **2002**, *77*, 435-439.

229. K.Chen; R.C.Yang; S.W.Cheng. *Key Eng.Mat.* **2007**, *353-358*, 1366-1369.

230. Carrasco, F.; Pages, P. *J.Appl.Polym.Sci.* **1996**, *61*, 187-197.

231. Schartel, B.; Hull, T. R. *Fire Mater.* **2007**, *31*, 327-354.

232. Kashiwagi, T.; Du, F. M.; Douglas, J. F.; Winey, K. I.; Harris, R. H.; Shields, J. R. *Nature Materials* **2005**, *4*, 928-933.

233. Martin, C.; Ronda, J. C.; Cadiz, V. *Polym Degrad Stab* **2006**, *91*, 747-754.

234. Hogarth, C. A.; Ahmed, M. M. *J. Chem. Sci. Lett.* **1983**, *2*, 649-652.

235. Wu, Z.; Hu, Y.; Shu, W. *J Vinyl Addit Technol* **2009**, *15*, 260-265.

236. Manzi-Nshuti, C.; Hossenlopp, J. M.; Wilkie, C. A. *Polym Degrad Stab* **2009**, *94*, 782-788.
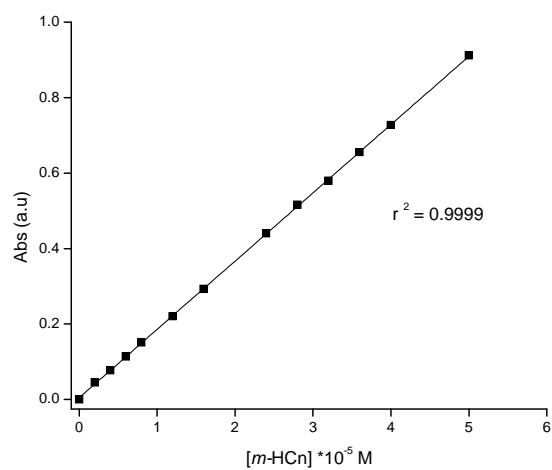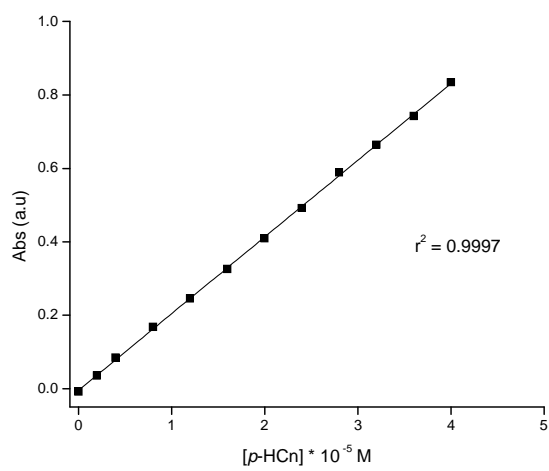
Appendix A
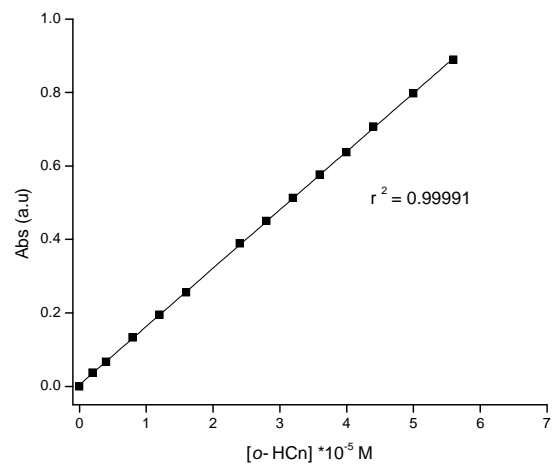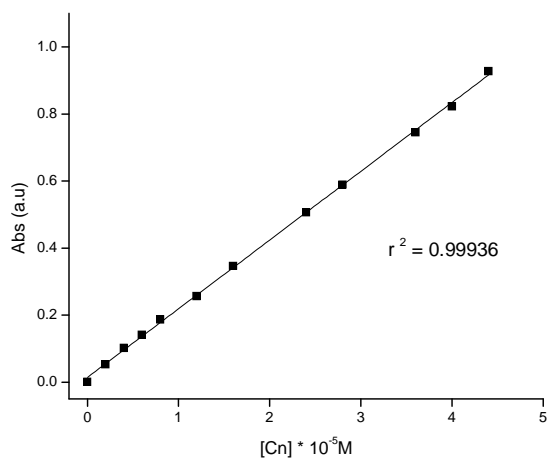
Representative UV-vis spectra collected during the release of isomers of

hydroxycinnamic acid
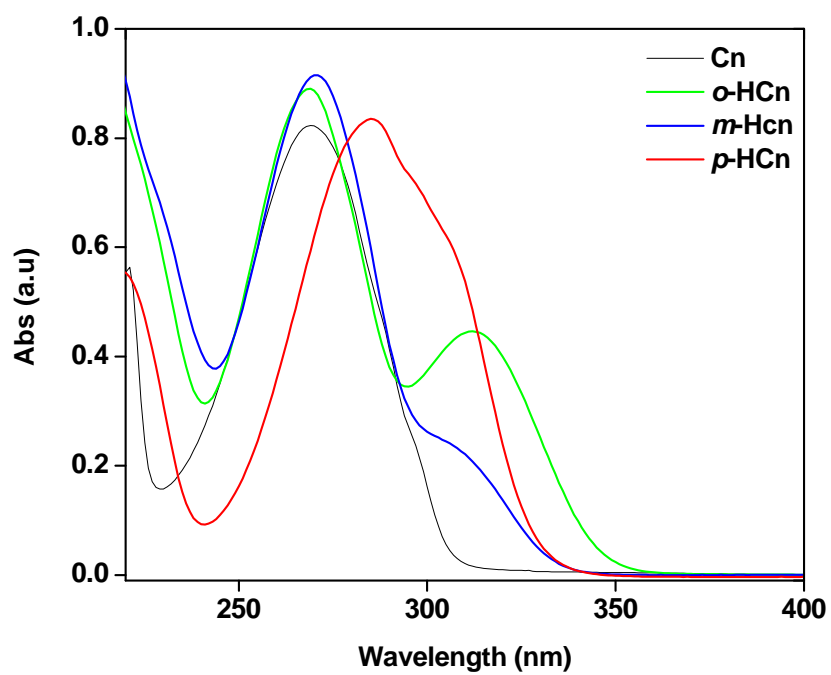
Appendix B

Calibration curves used for the analysis of filtrates obtained from anion exchange reactions.

Appendix C

Arrhenius plots for the determination of the activation energy for (I) the release of o-HCn from C-*o*-HCn for (A) solid state analysis, (B) solution analysis and (II) for the release of Cn from ZC-Cn (C) solid state analysis and (D) solution analysis
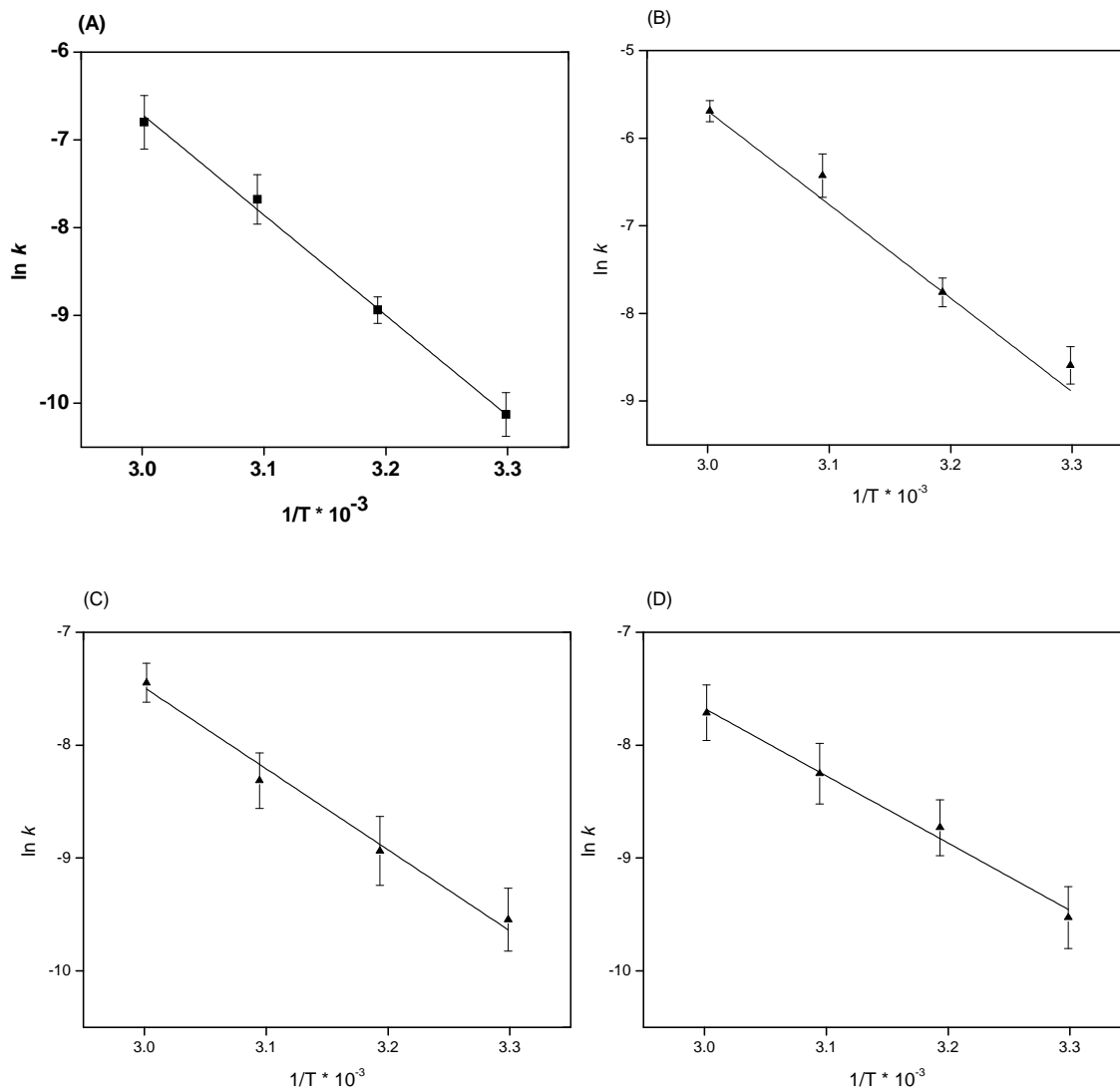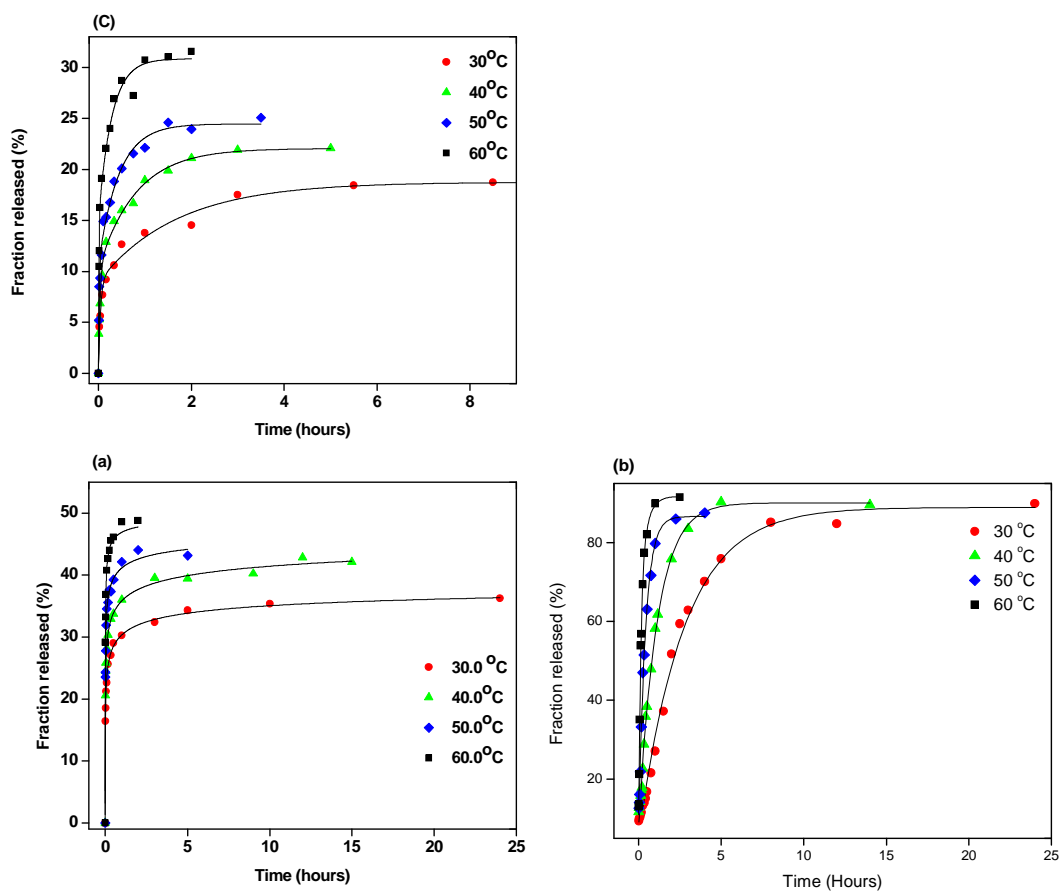
Appendix D

TG curves for the degradation of (a) ZC-*o*-HCn, (b) ZC-*p*-HCn and (c) ZC-*m*-HCn in nitrogen atmosphere at a ramp rate of 20°C/min
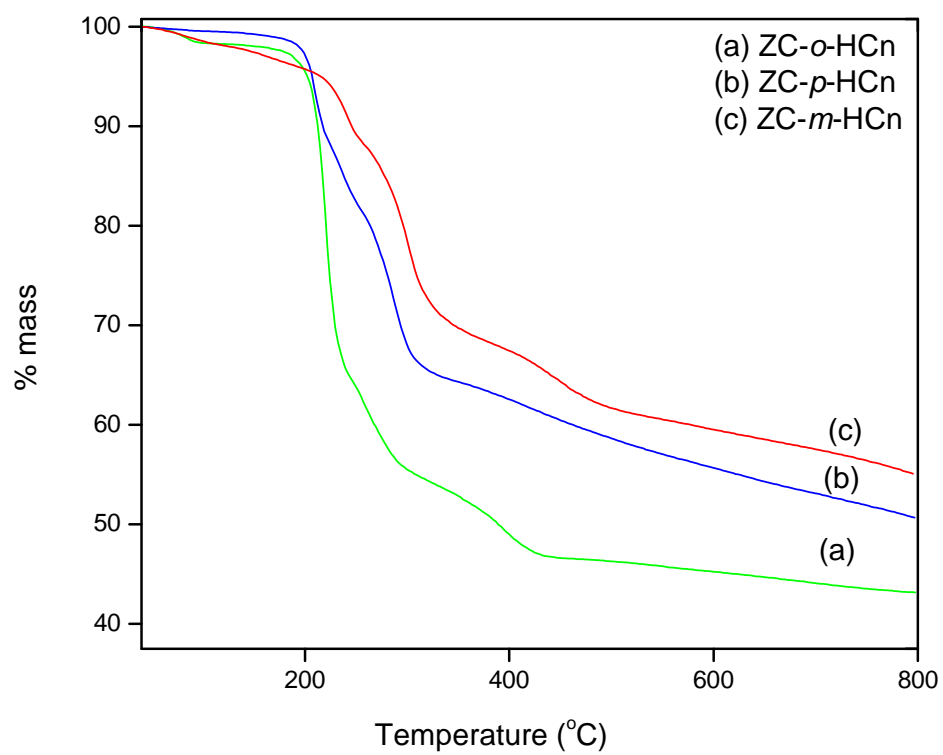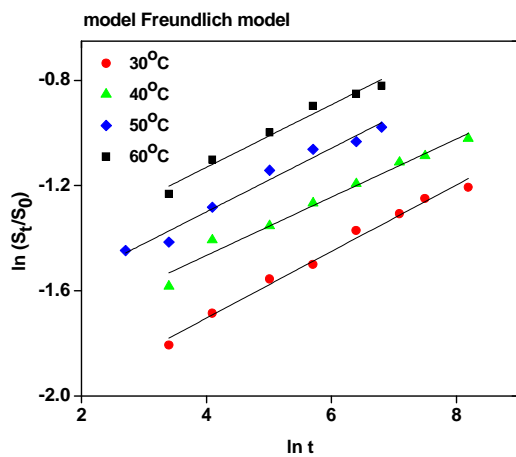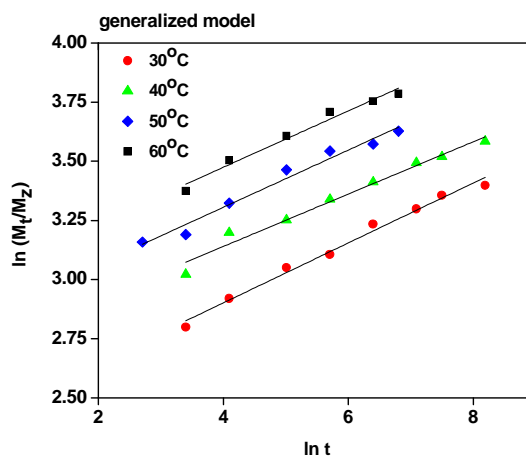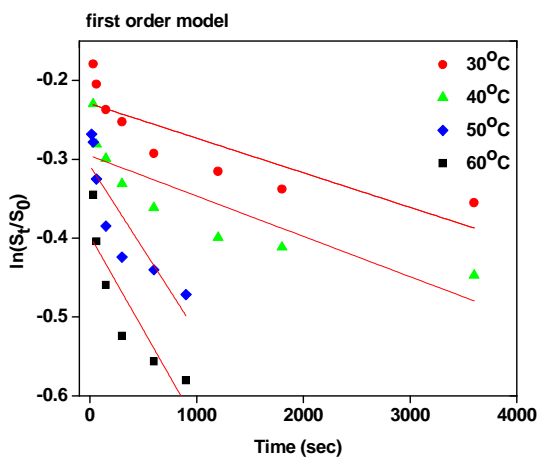
Appendix E

Extent of release for **(a)** *m*-HCn **(b)** *o*-HCn **(c)** *p*-HCn at different temperatures in 1 M sodium chloride solution.

Appendix F

i.   Fitting ZC-o-HCn to different release models
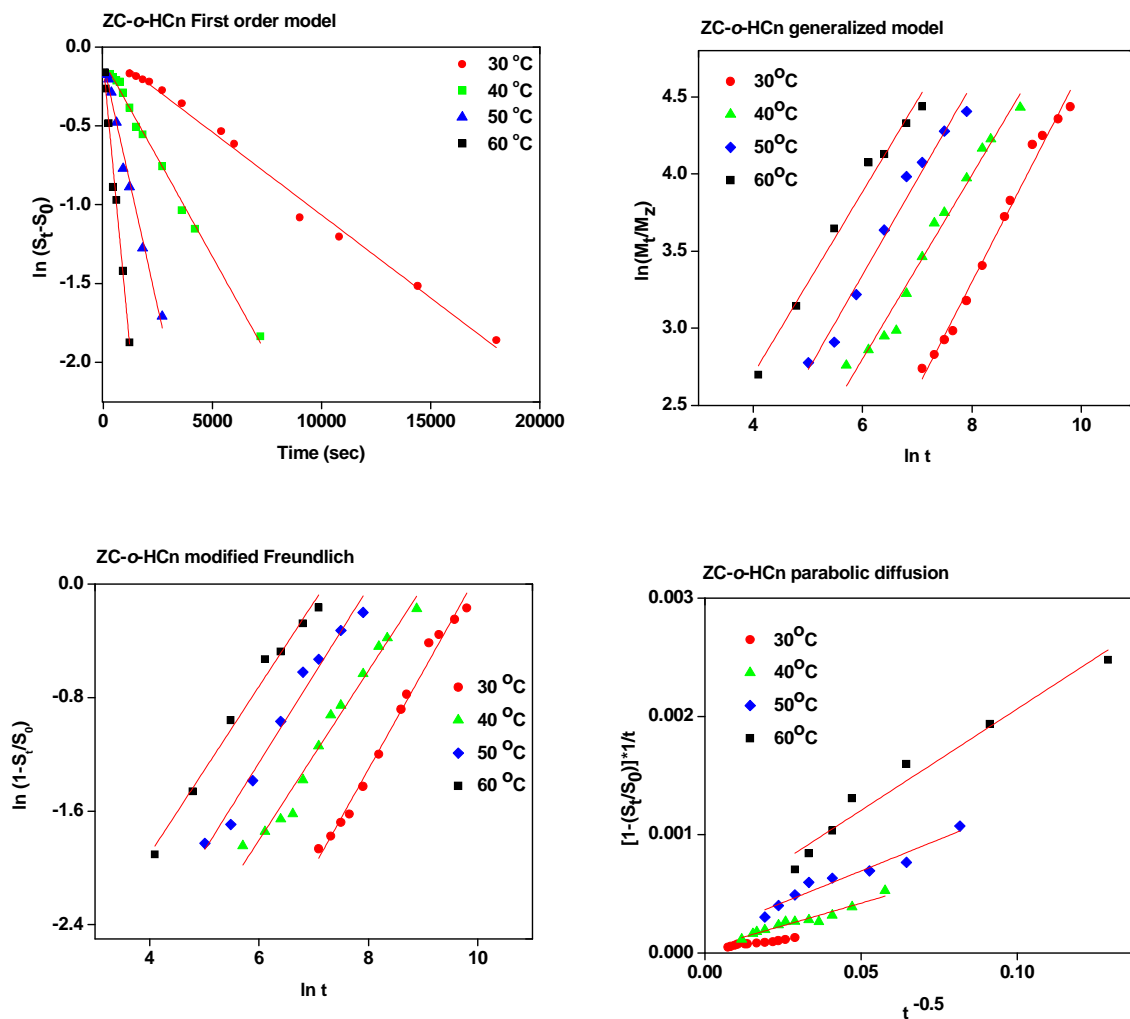
ii)   Fitting ZC-*m*-HCn to different release models
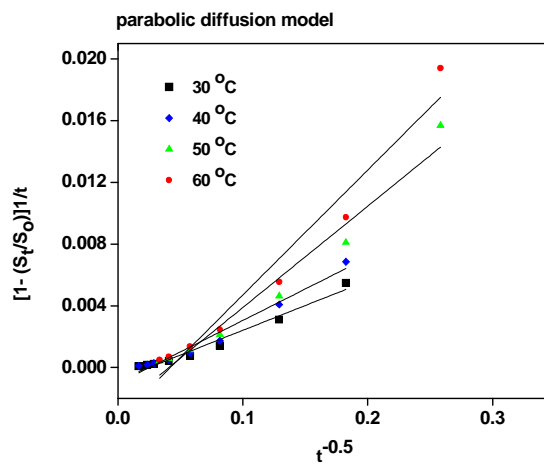
iii)   Fitting ZC-*p*-HCn to different release models